SURFACE ENHANCED RAMAN SPECTROSCOPY OF COLLAGEN I FIBRILS

by

Corinne Gullekson

Submitted in partial fulfillment of the
requirements for the degree of
Master of Science

at

Dalhousie University
Halifax, Nova Scotia
August 2011

DALHOUSIE UNIVERSITY

DEPARTMENT OF PHYSICS AND ATMOSPHERIC SCIENCE

The undersigned hereby certify that they have read and recommend to the Faculty of Graduate Studies for acceptance a thesis entitled "SURFACE ENHANCED RAMAN SPECTROSCOPY OF COLLAGEN I FIBRILS" by Corinne Gullekson in partial fulfillment of the requirements for the degree of Master of Science.

Dated: August 5, 2011

Supervisor: _____

Readers: _____

_____

DALHOUSIE UNIVERSITY

DATE: August 5, 2011

AUTHOR: Corinne Gullekson

TITLE: Surface enhanced Raman spectroscopy of collagen I fibrils

DEPARTMENT OR SCHOOL: Department of Physics and Atmospheric Science

DEGREE: MSc CONVOCATION: October YEAR: 2011

_____

Signature of Author

Table of Contents

List of Tables

List of Figures

Abstract

Collagen fibrils are the main constituent of the extracellular matrix surrounding eukaryotic cells. Even though the assembly and structure of collagen fibrils is well characterized, very little is known about the physico-chemical properties of their surface which is one of the key determinants of their biological functions. One way to obtain surface sensitive structural and chemical data is to take advantage of the near field nature of surface and tip-enhanced Raman spectroscopy. Using Ag and Au nanoparticles bound to collagen type I fibrils, as well as tips coated with a Ag nanoparticles and a thin layer of Ag, we obtained Raman spectra characteristic of the first layer of collagen molecules at the surface of the fibrils. The most frequent Raman peaks were attributed to aromatic residues such as phenylalanine and tyrosine. We also observed in several instances Amide I bands with a full width at half maximum of 10-30 cm^{-1}. The assignment of these Amide I bands positions suggests the presence of collagen-helices as well as α-helices and β-sheets at the fibrils surface. As a step towards *in vivo* characterization of collagen fibrils, fascicles removed from tendons were also examined with surface-enhanced Raman spectroscopy.

List of Abbreviations and Symbols Used

CCD	charge coupled device
AFM	atomic force microscopy
SERS	surface-enhanced Raman spectroscopy
TERS	tip-enhanced Raman spectroscopy
DNA	deoxyribonucleic acid
SER	surface-enhanced Raman
TER	tip-enhanced Raman
ECM	extracellular matrix
Gly	glycine
Pro	proline
Ala	alanine
Arg	arginine
Glu	glutamic acid
Ser	serine
Lys	lysine
Asp	aspartic acid
Gln	glutamine
Leu	leucine
Thr	threonine
Val	valine
Phe	phenylalanine
Asn	asparagine
Met	methionine
Ile	isoleucine
Tyr	tyrosine
His	histidine
PDB	protein data bank
FACIT	fibril-associated collagen with interrupted triple-helices

UV	ultraviolet
$\hbar$	reduced Plank constant
ω_0	angular frequency of an exciting photon
ω_s	angular frequency of a scattered photon
ω_m	angular frequency of a molecular vibration
$\mathbf{E}$	electric field
t	time
$\mathbf{P}$	dipole
$\hat{\alpha}$	polarizability tensor
$\mathbf{q}$	nuclear displacement
r	radius of a dielectric sphere
d	distance away from the metal surface
θ	angle with respect to the incident electric field
ϵ	dielectric constant
A	electric field enhancement factor
M	Raman signal enhancement factor
e	Euler's number
NA	numerical aperture
DIC	differential interference contrast
PBS	phosphate buffered saline
I	intensity
Vis	visible
a.u.	arbitrary units
TEM	transmission electron microscopy
FWHM	full width at half maximum
$\hat{R}$	Raman tensor
FIB	focused ion beam
PDADMAC	polydiallyl dimethyl ammonium chloride
3-MPTS	(3-mercaptopropyl)trimethoxysilane

Acknowledgements

I would like to thank all the people who have helped and inspired me during my thesis research. I especially want to thank my advisor, Laurent Kreplak, for his encouragement, guidance and support during my research and study at Dalhousie University. His perpetual energy and enthusiasm in research has always motivated me to achieve better. In addition, he was always accessible and willing to help his students with their research. As a result, my research advanced speedily, smoothly and was very rewarding for me.

I would like to thank my parents, Garth and Joanne Gullekson, for all the love, support and caring they provided. Lastly, I would like to thank Benedict Drevniok for his daily emotional support and grad student advice and for sticking with me after I moved 1500 km away to pursue this degree.

Chapter 1

Introduction

For more than three decades, protein structures have been investigated with Raman spectroscopy [1]. During this time band assignments of secondary structures and amino acid residues have been established. Raman spectroscopy is a popular tool for proteins due to it being a non-destructive, fast analysis technique that requires small sample volumes [2]. Water is also a weak Raman scatterer, compared with IR, which makes it an ideal choice for water-rich biological samples. Technological advances such as charge coupled device (CCD) detectors have dramatically increased the achievable signal-to-noise ratio in Raman spectra resulting in new insights into protein folding, assembly and aggregation [1]. The new generation of commercial Raman instruments has steered numerous applications of protein analysis in biotechnology, pharmaceutical production and the food industry [1].

The main disadvantage of Raman scattering is that it is an inelastic process that suffers from a small scattering cross-section [3]. However, by coupling the molecule or macromolecular assembly of interest with a metallic nanostructure such as a gold or silver nanoparticle or a silver-coated atomic force microscopy (AFM) tip, it is possible to achieve signal enhancement of up to 10^{14} [4] and 10^{9} [5], respectively. Both approaches, named surface-enhanced Raman scattering (SERS) and tip-enhanced Raman scattering (TERS), have been recently applied to the characterization of viruses, cells, DNA, single amino acids, and amyloid fibrils [6, 7, 8, 9, 10]. With the enhancement effect being due to a coupling between the metal nanostructure and the sample, the penetration depth is limited to a few nanometers [11, 12], making SERS and TERS surface-sensitive techniques.

The application of SERS and TERS has the opportunity to once again rejuvenate Raman spectroscopy of protein structure. Their spatial and chemical specificity [13] can be used to obtain surface-sensitive structural and chemical information of large protein assemblies such as collagen I fibrils.

1.1 Goal

The goal of this thesis is to study the surface structure of collagen I fibrils with SERS and TERS. Although SERS and TERS are not new techniques, their application to biological samples is still relatively recent. Techniques developed in this thesis to study collagen I fibrils could be applied to other protein assemblies.

We want to develop procedures to study both the surface molecules of the protein and their secondary structure. We want to build up these techniques to the point were it is possible to map functional sites on the protein. We also want to examine the secondary structure of the fibril without the use of any spectral decomposition of the Amide I band. This can be accomplished by examining the positions of SERS and TERS Amide I bands. Ideally, the Amide I peaks can be used for the future application of spatially mapping secondary structure as well and measuring changes in secondary structure during types of stress and deformation.

1.2 Outline

In this thesis, along with a paper on the same topic [14], we demonstrate some of the first characterizations of the surface of *in vitro*-assembled rat tail collagen I fibrils by both SERS and TERS. In the following, we provide a brief outline of the structure of the thesis.

The purpose of Chapter 2 is to provide sufficient background to understand the rest of the thesis. It contains an overview of collagen I structure and the basic theory of an atomic force microscope. Raman scattering is then introduced with a semi-classical derivation of the phenomenon. It is followed with an introduction to SERS and TERS and their electromagnetic enhancement mechanisms. Chapter 3 describes the basic experimental details of this thesis. It describes the set-up of our Raman spectrometer and atomic force microscope. The SERS and TERS set-ups are also explained along with the protocol used to assemble collagen I fibrils and data analysis techniques used to interpret Raman spectra.

In Chapter 4, the characterization of collagen fibrils by SERS is presented. The nanoparticles used are characterized by their size, plasmon resonance, shape, distribution on the fibrils, background spectra and their spectral fluctuations. Both gold

and silver SER spectra of the collagen I fibrils are presented and compared to the far field Raman spectra of collagen and phenylalanine. The enhanced Amide I bands are presented and compared to the spectral deconvolution of the far field Raman Amide I band.

In Chapter 5, the TERS characterization of collagen fibrils is presented. A variety of tip manufacturing methods are discussed and characterized. The collagen I fibril TER spectra are presented and compared to the far field Raman spectrum and the SER spectra of collagen. The mapping of collagen I fibrils with TERS is discussed. The TERS Amide I bands are compared with the far field and SERS amide I bands.

The last set of experiments was carried out on rat tail tendon fascicles and are discussed in Chapter 6. The spectra of fascicles soaked in nanoparticles are examined. They are compared with the far field spectra of the collagen and the SER spectra of the collagen I fibrils.

Chapter 2

Background

2.1 Collagen Structure

2.1.1 Introduction

Collagen is the most abundant protein in the human body. It is a main component of the extracellular matrix (ECM), particularly in connective tissues including skin, tendons, bone and cartilage [15]. Collagen fibrils provide the major biomechanical scaffold for cell attachment and anchorage of macromolecules, defining the shape and elasticity of tissues [16]. Currently, there are 29 members of the human collagen protein family; among these, collagen I is the most abundant [17]. The molecular structure of collagen and its hierarchical structure have been studied using a variety of techniques, including electron microscopy and x-ray diffraction beginning in the 1950s [18, 19, 20]. These studies reveal a complex structure.

2.1.2 Collagen Molecule

Collagen is distinct from other proteins in that the molecule comprises three polypeptide chains which form a triple-helical structure. This is a result of collagen's repetitive sequence. The polypeptides have a repeating structure Gly-Xaa-Yaa with a glycine every 3 residues and the Xaa and Yaa positions often filled by proline and hydroxyproline. The Xaa and Yaa positions are also filled by other amino acids such as alanine, arginine, glutamic acid and serine (Table 2.1). The collagen molecules consist of three polypeptide chains in an uninterrupted triple helix 300 nm in length and 1.5 nm in diameter flanked by short telopeptides [16] (Figure 2.1A). The telopeptides do not have a repeating Gly-Xaa-Yaa structure and do not adopt a triple-helical conformation. The structure of the telopeptides has been predicted by sequence analysis and computer modelling. It has been suggested that the telopeptides adopt a β-sheet structure with one hairpin turn [23, 24].

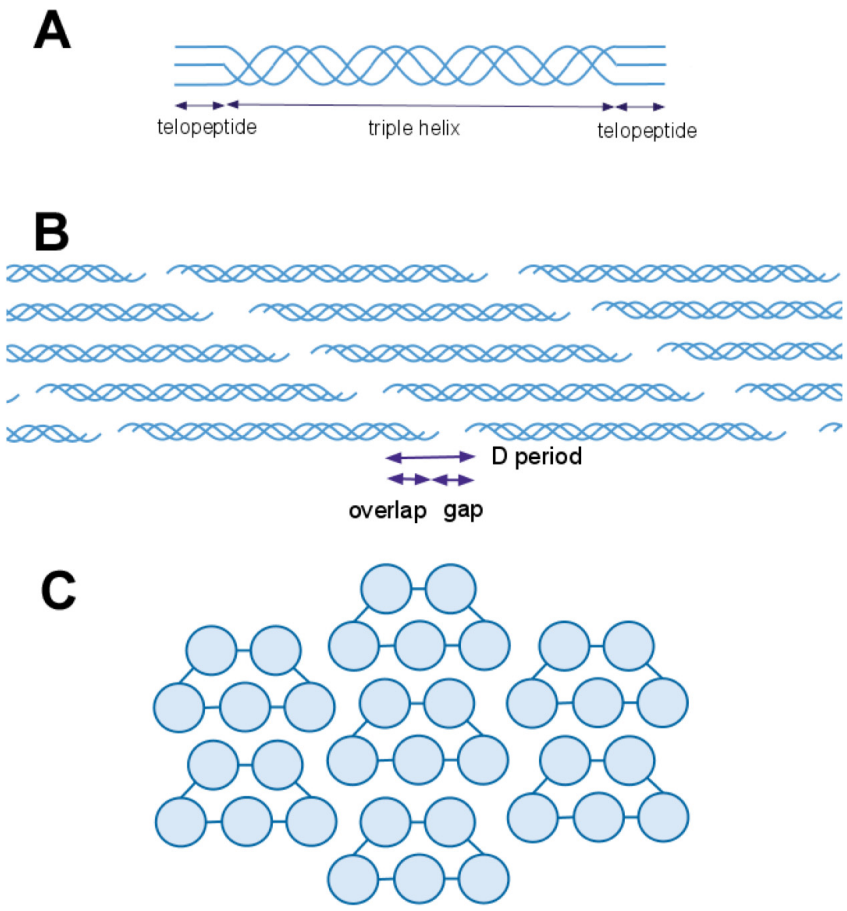

Figure 2.1: A diagram of collagen I organization. A) Diagram of the collagen triple helix after cleavage of the terminal pro-peptides modified from Shoulders et. al. [21]. There are non-triple helical telopeptides at the ends of the molecule. B) Diagram of the 67 nm D spacing observed in collagen microfibrils modified from Shoulders et. al. [21]. C) Diagram of the packing of microfibrils within collagen fibrils suggested by Trus et al.[22]. Each circle represents one triple helix. Microfibrils are composed of 5 cross linked triple helices.

Gly	Pro	Ala	Arg	Glu	Ser	Lys	Asp	Gln
32.8%	22.3%	10.9%	5.0%	4.6%	4.2%	3.6%	3.2%	2.9%
Leu	Thr	Val	Phe	Asn	Met	Ile	Tyr	His
1.9%	1.9%	1.9%	1.3%	1.3%	0.8%	0.7%	0.5%	0.2%

Table 2.1: The amino acid composition of the rat collagen I chain after the cleavage of the propeptides. The propeptides are the parts of the molecule cleaved during maturation.

The triple helix of collagen is called the collagen-helix (Figure 2.2A). The structure of the collagen-helix has been characterized for bulk tendons [25, 26] and for collagen-like peptides [19] by X-ray diffraction. This helix has 3.3 residues per turn, a rise per residue of 0.29 nm and a right handed twist [27]. It is unstable in its single stranded form and is only observed as a triple helix [21]. This is due to the hydrogen bonding pattern of the triple helix. Hydrogen bonds are formed between adjacent peptide chains as opposed to inter-chain hydrogen bonds. In contrast, the most prevalent secondary structure in proteins are the α-helix followed by the β-sheet (Figure 2.2B,C). The α-helix is less tightly wound than the collagen-helix with 3.6 residues per turn, a rise per residue of 0.15 nm and occurs in a single stranded form [28].

After the peptide chains are synthesized in the cell, they undergo post-translational modifications that affect the stability and function of collagen. These modifications include the hydroxylation of certain proline and lysine residues and the glycosylation of hydroxylysine residues (Figure 2.3) [29]. After these modifications, the chains assemble into triple-helical trimers called procollagen initiated by the formation of di-sulfide bonds in the C-terminus propeptide [30].

2.1.3 Collagen Fibril

After post-translational modifications, the procollagen molecules are excreted into the extracellular space. The propeptides are cleaved by specific enzymes [16] and the collagen molecules form fibrils with a diameter of 100-500 nm and a length up to the millimeter range [31]. The fibrils are made up of repeating units of collagen bundles called microfibrils. The microfibrils contain five tropocollagen molecules in a staggered spiral formation [32]. The microfibrils have a left handed superhelical

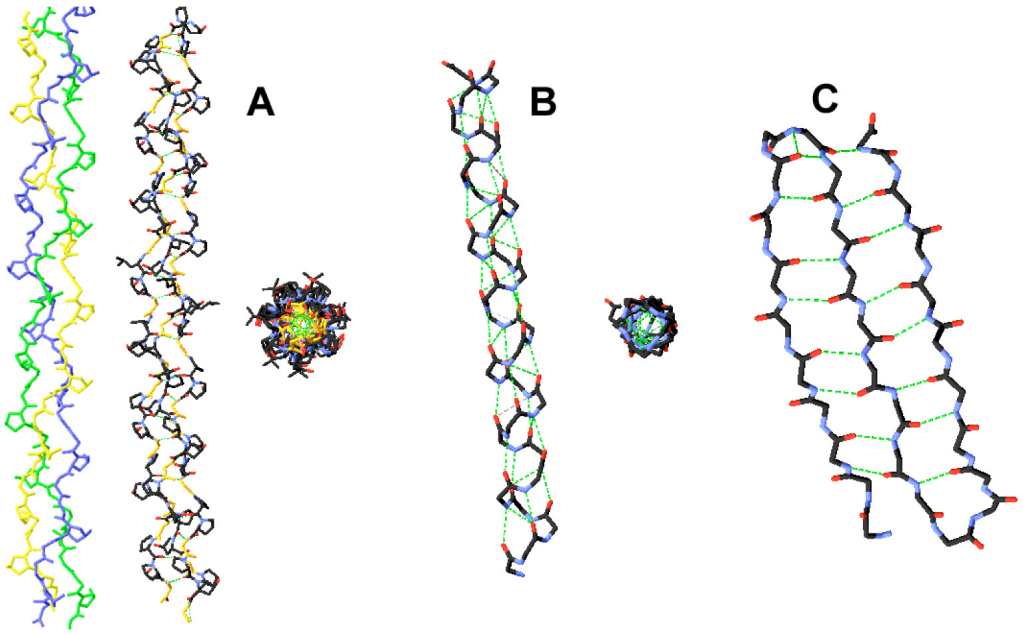

Figure 2.2: A comparison of protein secondary structures. Carbon, nitrogen and oxygen atoms are represented by black, blue and red lines respectively (colour available in electronic version). Hydrogen bonds are represented by green dotted lines. A) The helix of a collagen like polypeptide (PDB entry 2DRX). The first triple helix has each strand in a different colour. In the second triple helix, the glycine amino acids are shown in orange. Note that the hydrogen bonds are between adjacent chains and the glycine amino acids are placed closer to the helical axis than the other amino acids. B) An example of an α-helix (from PDB entry 2CCE). Note the inter-chain hydrogen bonds. C) An example of an β-sheet (from PDB entry 1ICM). Note the inter-chain hydrogen bonds and the sharp turns in the chain (called β-turns).

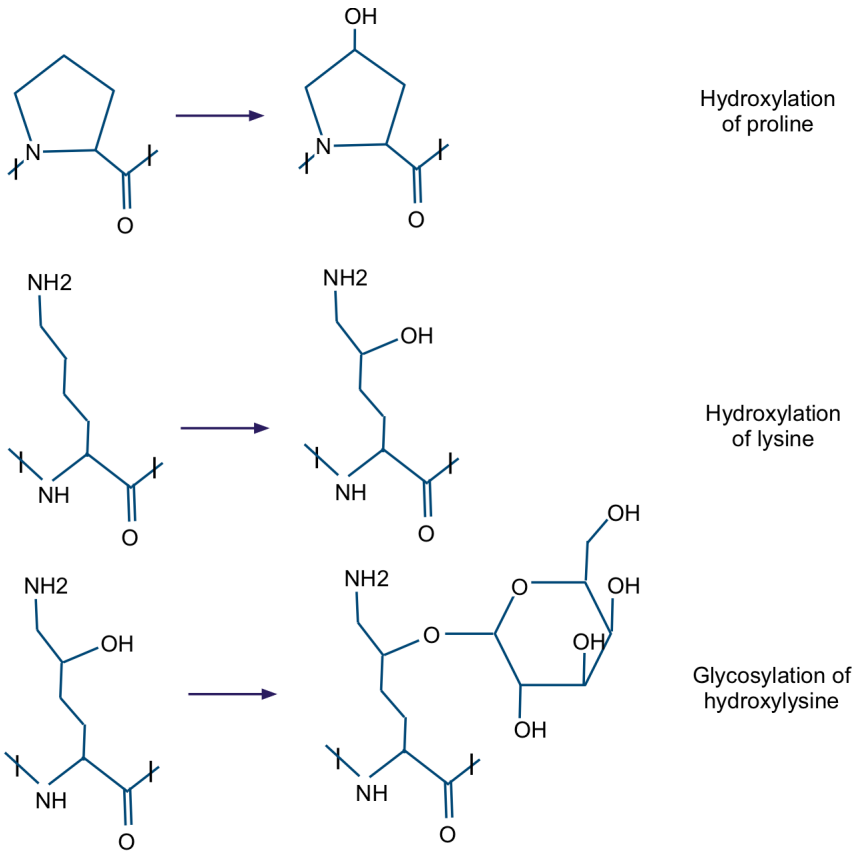

Figure 2.3: Diagram of the glycosylation and hydroxylation reactions.

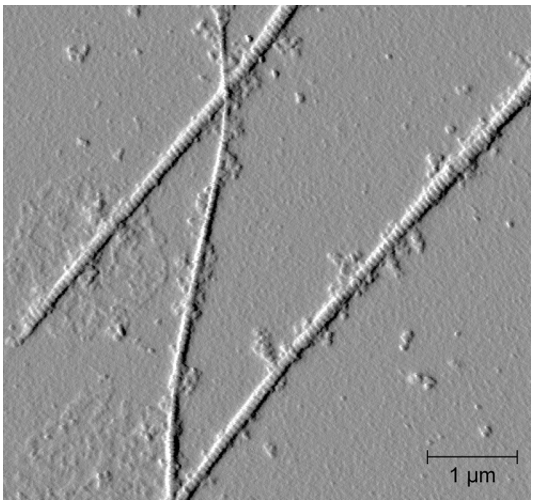

Figure 2.4: An atomic force microscopy deflection image of collagen fibrils on glass. The image was taken in contact mode with a 0.03 N/m MSNL cantilever. The fibrils were assembled in vitro in phosphate buffered saline from rat tail collagen I.

arrangement [32]. Groups of micro fibrils are packed laterally in bundles in a pseudo-hexagonal lattice (Figure 2.1C) [22]. The assembly of collagen molecules into fibrils is an entropy-driven process. It is driven by the loss of water molecules from the surface of protein chains and result in assemblies with a circular cross-section, which minimizes the surface area to volume ratio of the final assembly [16]. There is a gap separating each collagen molecule of approximately 36 nm. The gap and overlap regions can be observed by atomic force microscopy . The spacing between the start of one overlap or gap region and the next is called the D spacing which is approximately 67 nm for type I collagen fibrils (Figure 2.1B) [33].

2.1.4 Collagen Fibers and Networks

At the next level of organization, multiple fibrils form collagen fibers and networks. These networks of fibrils incorporated with other molecules form the ECM. Fibrils are bundled via a number of molecular components including proteoglycans [34]. Proteoglycans are a main component of the ECM and play a major role in fibril's binding to other proteins and cells. These molecules dictate the interaction between fibrils and subsequently fibril bundling is largely dependant on the types of proteoglycans present. Fibrils are also connected by fibril-associated collagens with interrupted

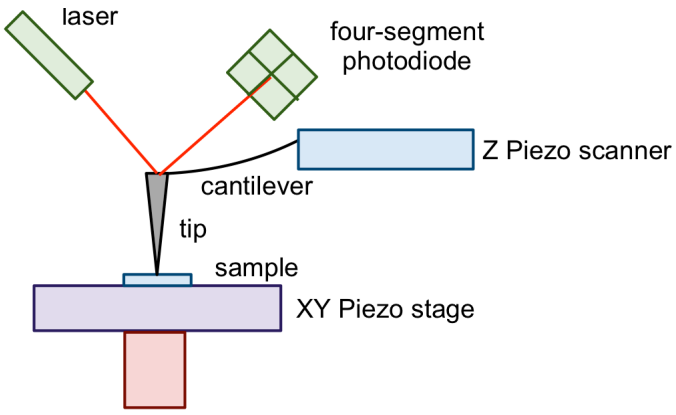

Figure 2.5: Diagram of an atomic force microscope.

triple-helix (FACITs). FACITs cannot form fibrils themselves but they can bind, via their triple helix tract, to fibrils of other types.

This work will concentrate on the fibril level of organization, investigated with atomic force microscopy and Raman spectroscopy.

2.2 Atomic Force Microscopy

The atomic force microscope (AFM) is a high resolution microscope that overcomes the optical diffraction limit. It is a local probe technique, designed to measure interaction forces of a sharp tip with the surface of a sample, making it one of the most popular tools for imaging, measuring and manipulating matter at the nanoscale. The tip is etched out of one end of a thin cantilever, which is fixed at the opposite end to a solid support (Figure 2.5). As the tip is brought to within interaction-distance of the sample surface, the lever will deflect by an amount proportional to the force experienced by the tip [35]. This deflection is detected by a laser that is focused onto the back of the cantilever. The reflected beam is detected by a four-segment photodiode. The position of the reflected beam on the photodiode is measured to determine the defection of the cantilever [36]. This is done by comparing the relative intensity of the reflected laser light in each quadrant. The cantilever's solid support can be adjusted to scan over a sample. In a sample scanning instrument such as the one used in this work, the cantilever moves in the z direction to keep the deflection constant while the

sample is scanned in the x and y directions. These precise movements are performed by 3 piezoelectric elements. By using an AFM, not only can one image the surface at atomic resolution, but also measure forces at the nanonewton scale [36]. The AFM can be used to image surfaces in both air and aqueous environments.

AFMs have several different modes of operation. The modes utilized in this thesis are contact mode and tapping mode. In contact mode, the tip remains in contact with the sample during the scanning process. With the z piezoelectric positioning element, the height can be adjusted so the tip feels a constant repulsive force. This is achieved by choosing the appropriate deflection set-point. If the measured deflection is different from the desired value, voltage will be applied to the piezo by a feedback controller to raise or lower the tip with respect to the sample so that the desired value of deflection can be restored [37]. Measuring the tip-sample distance at each point allows the construction of a topographic image of the sample surface.

Tapping mode is often utilized to protect the tip from wear and reduce the shear force on the sample [37]. The cantilever is driven by piezoelectrics to oscillate near its resonant frequency and positioned over the surface. When interacting with the sample, attractive forces cause a change in the amplitude of the oscillation [37]. The feedback loop maintains a constant oscillation amplitude by adjusting the tip to sample distance to compensate for the change in resonant frequency.

In this thesis, the tip was usually coated with metal and used as a probe in conjunction with Raman spectroscopy. The AFM was mainly utilized for its ability to position a tip directly over a sample and its nanoscale mapping capabilities.

2.3 Raman Spectroscopy

Light can interact with the atoms and molecular bonds of biological samples in a variety of ways. Most photons are elastically scattered in a process called Rayleigh scattering. This is the type of scattering observed in classical optical microscopy. However, a small fraction of the photons, approximately 1 in 10^6, will interact with the sample through an inelastic process called Raman scattering [38]. Raman scattering is used to probe deformation modes of the electron clouds of a sample. It is often applied with excitation sources in the UV to infrared region. There are two types of Raman scattering, Stokes scattering and anti-Stokes scattering (Figure 2.6). In Stokes

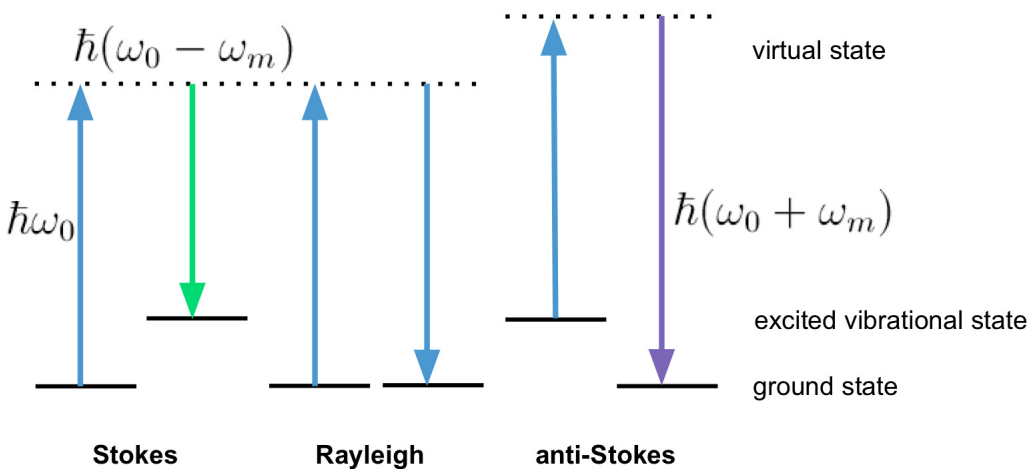

Figure 2.6: Energy diagram of the Raman process. Note that the virtual state is not a real physical state.

scattering, a photon of energy, $\hbar\omega_0$, excites a molecule to a virtual energy state. The virtual energy state can be considered a short lived distortion of the electron cloud as a result of the oscillating electric field of the incident light. The molecule then relaxes to an excited vibrational state emitting a photon of energy $\hbar\omega_s$. The difference between the two photon energies, $(\hbar\omega_0 - \hbar\omega_s)$, is the energy of the characteristic molecular vibration, $\hbar\omega_m$. This shift provides useful information on chemical structure. In anti-Stokes scattering, the molecule starts in an excited vibrational state and relaxes to a vibrational state of lower energy. The population of excited vibrational modes is described by the Boltzmann distribution, which implies that at room temperature, Stokes scattering is more probable than anti-Stokes scattering. For this reason, most Raman spectroscopy approaches only use the Stokes Raman signal.

2.3.1 Semi-Classical Derivation

Different vibrations can have peaks of varying Raman intensities. This can be explained with the semi-classical theory of Raman Scattering. A polarization is induced in the molecule by the oscillating electric field of the incoming light. The induced dipole radiates scattered light. The oscillating electric field of the incident light, $\mathbf{E}$, can be represented by

$$\mathbf{E} = \mathbf{E}_0 \cos(\omega_0 t) e^{ik_0 x} \tag{2.1}$$

where $\mathbf{E}_0$ is the maximum electric field and ω_0 is the frequency of the laser. This electric field induces a dipole, $\mathbf{P}$, described by

$$\mathbf{P} = \hat{\alpha}\mathbf{E} \tag{2.2}$$

where $\hat{\alpha}$ is the polarizability tensor of the molecule. If the molecule is vibrating at a frequency ω_m, the nuclear displacement, $\mathbf{q}$, is written as

$$\mathbf{q} = \mathbf{q}_0 \cos(\omega_m t) \tag{2.3}$$

where $\mathbf{q}_0$ is the vibrational amplitude. For a small amplitude vibration, $\hat{\alpha}$ can be represented at the first order of $\mathbf{q}$. Hence:

$$\hat{\alpha} = \hat{\alpha}_0 + \left(\frac{\partial\hat{\alpha}}{\partial\mathbf{q}}\right)_0 \mathbf{q}_0 + ... \tag{2.4}$$

where $\hat{\alpha}_0$ is the polarizability at equilibrium position and $(\partial\hat{\alpha}/\partial\mathbf{q})_0$ is the rate of change evaluated at the equilibrium position. Combining these equations and noting that $\cos a \cos b = [\cos(a+b) + \cos(a-b)]/2$, we obtain

$$\mathbf{P} = \hat{\alpha}_0\mathbf{E}_0 \cos(\omega_0 t)e^{ik_0 x} + \frac{1}{2}\left(\frac{\partial\hat{\alpha}}{\partial\mathbf{q}}\right)_0 \mathbf{q}_0\mathbf{E}_0[\cos((\omega_0+\omega_m)t) + \cos((\omega_0-\omega_m)t)]e^{ik_0 x} \tag{2.5}$$

This equation predicts light scattering at three frequencies. The first term is the Rayleigh scattering with a scattering frequency of ω_0. The equation also predicts anti-Stoke and Stokes scattering at frequencies $\omega_0+\omega_m$ and $\omega_0-\omega_m$ respectively. The anti-Stokes and Stokes terms are proportional to $(\partial\hat{\alpha}/\partial\mathbf{q})$. When this term is zero, there is no Raman scattering. For this reason, a vibrational mode is only Raman active if the interaction of the molecule with incident light results in a change of polarizability. This depends on the vibrational mode's geometry and the orientation of the incident electric field. The strength of $(\partial\hat{\alpha}/\partial\mathbf{q})$ may also vary strongly for different molecules and modes resulting in different Raman intensities. At high electric field strengths, the term from a third order approximation of $\hat{\alpha}_0$ may contribute to the scattering. This results in the observation of previously Raman inactive modes.

2.3.2 Surface Enhanced Raman Spectroscopy (SERS)

Due to Raman scattering's small cross section its applications are limited, specifically when looking at a small number of molecules or weak Raman modes. In order to

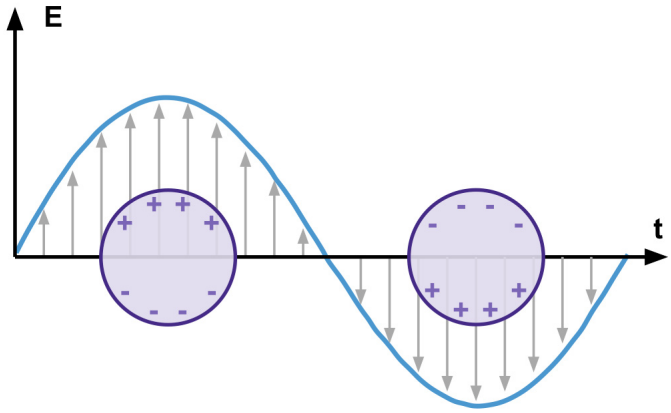

Figure 2.7: Schematic diagram illustrating a localized surface plasmon.

increase the Raman signal, one must either increase the electric field or the polarizability. The strong electric field enhancement mechanism called SERS, was initially discovered with the absorption of molecules to rough metal surfaces [39]. It is a surface-sensitive technique that enhances the Raman scattering signal of absorbed molecules. In this thesis we will be using metallic nanoparticles instead of roughened metal surfaces. Both approaches use the same mechanism of electromagnetic enhancement. The electromagnetic enhancement can be viewed as a redistribution of the electromagnetic field, resulting in localized regions of high field intensities.

When a metallic nanoparticle interacts with the electric field of the incident light, there is collective motion of the free electrons in the opposite direction of the electric field. The skin depth of the electric field inside the nanoparticle can be estimated with the plasmon frequency of the nanoparticle ($\delta \approx c/\omega_p$). This is approximately 100 nm for gold nanoparticles and 85 nm for silver nanoparticles. For metallic nanoparticles with high conductivity and that are much smaller than the wavelength of the electromagnetic radiation, if the radiation's wavelength is optimal, the electrons oscillate coherently producing a localized surface plasmon (Figure 2.7). Surface plasmons are the coherent oscillation of electrons that exist at the interface between two materials where the real part of the dielectric constant changes sign [40]. This condition is met with metal-air and metal-water interfaces when the real part of the dielectric constant of the metal is negative. Localized surface plasmons are surface plasmons that are confined to metallic nanoparticles or nanostructures.

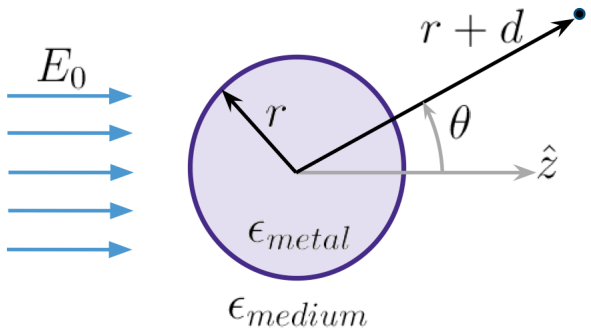

Figure 2.8: A dielectric metal sphere in a uniform electric field.

The enhancement of the signal is a result of the electric field of the incident radiation acting on the metal nanoparticle. This effect can be approximated by a dielectric sphere of radius r in a uniform electric field $E_0\hat{\mathbf{z}}$ (Figure 2.8). The electrons in the sphere will rearrange themselves into an induced dipole. The molecule at distance d away from the metal surface will then experience the electric field of the incident electromagnetic radiation and the electric field from the metal sphere.

$$\mathbf{E} = E_0\hat{\mathbf{z}} + \mathbf{E}_{sp} \tag{2.6}$$

The electric field from the dipole in spherical coordinates, $\mathbf{E}_{sp}$, is

$$\mathbf{E}_{sp} = \left(\frac{\epsilon^*_{metal} - \epsilon_{medium}}{\epsilon^*_{metal} + 2\epsilon_{medium}}\right)\frac{E_0 r^3}{(r+d)^3}(2\cos\theta\hat{\mathbf{r}} + \sin\theta\hat{\boldsymbol{\theta}}) \tag{2.7}$$

where ϵ^*_{metal} is the complex dielectric constant of the metal, ϵ_{medium} is the dielectric constant of the medium and θ is the angle with respect to the incident electric field. This results in strong electric fields at the surface of the sphere. The electric field enhancement factor, A, at a distance d away from the sphere is the ratio of the total electric field and the incident field.

$$A = \left|\frac{\mathbf{E}_0 + \mathbf{E}_{sp}}{\mathbf{E}_0}\right| \approx \left(\frac{\epsilon^*_{metal} - \epsilon_{medium}}{\epsilon^*_{metal} + 2\epsilon_{medium}}\right)\left(\frac{r}{r+d}\right)^3 \tag{2.8}$$

It is important to note the dependence on the material's dielectric constants. These parameters are strongly dependant on laser wavelength. The system is resonant

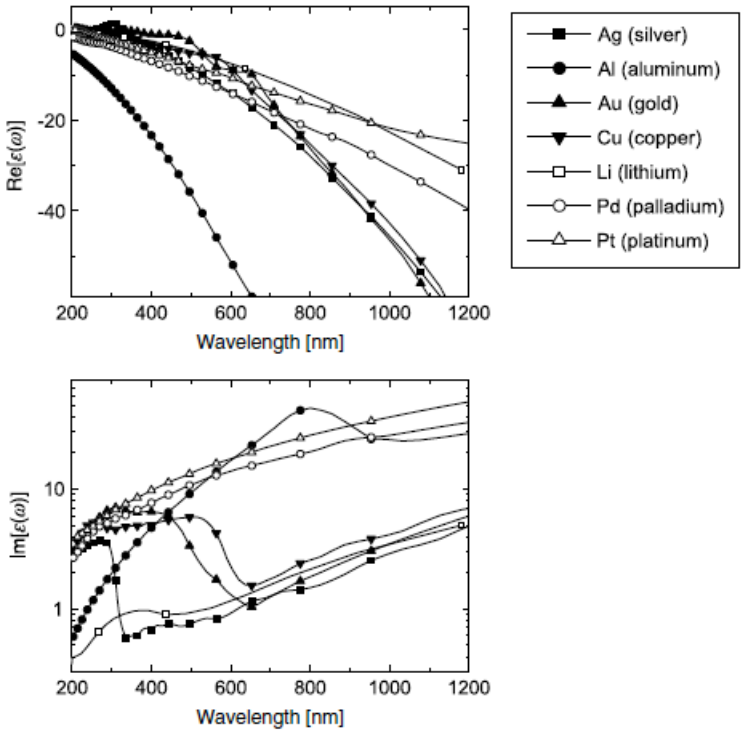

Figure 2.9: Overview of the dielectric constants of a selection of metals in the extended visible range. The real (top) and imaginary (bottom) parts of ϵ are plotted against wavelength. [41]

when $\epsilon^*_{metal} = -2\epsilon_{medium}$. The materials and laser frequencies are chosen to optimize this effect. A metal is suitable for use in SERS if it has a negative real part of the dielectric function and a small imaginary part of the dielectric function.

While many metals have a negative real part of their dielectric function (Figure 2.9), silver and gold are most commonly used. Metals like lithium and palladium present too much absorption, while aluminum is only suitable for applications in the UV. This has been demonstrated recently with the SERS of crystal violet on an Al surface [42]. Silver is the most promising metal. Gold and copper are also suitable, but only at longer wavelengths above 600 nm. At such wavelengths, the optical absorption of gold becomes comparable to that of silver. Copper is rarely used due to its chemical instability as well as relatively weaker SERS activity [43]. Finally, lithium also exhibits suitable properties but has not been used much because it reacts easily with water and does not occur freely in nature due to its chemical activity [41]. In this thesis, gold and silver were used.

The SERS effect is vastly pronounced because the field enhancement occurs twice. Initially, the field enhancement magnifies the intensity of incident light which will excite the Raman modes of the molecule, therefore increasing the signal of the Raman scattering. The radiative photons are then magnified by the same mechanism, resulting in a greater increase in the total output signal of the experiment. At each stage the electric field is enhanced as E^2, for a total enhancement of of intensity of E^4. The Raman signal will then be enhanced by a factor M:

$$M \approx \left| \frac{\epsilon_{metal} - \epsilon_{medium}}{\epsilon_{metal} + 2\epsilon_{medium}} \right|^4 \left(\frac{r}{r+d} \right)^{12} \tag{2.9}$$

M varies as $(r+d)^{-12}$ in our simple model. This agrees with the experimental observation that when 12 nm silver nanoparticles are coated by varying thicknesses of Al_2O_3 the Raman intensity of absorbed molecules decreases by a factor of 10 with 2.8 nm [12]. This distance will depend on the size of the nanoparticle. The molecules in direct contact with the metallic nanoparticle surface are the main contributors to the SERS signal. It is also important to note that in equation 2.7 the electric field is twice as large when $\theta = 0$ than when $\theta = 90°$. This will correspond to molecules attached to surfaces perpendicular to the electric field being enhanced 16 times more than molecules attached to surfaces parallel to the electric field.

2.3.3 Hot Spots

In addition to the signal enhancement you can get with a single nanosphere, specific geometries can result in even more localized areas with exceptional enhancements called hotspots. These hotspots can be divided into two categories (Figure 2.10):

- hotspots in the gaps between closely spaced particles
- hotspots at the tip of objects with sharp features.

In the case of nanospheres, hotspots occur in the gap between coupled metallic nanoparticles separated by a few nanometers. Calculations of the electric field strengths in the gap between adjacent nanoparticles typically reveal field strengths that are many orders of magnitude greater than the fields at the surface of a single metallic nanoparticle.

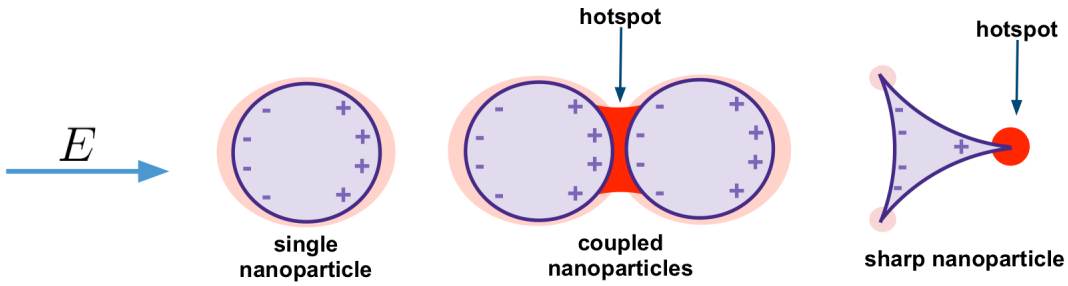

Figure 2.10: An illustration of electric field enhancement in the vicinity of a single metallic nanoparticle, coupled metallic nanoparticles and a sharp metallic nanoparticle. The spherical metallic nanoparticle electric field distributions are based on calculations by Mock et al. [44]. The triangular metallic nanoparticle electric field distribution is based on simulations made by Geldhauser et al. [45].

Sharp features can also produce larger field strengths but present strong laser polarization dependency [46]. These types of structures are often printed onto metal surfaces in arrays with different types of nanolithography.

2.3.4 Tip Enhanced Raman Spectroscopy (TERS)

TERS combines the unique vibrational signatures available from Raman scattering, the sensitivity provided by SERS, and the nanoscale spatial resolution provided by atomic force microscopy. A metal probe approaches the sample from above and excitation of surface plasmons in the metal tip gives localized enhancement under the tip. The tip can then be scanned across the sample while taking enhanced Raman spectra.

In TERS, the enhancement arises from the electromagnetic fields near the surface of a tip. Like in SERS, only molecules in the close vicinity of the tip will display enhanced Raman scattering intensity. In tapping mode experiments by Ichimura et al. Raman intensity was found to decrease by a factor of e, 2.8 nm away from the surface from a 28 nm silver coated tip [11]. Because AFM tips have radii of curvature on the nanometer scale, TERS allows for the collection of nanoscale resolution Raman maps.

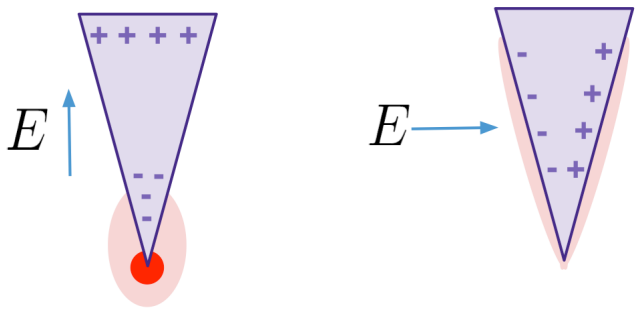

Figure 2.11: An illustration of electric field enhancement in the vicinity of an AFM tip under plane wave laser illumination irradiated sideways and from the bottom. Enhancement distribution is based on simulations by Micic et al. [47].

The field enhancement originates from a combination of the electrostatic lightning-rod effect (Figure 2.11), which is due to sharply pointed structures, and localized surface plasmons. The lightning rod effect is dependent of the tip geometry and the orientation of the excitation source. When the incident polarization is perpendicular to the tip axis, the surface of the tip sides have opposite charges. As a consequence, the end of the tip remains uncharged and no field enhancement is achieved. On the other hand, when the incident polarization is parallel to the tip axis, the induced charge density has the highest amplitude at the end of the tip. To establish a strong lightning rod field enhancement at the tip, the electric field of the exciting laser beam needs to have a component that is polarized along the tip axis.

Influenced by this polarization dependance there are two common TERS set-ups: illuminating from the side and illuminating from the bottom (transmission). Illumination from the side, with a laser beam at an angle of 45 degrees with respect to the tip, takes advantage of the lightning rod effect. This set-up has the potential of higher Raman enhancements. However, one of the disadvantages of illuminating from the side is a strong background signal from the tip and other optical elements in the laser path. Additional reduction in signal intensity is attributed to shadowing of the laser spot by the tip. This set-up is also more difficult to align. Bottom illumination only uses the localized surface plasmons on the tip as an enhancement mechanism. This can be achieved by using rough surfaces with grains of the appropriate size to support plasmons or a plasmon resonant structures attached or etched into the apex

of the tip. This method is limited to thin transparent samples or nano-objects on transparent slides. This type of illumination was used in this thesis.

Chapter 3

Experimental Methods

3.1 Raman Set-up

The aim of Raman spectroscopy is to measure the scattered signal intensity versus the shift in frequency from the incident light source. This can be done by separating the wavelengths spatially on a multichannel detector. The Raman spectrometer can be divided into 3 main components: the excitation source, the illumination and collection optics and a detection system consisting of a dispersive element (spectrograph) and multichannel detector (Figure 3.1).

3.1.1 Excitation Source

Continuous wave lasers are the preferred excitation source in Raman spectroscopy. They are highly monochromatic, stable and are almost completely linearly polarized. In our experimental set-up we have 532 and 660 nm solid state lasers (Ventus Vis, Laser Quantum). The power of the lasers were adjusted to 5 mW for bulk Raman experiments and 100μW for enhanced Raman experiments to avoid damaging the sample.

3.1.2 Optics

The set-up used in this thesis includes a transmission Raman set up with an inverted microscope (Olympus IX71). The laser and collection optics are collinear. This is a popular choice especially in combination with microscopes. The laser is focused onto the sample from below through a 100X, 1.3 NA oil immersion aperture. This creates a 1 μm laser spot. The stage that the sample sits on is controlled by piezoelectrics in the x and y direction. This can be utilized to position the laser on the desired sample feature. The scattered light is then collected by the same aperture. The high numerical aperture of the objective is essential to collect the maximum amount of

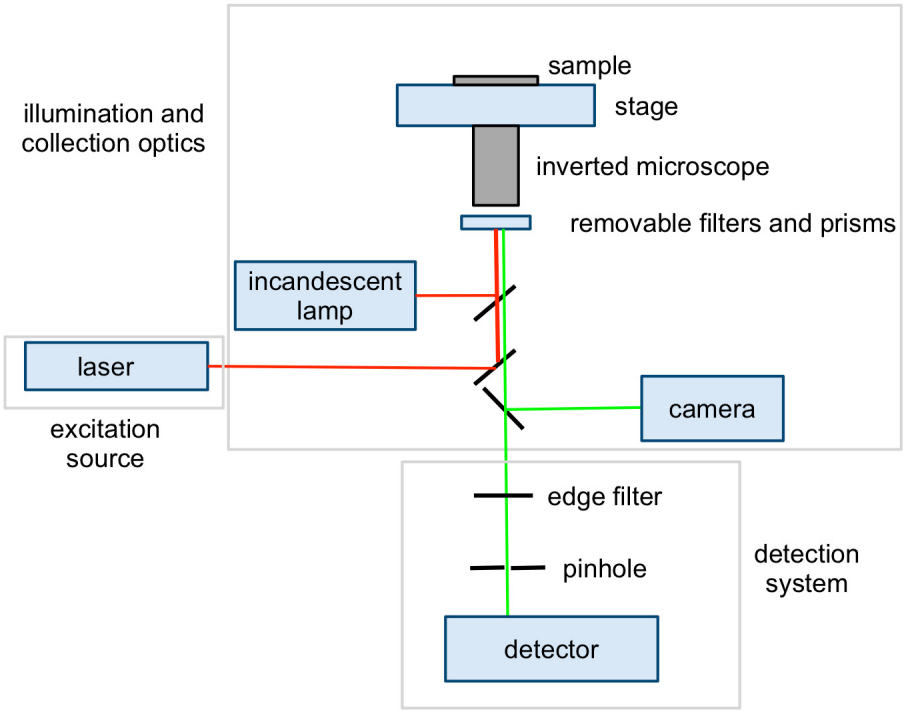

Figure 3.1: A diagram of the Raman set-up.

scattered light. An incandescent light source (either a halogen lamp or a conventional incandescent light bulb) can also be used instead of the laser to optically view the sample. This light scattered by the sample is then either sent to a camera (when illuminated by a light source) or to the detector (when excited by the laser). Filters and prisms can also be added into the path of the light to use Differential Interference Contrast (DIC) microscopy when viewing the sample.

3.1.3 Detection

After interacting with the sample, the scattered light is directed to the detector. The detector used in this set-up is an iHR550 Raman Spectrometer (Horiba Jobin Yvon). The light is split with a diffraction grating and then detected with a peltier-cooled electron multiplied CCD. In order to obtain high signal-to-noise in Raman measurements, it is necessary to block Rayleigh scattering from reaching the detector while transmitting the Raman signal. The light passes though an edge filter that only transmits the Stokes signal. The scattered light also passes through a pinhole that obstructs out of focus light. This obstructed light can include light from adjacent spatial regions, fluorescent emission and light not originating from the focal plane of the objective lens.

3.2 SERS Set-up

As mentioned in the previous chapter, gold and silver are commonly used to enhance Raman signal. Gold is used with the 660 nm laser and silver is used with the 532 nm laser. A solution of metallic nanoparticles suspended in water is deposited on a sample. Unattached nanoparticles are washed away. Experiments are either performed in air or water.

SERS samples were prepared in a variety of ways. Dried collagen I fibrils adsorbed onto glass were covered with either a solution of either Ag or Au nanoparticles. The nanoparticles were either purchased from nanoCompsix or Nanopartz or produced and characterized in the laboratory of Professor Kevin Hewitt by Leanne Lucas. Silver polydisperse nanoparticles were formed by heating a 0.02% $AgNO_3$ solution to boil and adding 1% sodium citrate [48]. The solution was then stirred. When the nanoparticles formed, the transparent solution turned yellow. Gold nanoparticles

were formed by heating 0.01% $HAuClO_2{\cdot}3H2O$ solution to boil and adding 1% sodium citrate solution. The solution then changed from colourless to reddish purple.

3.2.1 AFM

A Veeco Bioscope II atomic force microscope was used in this thesis. All samples were imaged in contact or tapping mode in air. For contact mode imaging Veeco MSNL cantilevers with 0.03 and 0.1 N/m nominal spring constants were used as well as Nanoworld CONT cantilevers with a 0.2 N/m nominal spring constant. For tapping mode imaging, we used a Veeco TESP-SS cantilever with a 42 N/m nominal spring constant and a resonance frequency of 300 kHz. The amplitude of oscillation was set to 10 nm for both imaging and Raman scattering data collection. A scan rate of 1 Hz was used to produce 512x512 pixel images. A closed loop feedback system in the x, y and z direction was used for all scans. All the images were analysed with Gwyddion (http://gwyddion.net/).

TERS tips were prepared using evaporated Ag films. Silicon AFM tips were coated with 30 nm of Ag via thermal evaporation deposition. The evaporation was performed in an evaporator (model 4, Edwards, West Sussex, UK) with a background pressure between 10^{-5} and 10^{-6} Torr. Ag was heated in a tungsten basket with the cantilevers 12-15 cm above the Ag source. The average deposition rate was around 10 nm/min with the thickness being monitored by a quartz microbalance. Tips were used within one week of deposition.

3.3 TERS Set-up

3.3.1 Tip Alignment

The alignment of the laser spot onto the AFM tip (Figure 3.2) was a multistep process. The AFM tip was brought 1.5 mm away from the sample surface. The tip was found optically with a 10X objective and centered in the field of view. The tip was then brought 1 mm away from the surface, found optically with a 40X objective and centered. The AFM head was then lifted from the stage and the sample was viewed with a 100X oil immersion objective. An appropriate area of the sample was found by moving the sample with the AFM stage. The head was then put back on

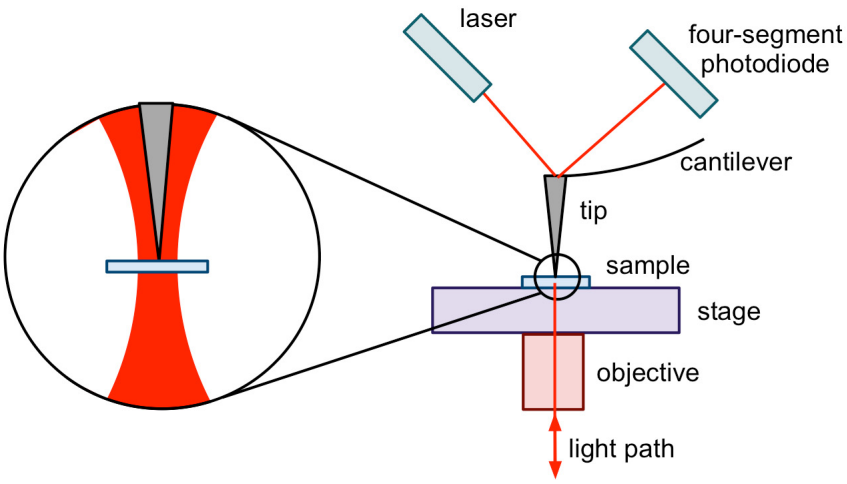

Figure 3.2: A diagram of the TERS set-up.

the stage and allowed to approach the sample. When in contact with sample, the tip appears as a small black dot. The focus was adjusted to the focal position where the black dot just appeared. The dot was also moved to the position where the center of the laser hits the sample. The collagen fibrils (or desired sample aspect) were then moved to the tip by the AFM stage while the tip was out of contact with the sample.

3.4 Sample Preparation

Rat tail collagen I with a concentration of 1mg/ml in 20mM acetic acid was purchased from Sigma. For enhanced Raman experiments, assembly was induced by diluting collagen I to 0.1 mg/ml in phosphate buffered saline (PBS). 1 ml samples were incubated in a 37°C water bath for 1 hour. A 0.5 ml aliquot was deposited on a clean glass-bottom Petri dish. After 30 min, the sample was washed with deionized water and dried with nitrogen gas. For bulk Raman experiments, collagen I was diluted to 0.45 mg/ml in PBS and incubated 17 hours to form a clump of fibrils. Every other step remained unchanged. To form a collagen sheet, collagen was diluted to 0.5 mg/ml in a 20 mM Tris, 100 mM NaCl buffer. A 20 μl aliquot was deposited on a clean glass-bottom Petri dish. The sample was washed and dried after 17 hours.

3.5 Data Analysis

Spectra were fitted in LabSpec (Horiba Jobin Yvon) using Gaussian functions to determine position, intensity and widths of the peaks. The bulk Raman spectrum of collagen I fibrils underwent background subtraction as well as smoothing by a filtration of degree 2 and size 9 in LabSpec. The spectrum of a sheet of collagen underwent background subtraction. The Amide I band of this spectrum was then fit with multiple Gaussian functions. The enhanced Raman spectra were not altered with smoothing or background subtraction. The enhancement factor (M) of a Raman spectrum was calculated from the enhanced peak intensity ($I_{enhanced}$) and the non-enhanced noise intensity ($I_{non-enhanced}$) as well as the scattering area radius for enhanced ($r_{enhanced}$) and non-enhanced scattering ($r_{non-enhanced}$) (Equation 3.1). The radius of scattering had to be estimated. The laser spot is around 1 μm in diameter so the non-enhanced scattering radius was estimated to be 500 nm. The radius of enhanced scattering was harder to estimate. The SERS spectra were likely the result of hot spots in clusters of nanoparticles and the TERS spectra were likely the result of the rough surface of the tip. The enhanced scattering radii were estimated to be the radius of the nanoparticle or tip used.

$$M = \left(\frac{I_{enhanced}}{I_{non-enhanced}}\right)\left(\frac{r_{non-enhanced}}{r_{enhanced}}\right)^2 \tag{3.1}$$

Chapter 4

Surface Enhanced Raman Spectroscopy

Raman spectroscopy is an important tool for the determination of structures of proteins. Surface enhanced Raman spectroscopy (SERS) overcomes the long collection times inherent in normal Raman spectroscopy. It makes it possible to view vibrations in small amounts of molecules that would be undetectable with far field Raman. The small area probed by SERS also makes it possible to probe the surface of biological structures which is one of the key determinants of their biological functions. Using SERS to study collagen I fibrils will provide valuable information about the secondary structure of the molecules and the amino acid residues at their surface.

4.1 Nanoparticle Characterization

A variety of metallic nanoparticles were used. Silver and gold nanoparticles were either purchased from nanoComposix, Nanopartz or produced by Leanne Lucas following a citrate reduction protocol described in section 3.2.

4.1.1 Nanoparticle Size and Plasmon Resonance

The most common way to characterize SERS metallic nanoparticles is to measure their plasmon resonance. This can be done either using the absorption spectra or the scattering spectra of the nanoparticles. Both SERS and TERS rely on the anomalous scattering of nanoparticles. Unfortunately it is difficult to measure, so most research groups rely on the absorption spectrum that can be measured in solution using a UV/Vis spectrometer. The nanoparticles used in this thesis were measured by absorption in aqueous form.

It is believed that the maximum SERS enhancement arises when the actual plasmon resonance is halfway between the wavelength of the exciting radiation and the scattered light [49]. Both the scattered and the exciting radiation's wavelength must be close to the resonance to take advantage of the E^4 enhancement. If the plasmon

resonance is near the exciting radiation's wavelength, vibrational modes with small Raman shifts will be more intense than the large Raman shifts. Similarly, if the plasmon resonance is highly red shifted, the large Raman shifts will be more intense.

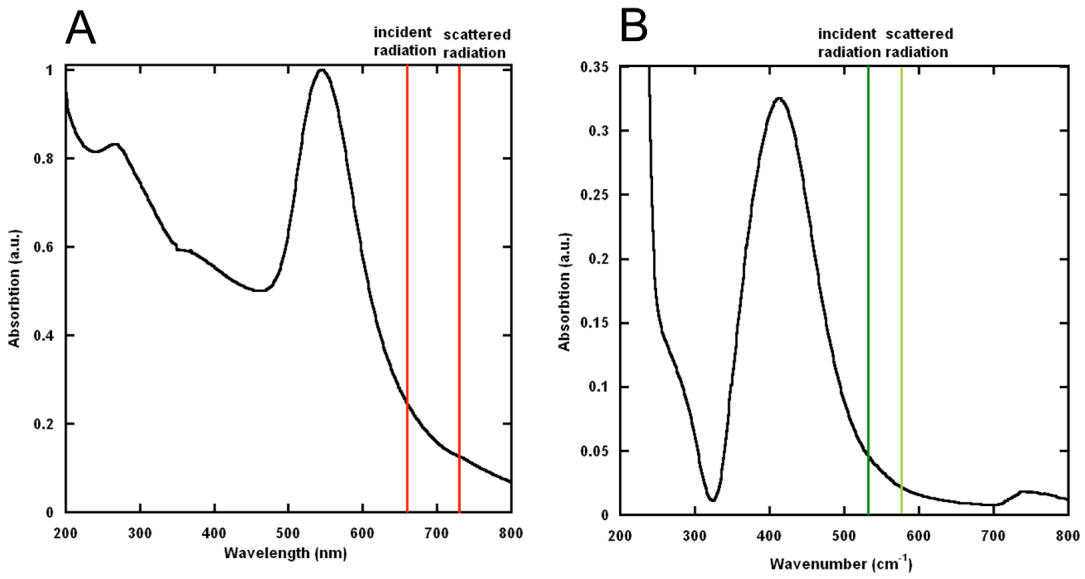

Figure 4.1: Absorption spectra of nanoparticles. A) The absorption spectrum of 65 nm gold nanoparticles. The peak absorption is 545 nm. The laser excitation wavelength (660 nm) and the scattered radiation wavelength for a 1500 cm^{-1} peak (733 nm) are highlighted. B) The absorption spectrum of 45 nm silver nanoparticles. The peak absorption is 413 nm. The laser excitation wavelength (532 nm) and the scattered radiation wavelength for a 1500 cm^{-1} peak (568 nm) are highlighted.

However, finding the appropriate nanoparticle to use for a given apparatus is mostly a trial and error process. We found that 65 nm gold nanoparticles and 45 or 34 nm silver nanoparticles were good SERS scatterers for our 660 and 532 nm lasers respectively. However the absorption spectra of the particle suggests plasmon resonances approximately 150 nm too low in wavelength (Figure 4.1). Due to the absorption of nanoparticles to the sample, the nanoparticle configuration is often different from the one in the measured solution. It has been found in nanoparticle arrays of gold and silver nanoparticles that plasmon resonance is shifted with decreasing nanoparticle separation [50, 51]. The plasmon resonance appeared strongly red-shifted, exponentially decaying with increasing distance, when the exciting radiation was polarized along the nanoparticle pair's axis [50, 51]. For light polarized

perpendicular to the particle axis, there was a weak blue shift [51]. Silver nanoparticles separated by 10 nm were red-shifted approximately 100 nm from nanoparticles separated by 25 nm and approximately 150 nm from single nanoparticles [51]. Gold nanoparticles also exhibited a strong effect, with a 60 nm red-shift for nanoparticles separated by 54 nm when compared to single nanoparticles [50]. The nanoparticles investigated in this thesis had a colloidal plasmon resonance below the excitation laser's wavelength (Table 4.1). This indicates that we obtained SERS spectra from clusters of nanoparticles rather than single ones.

Company	Material	Diameter (nm)	Maximum colloidal absorption wavelength (nm)
Nanopartz	Gold	32±2	524
Nanopartz	Gold	40±7	527
Nanopartz	Gold	50±4	534
Nanopartz	Gold	60±4	536
Nanopartz	Gold	72±5	543
Nanopartz	Gold	82±4	550
Nanopartz	Gold	90±4	563
	Gold	18±5	521
	Gold	45±8	528
	Gold	45±5	530
	Gold	47±15	541
	Gold	**65±11**	**545**
NanoComposix	Silver	9.5±1.5	391
NanoComposix	Silver	20.0±2.4	400
NanoComposix	**Silver**	**34.4±3.4**	**504**
NanoComposix	Silver	49.1±4.5	418
NanoComposix	Silver	57.7±5.0	431
NanoComposix	Silver	69.0±4.9	451
	Silver	**45±25**	**413**

Table 4.1: The physical properties of the colloidal nanoparticles tested in this thesis. The optimal plasmon resonance for a 1500 and 1000 cm^{-1} peak when excited with a 660 nm laser would be 697 and 684 nm respectively. The best results were found with the 65 nm gold particles (545 nm absorption). The optimal plasmon resonance for observing a 1500 and 1000 cm^{-1} peak with a 532 laser would be 578 and 562 nm respectively. Good SERS spectra were achieved with the 34 nm (504 nm absorption) and 45 nm silver nanoparticles (413 nm absorption). The nanoparticles used in this section are in bold.

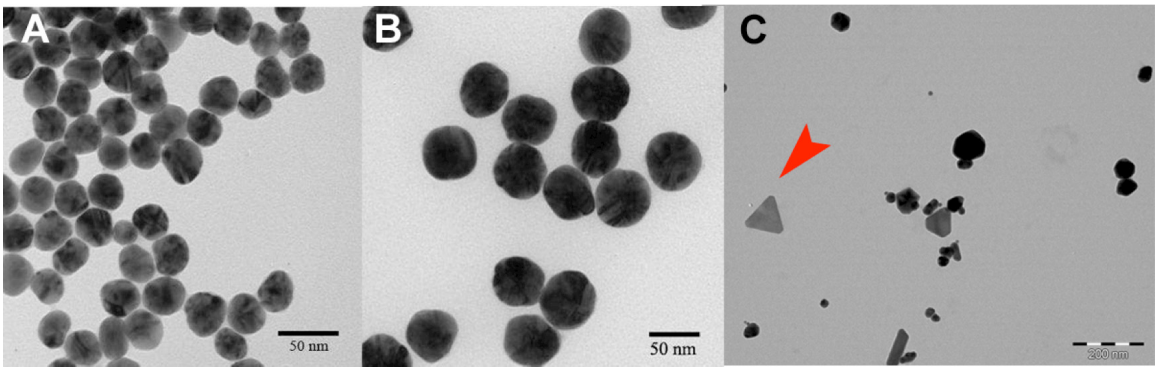

Figure 4.2: TEM images of silver nanoparticles. A) 34 nm silver nanoparticles purchased from nanocomposix (image provided by nanocomposix) B) 50 nm silver nanoparticles purchased from nanocomposix (image provided by nanocomposix) C) 45 nm polydisperse silver nanoparticles. A sharp nanoparticle is featured with an arrowhead.

4.1.2 Nanoparticle Shape

The shape of the nanoparticles also varied with manufacturing method. As revealed by Transmission Electron Microscopy (TEM) images of the nanoparticles (Figure 4.2A,B), the purchased nanoparticles had a more uniform spherical shape. They have the distinct advantage of being consistent. The nanoparticles made in house (Figure 4.2C) had much more variation. There was a greater variation in size and a greater variation in shape including nanoparticles with sharp features that can produce greater enhancements (Figure 4.1C arrowhead). However, these sharp features are strongly dependent on polarization orientation, resulting in many inactive nanoparticles.

4.1.3 Nanoparticle Distribution on Collagen I fibrils

It is important that the metallic nanoparticles are in contact with the fibrils being examined. For this reason, nanoparticles were attached to the sample then washed with water to remove any floating nanoparticles. The nanoparticles were visible with Differential Interference Contrast (DIC) microscopy in water. The fibrils were also imaged in air with AFM. Silver nanoparticles were found to preferentially attach to the fibrils over the glass (Figure 4.3A). They were also found to attach in nanoparticle clusters (Figure 4.3B). The gold nanoparticles preferentially absorbed to the fibrils

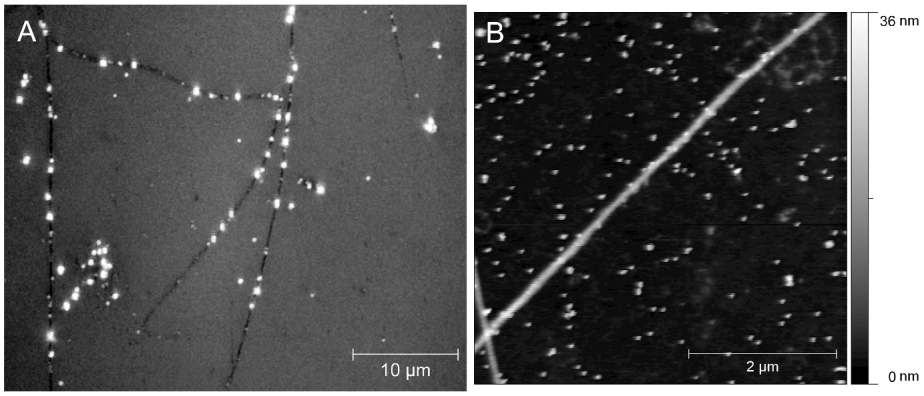

Figure 4.3: Distribution of silver nanoparticles on collagen I fibrils. A) DIC image of several collagen I fibrils coated with polydisperse 45 nm Ag nanoparticles. Each bright dot corresponds to at least one nanoparticle. The collagen fibrils are represented by dark lines. B) AFM height image of 34 nm Ag nanoparticles attached to collagen fibrils on glass obtained with a 0.03 N/m MSNL cantilever.

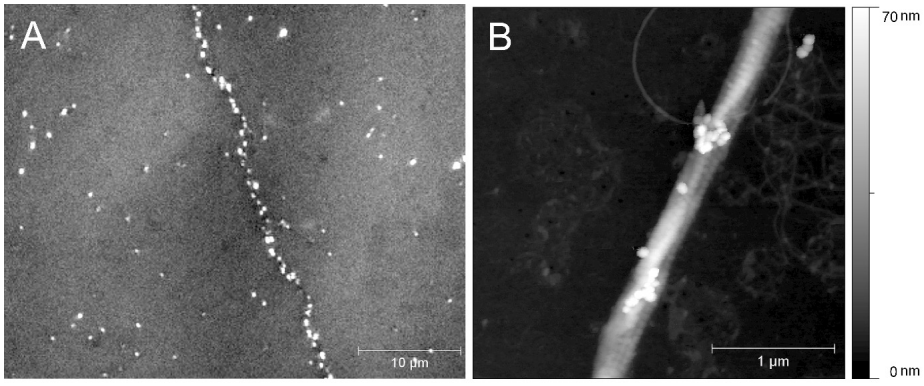

Figure 4.4: Distribution of gold nanoparticles on collagen I fibrils. A) DIC image of a collagen I fibril coated with 65 nm Au nanoparticles. Each bright dot corresponds to at least one nanoparticle. B) AFM tapping mode height image of 65 nm Au nanoparticles attached to collagen fibrils on glass obtained with a TESP-SS cantilever

and bound to the fibril in clusters (Figure 4.4). In the 65 nm gold nanoparticle AFM image, it was apparent that the nanoparticles attached between the gaps in the 67 nm banding pattern (Figure 4.4B).

4.1.4 Background Spectra

Materials other than collagen affect the Raman spectra in the form of background spectra. The collagen vibrational modes examined in this thesis are predominately found in the 600-1800 cm^{-1} region. Any peaks in this region that could be attributed to background should be taking into consideration. The nanoparticles themselves produce a Raman spectra. Although gold and silver lattices do not produce a Raman spectrum, chemisorption takes place. At the surface of the metal, bonds such as Ag-N, Ag-O, Ag-S form and are observed in the 100-300 cm^{-1} region [52]. Luckily these bands do not interfere with most of the bands associated with collagen. The other materials that have the possibility of contributing are water, the PBS that the collagen was assembled in and the glass the collagen is absorbed to. Water is a weak Raman scatterer [53]. In addition, its O-H stretching modes are in the 3200-3700 cm^{-1} region [54]. This makes it possible to study the collagen in aqueous solution. PBS is composed of NaCl, KCl, Na_2HPO_4 and KH_2PO_4. Although the sample is washed with water after assembly, it is possible for some of the buffer to remain. The Na^+, K^+ and Cl^- ions will not produce Raman bands, however the PO_4^{3+} has the potential to interfere with the collagen spectra. It's strongest peak is at 936 cm^{-1} with a second weaker peak at 1022 cm^{-1} [55]. Unfortunately the 1022 cm^{-1} is at the same frequency as a phenyl ring vibration. In far field Raman the glass spectrum dominates the Raman spectra and is subtracted. In SER spectra, its contribution is limited by using a small pinhole and low laser intensities. Spectra of both silver and gold nanoparticles in water in a clean glass dish do not reveal any strong peaks (Figure 4.5). The band from the nanoparticle surface bonds is present in both spectra.

4.1.5 Spectral Fluctuations and Sample Environment

In SERS spectra, fluctuations in the positions and intensities of peaks with time has been widely observed [56, 57, 58, 59, 60, 61, 62, 63]. In a series of subsequently measured SERS spectra, one can usually observe some fluctuations of every Raman

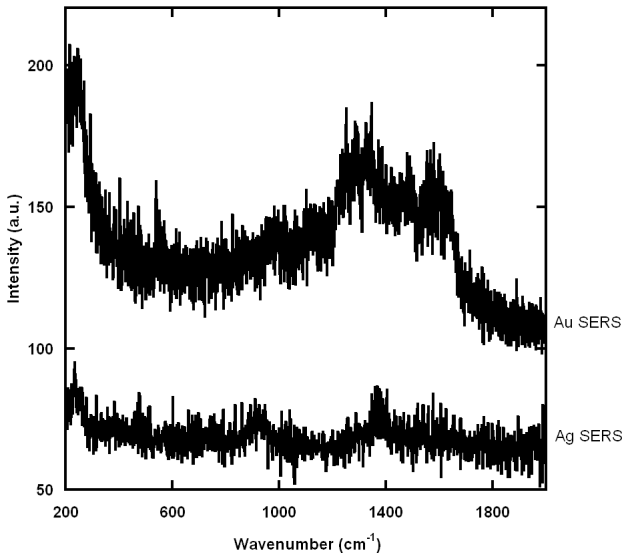

Figure 4.5: Background spectra of the SERS nanoparticles. Spectra of 65 nm Au and 34 nm Ag nanoparticles were taken on clean glass in water. The spectra were collected under the same conditions as the SER spectra of collagen fibrils.

band. The SERS signal is scattered by a very small part of the molecules residing in areas of high Raman enhancement. The observed spectral fluctuations can only be significant when both the number of the Raman active molecules and the sampling area are small; fluctuations are averaged out when the number of Raman active molecules is high [63].

There are several theories that attempt to explain spectral fluctuations. It is sometimes attributed to the detection of single molecules [58, 63, 60, 61]. The intensity fluctuations are considered a characteristic of single molecule detection [58]. However, spectral fluctuation alone is not enough evidence to classify it as a single molecule spectrum [60]. Spectral fluctuations have also been assigned to changes in the molecules absorption states with different spectral characteristics [57, 58] and surface diffusion of adsorbates [58, 59].

With our SERS system, nanoparticles were placed on top of the collagen sample in water. When the sample was viewed with a microscope, it became apparent that poorly attached nanoparticles were diffusive. For that reason the sample was rinsed to remove unattached nanoparticles. However, the attached nanoparticles could still move locally at the fibril surface thus causing spectral fluctuations. Spectra taken in

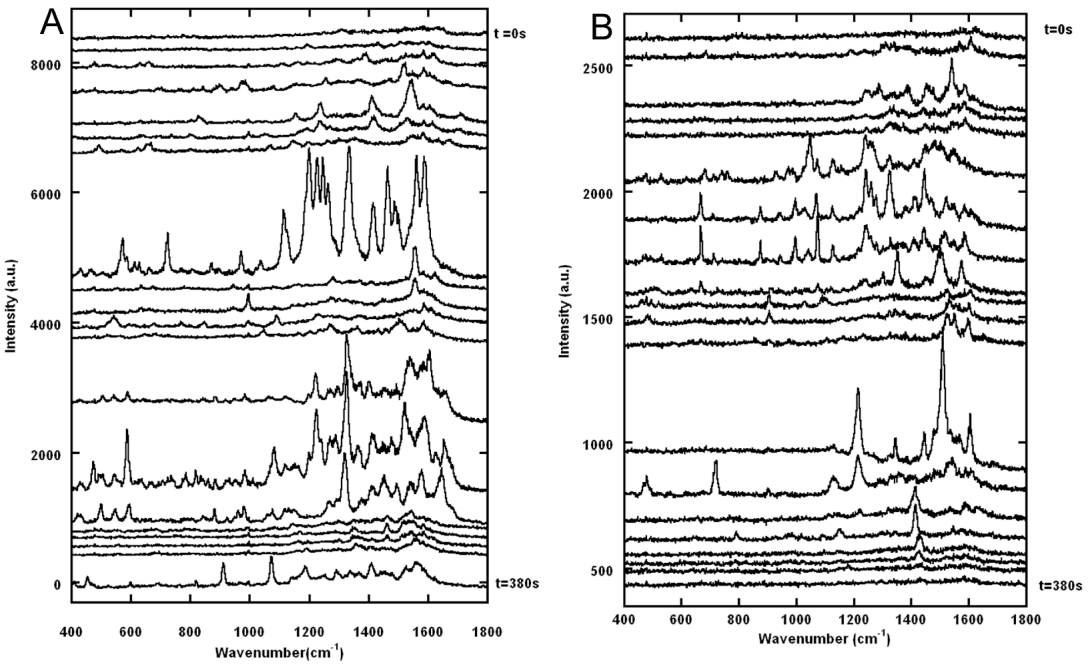

Figure 4.6: The spectral fluctuations with time of a collagen sample covered with 65 nm Au nanoparticles in water. Each spectrum was taken with a 660 nm laser adjusted to 100 μW. The acquisition time of a spectrum was 10 s per window (20 s total). A) 20 spectra taken in secession at a single spot. B) 20 spectra taken in succession at a different spot.

succession reveal highly varying spectral intensities and peak positions (Figure 4.6). There were periods of time with similar spectra that would end abruptly and a group of spectra with different peak positions would arise.

To test if these spectra variations were a result of diffusion in a aqueous environment, the same experiment was carried out with a dried sample. The dry sample displayed a decrease in spectral fluctuations (Figure 4.7). There was however some clear fluctuations that happened slower and with less intensity than the sample in water. These results suggest that the spectral fluctuations in our experiments were diffusion-based. The nanoparticles in the dry sample are strongly bound to the fibrils and show less spectral variation than the weakly bound nanoparticles in the wet sample.

Another spectral change with time to consider would be heat damage. Sample heating can change the surface structure of the nanoparticles which can lead to weaker field enhancement and signal losses [58]. The intensity of the spectra does not seem to

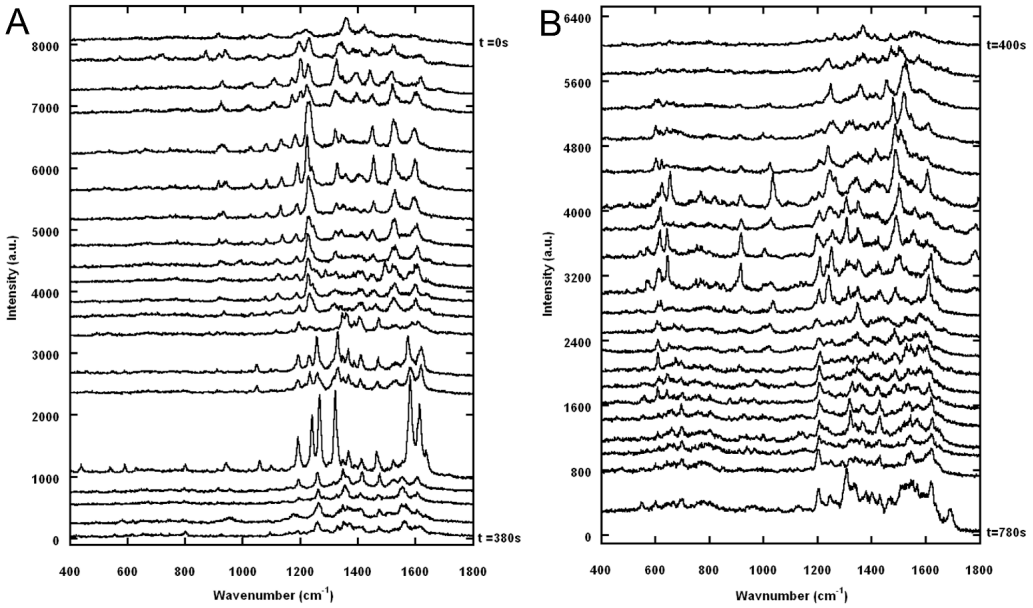

Figure 4.7: The spectral fluctuations with time of a dried collagen sample covered with 65 nm Au nanoparticles. Each spectrum was taken at a single spot with a 660 nm laser adjusted to 100 μW. The acquisition time of a spectrum was 10 s per window (20 s total). A) The first 20 spectra taken in secession. B) The next 20 spectra taken in succession.

significantly decrease with time in either the dry or wet environments. There is also a possibility of sample degradation after exposure to SERS high electric fields [60]. This type of damage is harder to observe. It would not change the spectra drastically enough to differentiate this effect from diffusive spectral fluctuations. Heating can also cause carbon contamination. If a nanoparticle can enhance the signals of the sample, it can also enhance the signals of carbon contaminants either arising from the environment or produced from a decomposed sample [64]. When looking at organic samples this can be a problem as many of the carbon contamination bands could be confused with the bands of the sample. Carbon contamination results in a broad band structure with peaks around 1580 and 1350 cm^{-1} [60, 65]. It is possible that the last few spectra from the dry SERS experiment are due to carbon contamination (Figure 4.7B). However, both sample heat damage and carbon contamination do have less of a chance to occur if spectral acquisition times are kept low and if the measurements are taken in a wet environment as opposed to a dry one due to the ability of the former to disperse heat faster.

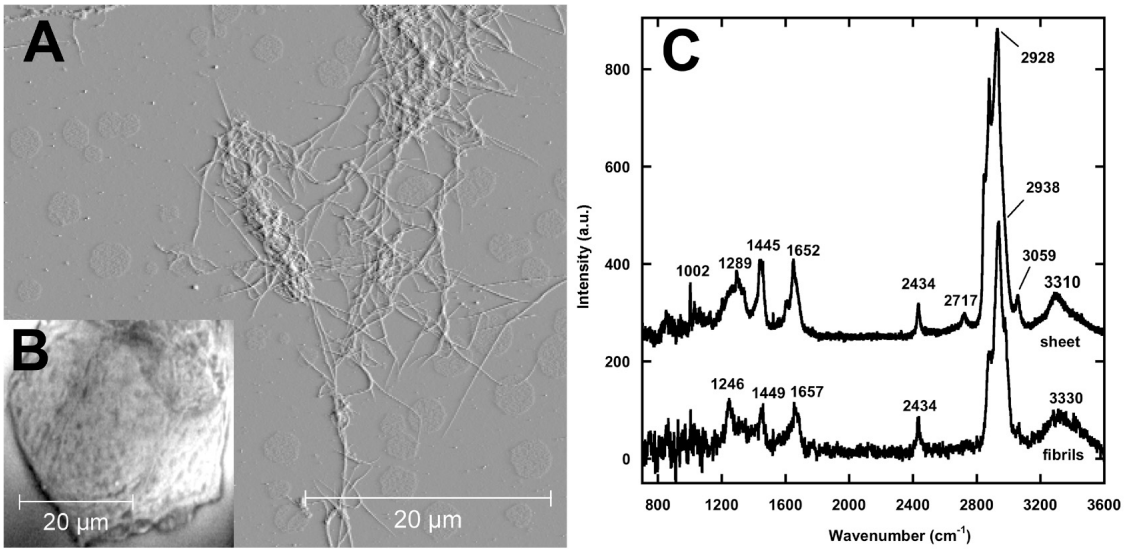

Figure 4.8: Far field Raman spectrum of collagen I fibrils. A) Contact mode AFM deflection image in air of a dense network of fibrils obtained with a 0.01N/m MSNL cantilever. B) Optical image of a sheet of collagen type I fibrils C) Raman difference spectra of the sheet and a dense network of fibrils. Positions of the major bands are indicated. The 2434 cm^{-1} band is attributed to glass. The FWHM of the Amide I bands are 90 cm^{-1}.

A dry environment displays less spectral fluctuations, which would be an advantage when doing any experiments that require to take multiple spectra at the same location and compare them. If less concerned with spectral fluctuations than sample damage and carbon contamination, a wet environment is a better choice. In the case of protein, wet samples provide near physiological conditions. For the most part we were not concerned with spectra fluctuations and used a wet environment for SERS experiments in this thesis.

4.2 Results

4.2.1 Reference Spectra

Collagen I fibrils adsorbed onto glass were imaged by AFM in air. We observed two types of structures, dense networks of fibrils (Figure 4.8A) and sheets of fibrils several microns in thickness (Figure 4.8B). Both spectra were dominated by the Raman scattering of the glass substrate. Subtracting a spectrum of clean glass allowed us to obtain spectra with a typical collagen fingerprint (Figure 4.8C), characterized by

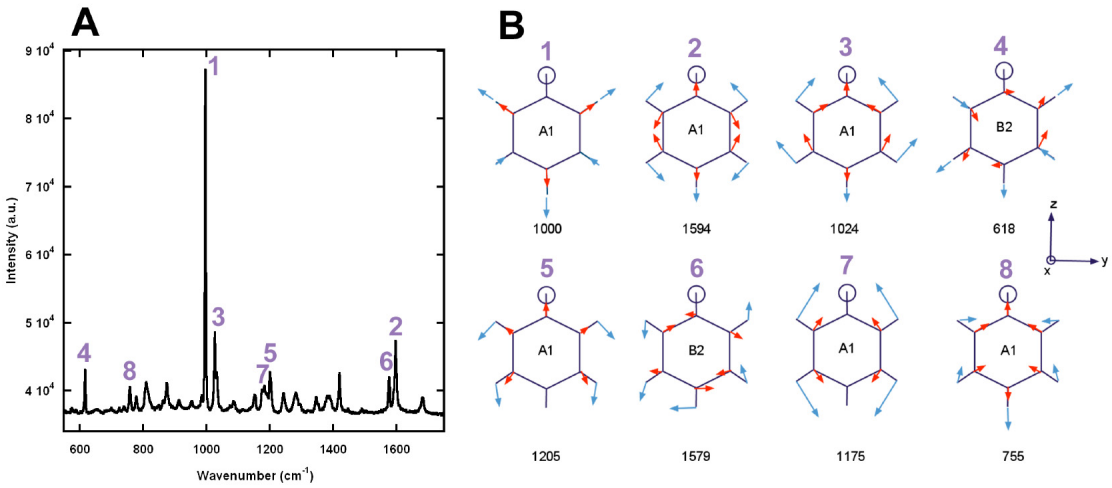

Figure 4.9: The vibrational modes of Phe-Phe nanotubes. A) Far field Raman difference spectrum of Phe-Phe nanotubes. B)The 8 strongest phenyl ring vibrations observed in the Phe-Phe spectrum in decreasing order. The circle denotes where the ring is attached to the backbone. The displacements of the H and C atoms are represented by arrows [70]. All vibrations shown are in-plane. Each mode is labelled by the vibration's accepted wavenumber and symmetry species [70]. The A_1 modes have xx, yy and zz polarizability components. The B_2 modes have xy polarizability components.

five bands. The Amide III and I bands were observed at 1268±22 and 1655±3cm^{-1} [66, 67, 68]. The 1447±2 and 2933±5 cm^{-1} bands are associated with CH_2 and CH_3 deformations and the 3320±10 cm^{-1} band is attributed to NH stretching [66, 67, 68].

The far field Raman spectra of the collagen sheet also contained a 1002 cm^{-1} peak. This peak is characteristic of the symmetric ring breathing mode in the amino acid phenylalanine. This peak has been observed in other bulk collagen Raman spectra in previous studies [66, 67]. For this reason a bulk Raman reference spectrum of phenylalanine was taken as well (Figure 4.9A).

Di-phenylalanine (Phe-Phe) nanotubes were assembled by diluting 100 mg/ml of Phe-Phe in HFP (1,1,1,3,3,3-hexafluoro-2-propanol) to 1 mg/ml (10 μl Phe-Phe 990 μl water) [69]. The solution was then deposited on a glass bottomed Petri dish and dried with nitrogen. The Phe-Phe nanotube Raman spectrum was taken by exposing the sample to a 532 nm green laser adjusted to 5mW for 25 seconds.

The spectra of Diphenylalanine tubes revealed many peaks including a very strong

$1000\,\mathrm{cm}^{-1}$ peak. Most peaks were assigned to well-documented phenyl ring vibrations [70] (Table 4.2 p46). Interestingly, the strongest modes were often highly symmetric vibrations (Figure 4.9B).

As mentioned in subsection 2.3.1, the Raman scattering of a molecule is proportional to $\left(\frac{\partial\hat{\alpha}}{\partial\mathbf{q}}\right)_0 \mathbf{E}_0$. Only vibrations in a molecule that result in a change in the polarizability tensor of the molecule will yield a Raman active mode. The polarizability tensor, $\hat{\alpha}$, is a 3x3 matrix.

$$\hat{\alpha} = \begin{vmatrix} \alpha_{xx} & \alpha_{xy} & \alpha_{xz} \\ \alpha_{yx} & \alpha_{yy} & \alpha_{yz} \\ \alpha_{zx} & \alpha_{zy} & \alpha_{zz} \end{vmatrix} \tag{4.1}$$

The tensor describing the changes in polarizability is called the Raman tensor, $\hat{R}$ [41, 52].

$$\hat{R} = \left(\frac{\partial\hat{\alpha}}{\partial\mathbf{q}}\right)_0 = \begin{vmatrix} \alpha'_{xx} & \alpha'_{xy} & \alpha'_{xz} \\ \alpha'_{yx} & \alpha'_{yy} & \alpha'_{yz} \\ \alpha'_{zx} & \alpha'_{zy} & \alpha'_{zz} \end{vmatrix} \tag{4.2}$$

The Raman tensor is symmetric and its trace is invariant [52]. I will refer to the Raman tensor elements as polarizability components of a vibrational mode. A mode is considered to have an xy component if the α'_{xy} element in the Raman tensor is nonzero. These components dictate if a vibrational mode will be viewed in a Raman spectrum based on the molecules orientation with respect to the polarization of the incident radiation ($\mathbf{E}_0$).

$$\mathbf{E}_S \propto \hat{R} \cdot \mathbf{E}_0 \tag{4.3}$$

The observed Raman intensity of the vibrational modes will depend on the polarization of the incident ($\hat{\epsilon_0}$) and scattered light ($\hat{\epsilon_s}$).

$$I \propto \left|\hat{\epsilon_s} \cdot \hat{R} \cdot \hat{\epsilon_0}\right|^2 \tag{4.4}$$

The polarization of the light you detect and your incident light can be chosen to select different vibrational modes. In order to get maximum enhancement in SERS, both the incident and scattered light must be polarized in the same direction ($\hat{\epsilon_0} = \hat{\epsilon_s}$).

The phenyl group belongs to the C_{2v} point group. Using group theory, the vibrational modes can be grouped by their polarizability components into symmetry species (Table A.1). The modes of the A_1 symmetry species have xx, yy and zz polarizability components (α'_{xx},α'_{yy},α'_{zz}). The other symmetry species, A_2, B_1 and B_2 only have xy, xz or yz polarizability components respectively. Similarly, the Raman-active vibrations in the tyrosine ring (D_{2h} point group) can be grouped into the symmetry species A_g, B_{1g}, B_{2g} and B_{3g}. The A_g modes have xx, yy and zz polarization components while the B_{1g}, B_{2g} and B_{3g} modes have xy, xz or yz components respectively.

Modes with xx, yy and zz polarizability components will be excited with any incident polarization. For example for incident light polarized in the z direction,

$$\mathbf{E}_S \propto \begin{vmatrix} \alpha'_{xx} & 0 & 0 \\ 0 & \alpha'_{yy} & 0 \\ 0 & 0 & \alpha'_{zz} \end{vmatrix} \begin{pmatrix} 0 \\ 0 \\ E_{0z} \end{pmatrix} = \begin{pmatrix} 0 \\ 0 \\ \alpha'_{zz}E_{0z} \end{pmatrix} \tag{4.5}$$

there will be Raman scattering with z polarized scattered light. Similarly, incident light polarized in the x or y directions will also produce Raman scattering

For modes with xy polarizability components, only certain incident light polarizations will produce Raman scattering. For example for incident light polarized in the xy direction,

$$\mathbf{E}_S \propto \begin{vmatrix} 0 & \alpha'_{xy} & 0 \\ \alpha'_{yx} & 0 & 0 \\ 0 & 0 & 0 \end{vmatrix} \begin{pmatrix} E_{0x} \\ E_{0y} \\ 0 \end{pmatrix} = \begin{pmatrix} \alpha'_{xy}E_{0y} \\ \alpha'_{yx}E_{0x} \\ 0 \end{pmatrix} \tag{4.6}$$

there will be xy polarized Raman scattering. Exciting light polarized in the x or y directions will also result in Raman scattering but the scattered light will be polarized in a different direction. That can be a disadvantage in SERS. In order to achieve the E^4 enhancement both the incident and scattered light must be enhanced by SERS mechanisms. Both the incident and scattered light must be polarized in the same direction as the electric field surrounding the nanoparticle[71, 72]. Similarly, modes with yz or xz polarization components will have Raman scattering when their incident radiation is polarized in the yz or xz directions respectively.

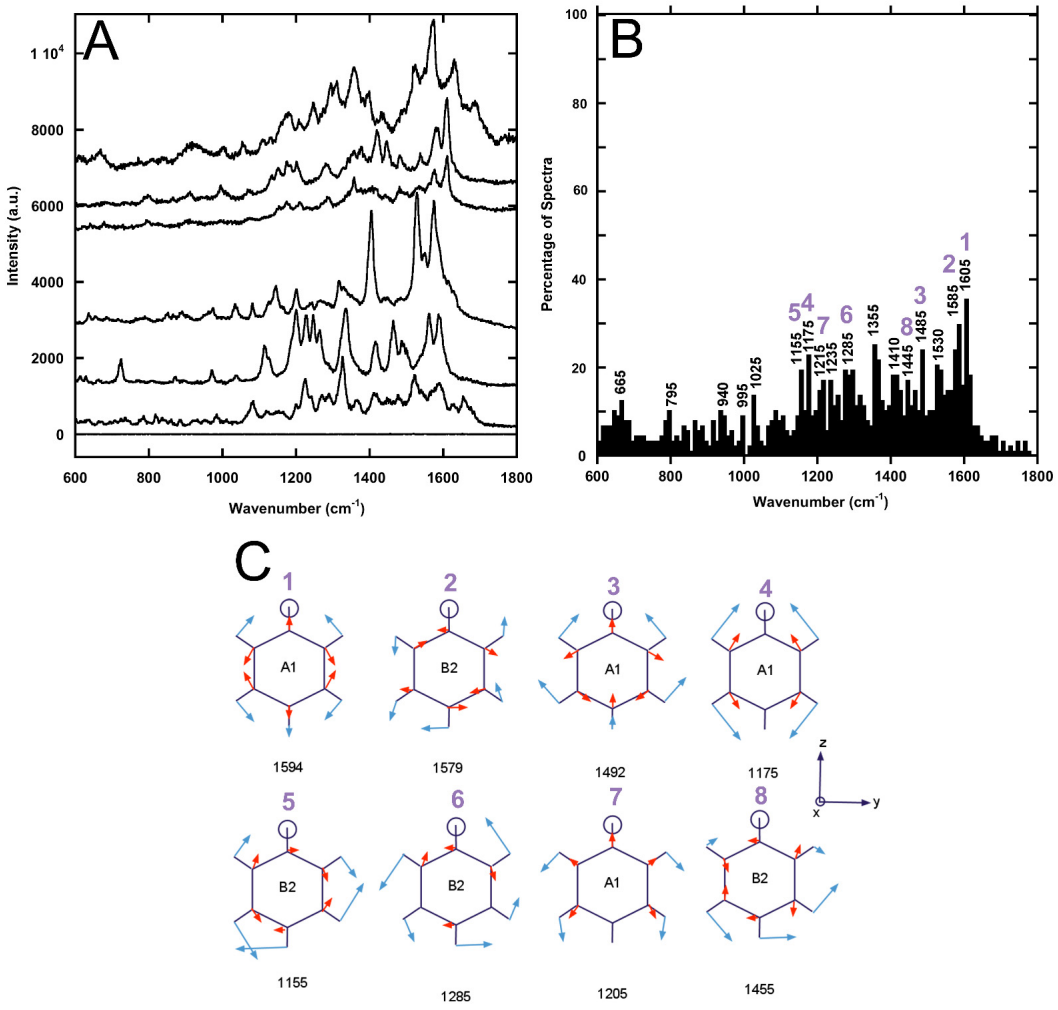

Figure 4.10: Silver surface enhanced Raman spectra of collagen I fibrils. A) Raman spectra single collagen I fibrils with Ag nanoparticles attached and a spectrum of a fibril without nanoparticles (bottom spectra). The Raman scattering signal was enhanced by a factor of 10^4 (Equation 3.1 p26). B) Histogram of peak positions observed in 87 silver SERS spectra of collagen I fibrils. C) Diagrams of the 8 phenyl vibrational modes commonly observed.

4.2.2 Silver SERS Spectra

As a first step to obtain surface enhanced Raman spectra, silver nanoparticles were attached to collagen I fibrils in water. 34 nm and 45 nm nanoparticles were used. Fibrils with well-attached nanoparticles were used for SERS experiments. Typically, the SER spectra of a collagen I fibrils had many intense bands in the 1000 to 1800 cm^{-1} region (Figure 4.10A). A histogram of peak positions observed in the 600 to 1800 cm^{-1}

region (Figure 4.10B) revealed two common bands. These peaks, located around 1585 and 1605 cm^{-1}, can be attributed to ring vibrations [70, 68, 73, 74] of either phenylalanine or tyrosine residues and were each observed in roughly 30% of all SER spectra (Table 4.2 p46). Even so most of the PBS, in which the fibrils were assembled, was washed prior to the SERS experiments, we did observe a possible weak contribution of PBS with peaks around 936 and 1022 cm^{-1}. Interestingly the fingerprint modes of phenylalanine and tyrosine residues at 1000 and 828 cm^{-1} [2], respectively, were not observed in any spectrum. Using uncoated regions of the fibrils as a reference, the polydisperse Ag nanoparticles were found to enhance the Raman scattering signal by a factor of 10^4.

The eight most commonly observed phenyl modes are much different from the strongest Phe-Phe nanotube modes (Figure 4.10C). Only half of the strongest Phe-Phe modes were the most common modes in the silver SERS. Most notably, three of the four strongest modes found in the far field, 1000, 1024 and 618 cm^{-1} (Figure 4.9), were not commonly observed in the silver SER spectra. The 1585 cm^{-1} peak also became the second most commonly observed peak and the number of B_2 modes (xy polarizability components) in the top eight doubled.

4.2.3 Gold SERS Spectra

As an attempt to observe the fingerprint modes of phenylalanine and tyrosine residues, 65 nm gold nanoparticles were also attached to collagen I fibrils in water. The Au nanoparticles preferentially attached to the collagen fibrils over the glass. The particles often attached to the fibrils in registry with the 67 nm banding pattern (Figure 4.4B p31). The gold SER spectra of collagen I fibrils had many peaks in the 1000 to 1800 cm^{-1} region with a distinctive 1000 cm^{-1} phenylalanine peak in nearly every spectrum (Figure 4.11A). The 828 cm^{-1} tyrosine peak was much less common but still apparent. A histogram of peak positions observed between 600 and 1800 cm^{-1} revealed 4 more very common peaks around 1025, 1165, 1195 and 1585 cm^{-1} that each appeared in over 40% of all spectra (Figure 4.11B). These peaks can all be attributed to phenylalanine [9, 68, 2, 70, 75, 57, 74] (Table 4.2 p46). The 1025 cm^{-1} may also arise from PO_4^{3-} attached to the fibrils. Using uncoated fibrils as a reference the Au nanoparticles were found to increase the Raman scattering signal by a factor of 10^5,

which is higher than the silver SER spectra.

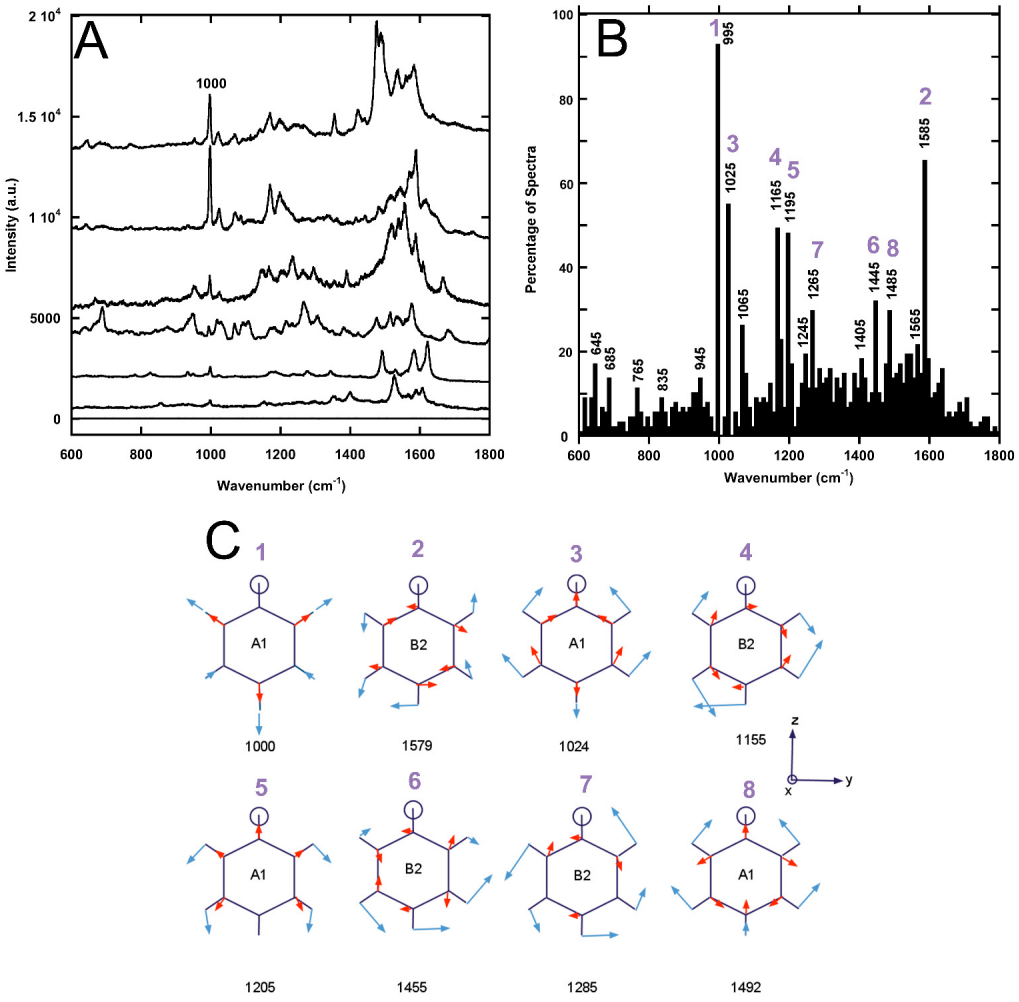

Figure 4.11: Gold surface enhanced Raman spectra of collagen I fibrils. A) Raman spectra single collagen I fibrils with Au nanoparticles attached and a spectrum of a fibril without nanoparticles (bottom). The Raman scattering signal was enhanced by a factor of 10^5 (Equation 3.1 p26). B) Histogram of peak positions observed in 87 gold SERS spectra of collagen I fibrils. C) Diagrams of the 8 phenyl vibrational modes commonly observed.

The gold spectra resembled the Phe-Phe spectra more than the silver spectra in that the 1000 and 1024 cm^{-1} were commonly observed. Many of the gold spectra displayed a large number of phenyl peaks with different relative intensities than observed in the Phe-Phe spectrum (Figure 4.12). Much like the silver SERS the 1579 cm^{-1} peak was commonly observed as well as other B_2 modes (Figure 4.11C).

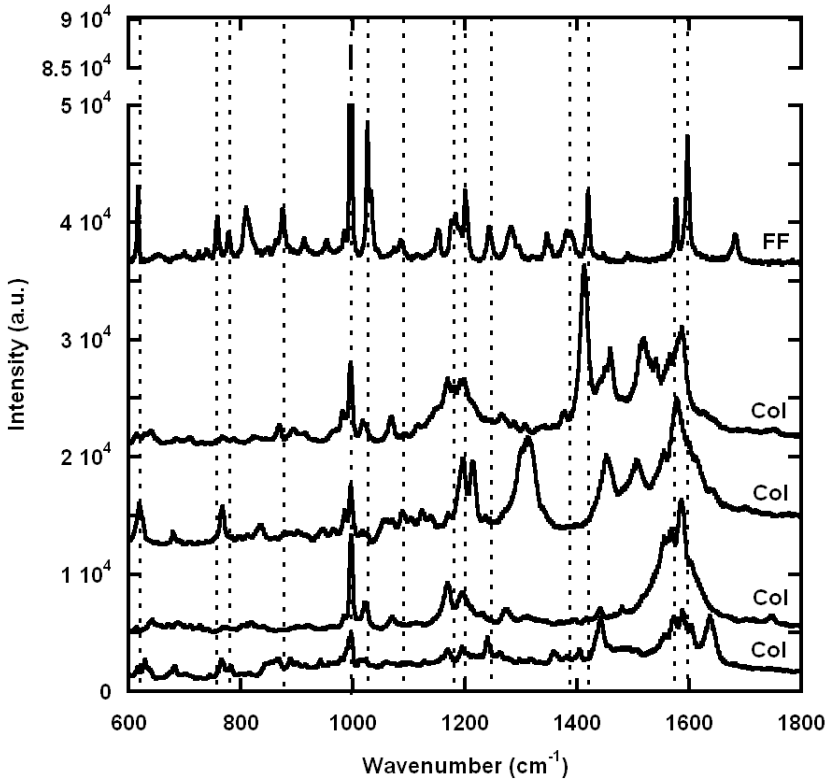

Figure 4.12: A comparison of Gold SERS spectra and the spectrum of Phe-Phe nanotubes. FF: Spectrum of a large clump of Phe-Phe tubes. Col: Gold SERS spectra that resemble the Phe-Phe spectrum. Positions of Phe peaks seen in the gold SERS spectra are marked with dotted lines.

4.2.4 Sum of SER Spectra

When examining a SERS spectrum, only the vibrational modes of the molecules close to the nanoparticle surface are being observed. For this reason there is a large variation between SER spectra. A histogram of all SER spectra can be made, or all the spectra may be summed together. The advantage of a sum is that it can be compared directly with a far-field spectrum. All silver SER spectra were added together to create a spectral sum (Figure 4.13A). The same was done for the gold SER spectra (Figure 4.13B). Neither of the silver or gold SERS spectra closely resemble the far field Raman spectrum (Figure 4.8 p36). The spectral sums, especially the gold sum, had many distinct peaks characteristic of aromatic amino acid residues (Table 4.2 p46). Most notably the silver SER spectra sum displayed the 1000 and 1020 cm^{-1} phenyl peaks absent in the histogram. This suggests that there were weak

contributions from these modes in many of the spectra that were elevated above the noise level. The spectral sums also differed from far-field Raman spectra by not exhibiting strong amide bands.

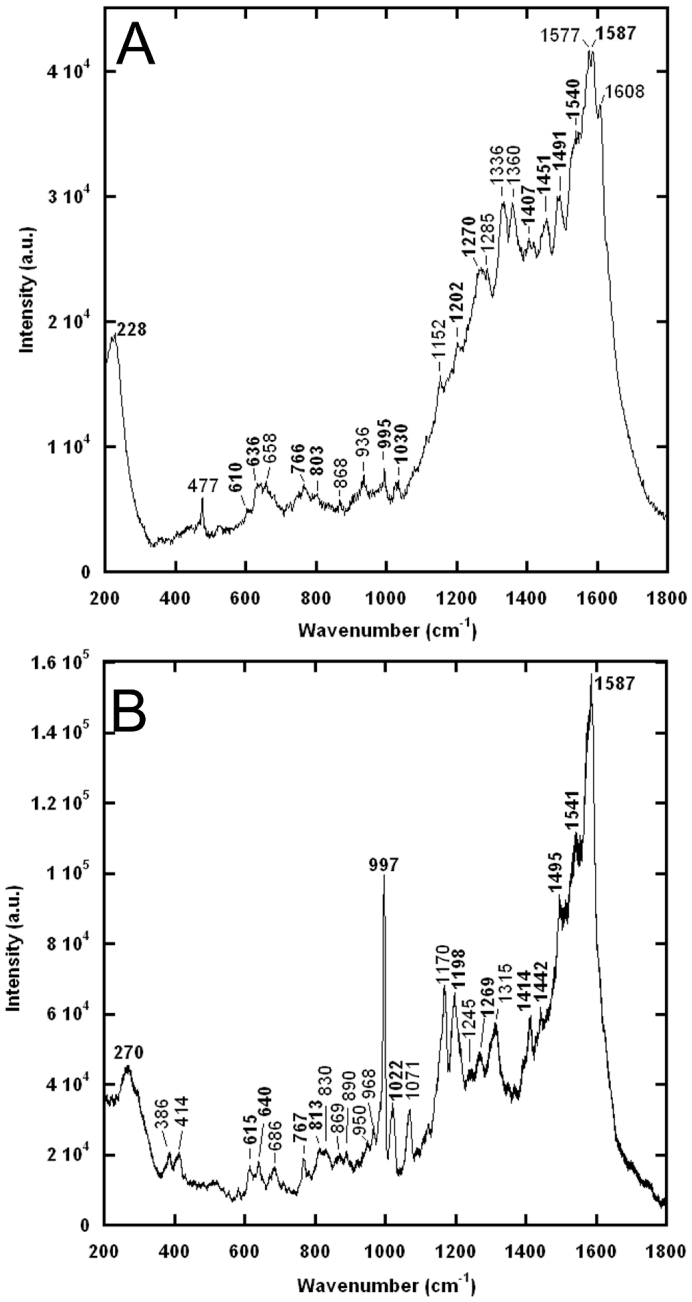

Figure 4.13: The spectral sums of the silver and gold SERS experiments. A) The sum of 87 silver SER spectra. B) The sum of 87 gold SER spectra. Peak positions are labelled and the peaks in common are presented in bold.

Peak Position (cm^{-1})						Assignment		
Far Field		Collagen SERS						
Collagen	Phe-Phe	Ag hist.	Au hist.	Ag sum	Au sum	Phe ring	Tyr ring	Other
	617			610	615	6b B_2 618(12)		
				636	640		6b B_{3g} 630(20)	
		665	645	658			6b B_{3g} 630(20)	
			685		686	4 B_1 690(10)	4 B_{2g} 700(35)	
	758,		765	766	767	A_1 755(25)		
	779							
	811	795		803	813		B_{1g} 820(30)	C-C backbone (821[66], 810[67])
			835		830	10a A_2 835(25)	B_{1g} 820(30)	
				868	869		A_g 820(50)	C-C residues (856[66])
	875							
	914				890	17b B_1 910(30)		
				936		17b B_1 910(30)		C-C backbone (934[67]), PO_4^{3+}
	953	940	945		950	17a A_2 960(20)		
	982				968	B_1 985(15)		
1002	997		**995**	995	997	12 A_1 1000(10)		

Table 4.2: Peaks observed in the 600-1000 cm^{-1} range. Peaks in the far field Raman spectrum of collagen and Phe-Phe nanotubes as well as the silver and gold SER spectra histograms and spectral sums of collagen fibrils are displayed. For the SERS histograms, the 8 most common peak positions are in bold. The ring vibrations are displayed with their Wilson vibration number, symmetry species and the range is excepted position [70]. Only Raman-active tyrosine modes are included. Assignment is based on previous Raman studies of collagen [66, 67] and Phe-Phe [76], the vibrational modes of substituted benzenes [70, 68, 74] and SERS and TERS studies of amino acids and short peptides [73, 9, 75, 57], insulin [10] and phenyl containing molecules [77, 78].

Peak Position (cm^{-1})						Assignment		
Far Field		Collagen SERS						
Collagen	Phe-Phe	Ag hist.	Au hist.	Ag sum	Au sum	Phe ring	Tyr ring	Other
	1028	1025	**1025**	1030	1022	18a A_1 1023(6)		PO_4^{3+}
	1085		1065		1071	18b B_2 1074(8)		CN (1087[66])
	1152	**1155**	**1165**	1152		15 B_2 1156(5)	9a A_g 1166(24)	
	1182	**1175**			1170	9a A_1 1175(5)	9a A_g 1166(24)	
	1202	**1215**	**1195**	1202	1198	A_1 1205	A_g 1210(10)	
1246	1244	1235	1245		1245			Amide III (1248[66], 1251[67])
1289	1283	**1285**	**1265**	1270, 1285	1269	3 B_2 1285(10)	3 B_{3g} 1286(26)	Amide III (1271[66], 1269[67])
				1336	1315	14 B_2 1325(12)		CH(1314 [66], 1307[67])
	1347	1355		1360				CH(1343 [66], 1340[67])
	1385							CH (1391[67])
	1420	1410	1405	1407	1414			COO^- (1422[66])
1445, 1449		**1445**	**1445**	1451	1442	19b B_2 1455(15)		CH (1451,1464[66])
		1485	**1485**	1491	1495	19a A_1 1492(22)		
		1530		1540	1541			Amide II (1526-1576[10])
			1565			8b B_2 1579(18)	8b B_{3g} 1578(26)	Amide II (1564[67])
	1577	**1585**	**1585**	1577, 1587	1587	8b B_2 1579(18), 8a A_1 1594(20)	8b B_{3g} 1578(26), 8a A_g 1600(29)	
	1597	**1605**		1608		8a A_1 1594(20)	8a A_g 1600(29)	

Table 4.3: Peaks observed in the 1000-1610 cm^{-1} range (a continuation of Table 4.2)

4.2.5 Relative Intensities of Ring Vibrations

A great deal of information can be extracted from the intensities of Raman peaks. Fortunately the $1000\,\mathrm{cm}^{-1}$ peak was observed in most of the gold SERS spectra as well as the SERS sums and the Phe-Phe Raman spectrum. The $1000\,\mathrm{cm}^{-1}$ peak can be used as a reference peak to compare phenyl mode intensities [78]. It is the characteristic mode of phenylalanine and does not have interfering contributions from tyrosine ring modes. It is also an A_1 mode with polarizability components in the xx, yy and zz directions, meaning that it will be excited in any orientation. The relative intensities of phenyl ring modes can be used to determine the orientation of the ring with respect to a SERS surface [78, 77].

Position (cm^{-1})	Phe-Phe reference	Au SERS average	Au SERS sum	Ag SERS sum	vibration	polarizability
610-617	0.13		0.09	0.53	6b B_2	yz
685-686		0.32	0.07		4 B_1	xz
758-767	0.07	0.24	0.08	1.03	A_1	xx, yy, zz
890-914	0.02		0.08		17b B_1	xz
945-953	0.03	0.43	0.10		17a A_2	xy
968-982	0.05			0.15	B_1	xz
995-997	1	1	1	1	12 A_1	xx, yy, zz
1022-1030	0.17	0.28	0.22	0.58	18a A_1	xx, yy, zz
1065-1085	0.02	0.29	0.17		18b B_2	yz
1152-1165	0.05	0.68		1.79	15 B_2	yz
1170-1182	0.08		0.45		9a A_1	xx, yy, zz
1995-1202	0.11	0.46	0.40	1.24	A_1	xx, yy, zz
1269-1285	0.05	1.06	0.22	1.82	3 B_2	yz
1315-1336			0.27	3.30	14 B_2	yz
1442-1445		0.43	0.37	1.76	19b B_2	yz
1485-1495		0.80	0.80	2.90	19a A_1	xx, yy, zz
1577-1587	0.1	2.09	1.72	11.47	8b B_2	yz
1597-1608	0.19			12.01	8a A_1	xx, yy, zz

Table 4.4: Relative intensity of peaks assigned to phenyl ring modes. The intensity of the peaks relative to the $1000\,\mathrm{cm}^{-1}$ peak is displayed. The $830\,\mathrm{cm}^{-1}$ phenyl vibration is not included because it is more likely to be assigned to the characteristic tyrosine ring vibration.

The peak heights were measured relative to the $1000\,\mathrm{cm}^{-1}$ peak in the Phe-Phe spectra and the SERS spectral sums (Table 4.4). Many of the modes had much higher SERS relative intensities than their far field Raman counterparts. Most notably the

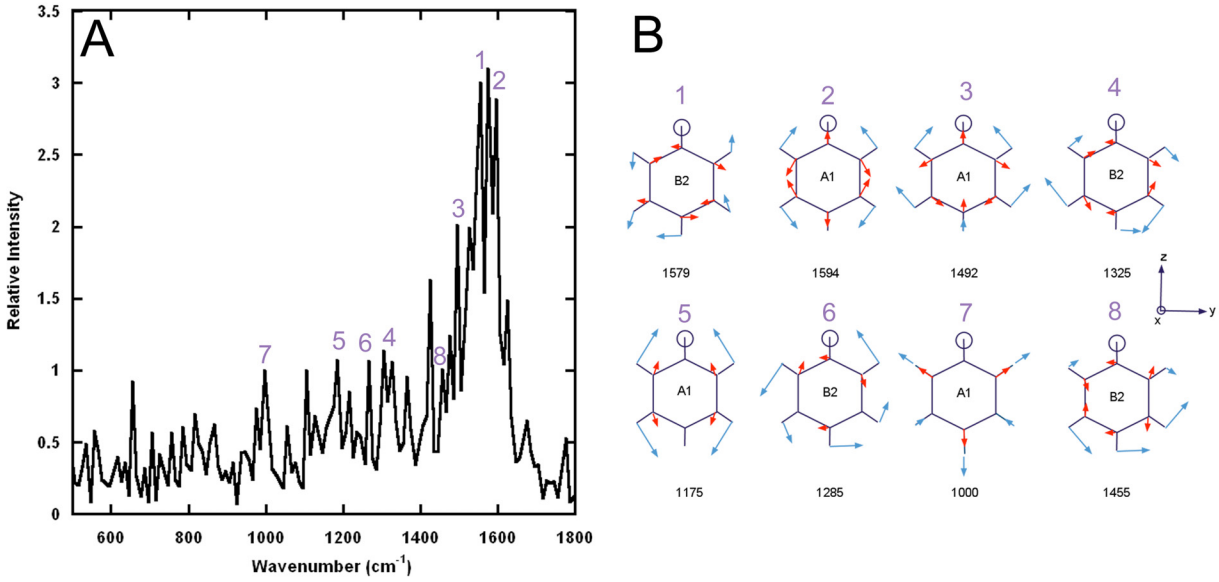

Figure 4.14: The relative intensity of the gold SERS peaks. A) The average relative intensity of the peaks in each 10 cm^{-1} wide bin presented in the gold SERS histogram (Figure 4.11B). The intensity of peaks in spectra containing a 1000 cm^{-1} were measured relative to the 1000 cm^{-1} peak intensity. The average relative intensity was then calculated for each bin in the gold SERS histogram. B) Diagrams of the 8 strongest Phenyl vibrational modes observed.

silvers SERS spectral sum had modes that were up to 12 times as intense as the 1000 cm^{-1} mode.

For each gold SERS spectra, the average relative intensity of each peak was calculated (Figure 4.14A). The peaks were most intense in the region around 1550 cm^{-1}. When examining these peak intensities in combination with the SERS sum relative intensities, it is apparent that the B_2 modes are stronger in the SERS spectra than in the Phe-Phe reference spectrum (Table 4.4).

4.2.6 Amide I Band

Several spectra of collagen I fibrils obtained with SERS presented Amide I peaks. We observed narrow peaks that were similar in position to the 1655 cm^{-1} reference Amide I band. These bands were observed in individual SER spectra and not the spectral sum. The Amide I band in the spectra sum was buried in the shoulder of the residue peaks around 1600. The reference Amide I band from the collagen

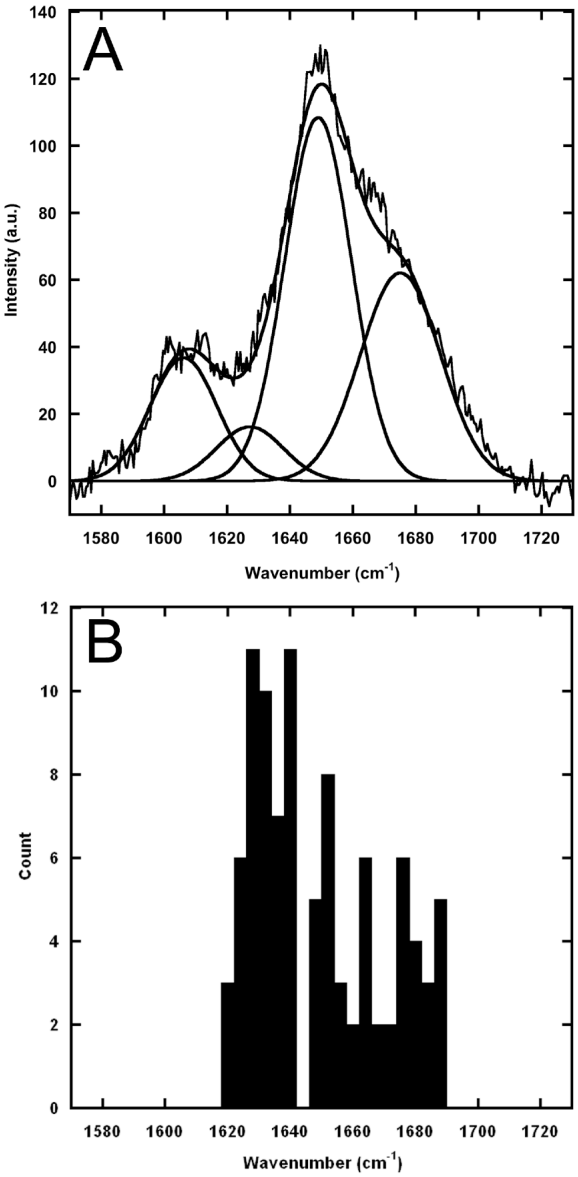

Figure 4.15: Comparison of the diffraction limited and surface enhanced Raman Amide I peaks for collagen I fibrils. A) Peak fitting of the Amide I band observed in a sheet of collagen presented in Figure 4.8 p36. The positions, height and FWHM of the Gaussians are presented in Table 4.5 p58. B) Histogram of the Amide I peak positions observed in SERS. The average FWHM of the Amide I band in 42 silver SERS and 37 gold SERS spectra used were $27\pm12\,\mathrm{cm}^{-1}$ and $22\pm11\,\mathrm{cm}^{-1}$ respectively. Peak positions are presented in Table 4.5.

sheet was fit with a convolution of narrower Gaussian functions with a FWHM of 25 or 30 cm^{-1} (Figure 4.15A, Table 4.5 p58). The Gaussian fitting function positions were comparable to a histogram of Amide I peak positions found in SERS (Figure 4.15B, Table 4.5 p58). The mean width of the SERS Amide I peaks were 27±12 and 22±11 cm^{-1} for silver and gold respectively. The SERS peaks were also more similar in width to the Gaussian fitting functions than the 90 cm^{-1} wide Raman Amide I band itself.

4.3 Discussion

4.3.1 Differences between SERS and Far Field Raman Techniques

In the diffraction limited Raman spectrum of collagen fibrils (Figure 4.8 p36), only contributions from C-H, N-H, Amide I and III bands were visible in both spectra. A 1000 cm^{-1} phenyl ring vibration, commonly observed in published collagen spectra [67, 66], was visible in our spectrum of collagen fibrils arranged in microns thick sheets. In SERS, we observed peaks not seen in diffraction limited Raman. SERS is sensitive to the surface of the fibril. SERS also has sensing volume within a few nanometers of the nanoparticle's surface [12]. Collagen molecules have a diameter between 1 and 2 nm [21]. Hence, our SERS experiments only probed bonds in the first layer of collagen molecules on the surface of the fibril. Due to its surface sensitivity, SERS could also be used to characterize the surface of naturally occurring collagen fibrils. For example, it should be possible to detect post-translational modifications such as glycosylation and hydroxylation on the fibrils surface. We could also use this approach to detect the presence of uncleaved propeptides at the surface of the fibrils using their high disulfide content.

4.3.2 Observation of Ring Modes

The commonly observed peaks in the SERS spectra included ring vibrations, Amide bands and C-H and COO^- vibrations (Table 4.2 p46). When considering the amino acids present in the collagen molecule (Figure 4.16), this is not surprising. The CH vibrations were frequent due to the plethora of CH bonds present in the collagen chain and amino acid residues. The COO^- vibrations arise from the ionized carboxyl

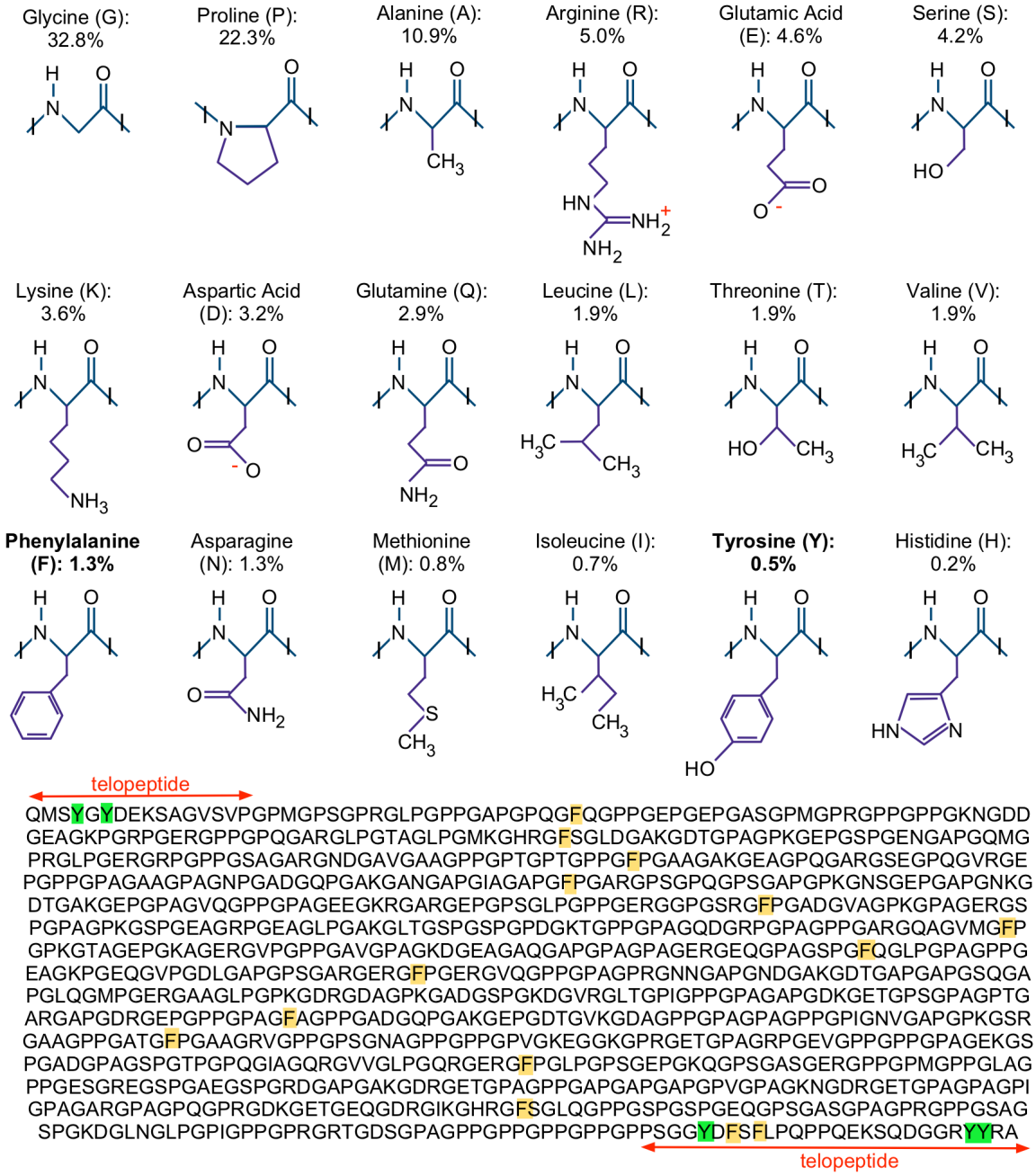

Figure 4.16: The amino acids present in a rat tail collagen I molecule after cleavage of the propeptides. All amino acids contained in the sequence are shown along with the percentage of the molecule that they comprise. The sequence of one of the chains is shown with the phenylalanines and tyrosines highlighted (colour available in electronic version). The telopeptide parts of the chain are indicated. Note that tyrosine is only present in the telopeptides.

groups in the residues of aspartic and glutamic acid [73] which account for 7.8% of the collagen peptide chain (Figure 4.16). But most importantly, amino acids with aromatic side groups give rise to strong Raman bands. It has been observed that the SER spectra of di- and tri-peptides are dominated by Amide bands and aromatic side chain vibrations [73]. Although collagen is mostly composed of glycine, proline and alanine, the helical sequence contains the aromatic amino acids phenylalanine and tyrosine (Figure 4.16).

Although present in small amounts it is reasonable to focus on phenylalanine and tyrosine when assigning peaks. Although glycine, proline and alanine are the three most common amino acids, they have relatively weak spectra with non-unique features. In the SERS spectra of these individual amino acids presented by Stewart et al. [9], the strongest bands in each amino acid was the COO^-deformation at $720\,cm^{-1}$ followed by the symmetric COO^- stretch at $1410\,cm^{-1}$. The only real way to distinguish between amino acids is with modes unique to the amino acids residue. The proline residue also does not produce any strong unique peaks that would make assignment possible [9]. The residues for glycine and alanine are H and CH_3 respectively and do not have distinguishable spectra. Amino acids with C-S bonds are also known to have intense Raman spectra. The methionine residue (in 0.8% of the chain) exhibits a distinguishable C-S peak at $700\,cm^{-1}$ [9]. In the gold SERS experiments there was a common peak around $685\,cm^{-1}$. It is possible that this peak could have arisen from the C-S vibration however; it is also possible that it is from the phenyl ring vibration at $690\pm10\,cm^{-1}$ or a tyrosine vibration at $700\pm35\,cm^{-1}$. There is not another strong C-S peak present to justify the assignment of this peak to the methionine residue.

The strongest phenylalanine and tyrosine bands were observed around 1585 and $1605\,cm^{-1}$. It is possible that other residues could produce bands in this region. That is true with all vibrational spectroscopy of organic materials. However, it is very likely that these bands do arise from phenylalanine and tyrosine. In the SER spectra of non-aromatic amino acids examined by Stewart et al., no bands in that region were observed [9]. COO^- asymmetric stretch and a NH_2 scissors vibrations appear in this region in IR. These modes exhibit weak or no Raman scattering. Due to the high electric field intensities used in SERS it would be possible to observe these

modes. However, the phenylalanine and tyrosine modes do exhibit Raman scattering and would be more likely than the Raman-inactive vibrations. It is thus reasonable to assign these bands to the phenylalanine and tyrosine rings as opposed to other organic groups.

As mentioned previously, the modes of ring vibrations are categorized into symmetry species that have different polarizability components (Table A.1). All Raman active modes can be observed in a randomly oriented sample when using a far field technique. SERS differs from far field Raman in that a mode is strongly enhanced if its polarizability component is perpendicular to the metals surface. This was evident in the calculation of the electric field of a single dielectric sphere (Equation 2.7). In the area with the strongest enhancement, the electric field was normal to the metal's surface. This is also the case with other plasmon supporting structures such as coupled nanoparticles or nanoparticles with sharp features. It has been found computationally that in these cases, in the region with the largest enhancements the normal component of the field is also much larger than the tangential component [79, 60]. It is commonly assumed that the enhanced spectra collected from clusters of nanoparticles [63, 77, 76] and rough metallic surfaces [9, 78] are dominated by modes excited perpendicular to the metals surface.

For this reason, the orientation of the rings with respect to the metal surface greatly affects the observed spectra. The phenylalanine and tyrosine residues each have a group of modes, A_1 and A_g [70] respectively, that have polarizability components in the xx, yy and zz directions [53]. These modes should be enhanced no matter what orientation the ring is in. The 1000 and 1605 cm^{-1} modes are of this kind, the first one for phenylalanine only and the second one for phenylalanine and tyrosine (Table 4.2 p46).

The other symmetry species will only be enhanced in particular orientations. The average intensity of the phenyl modes in each of these symmetry species were calculated and divided by the average intensity of the phenyl modes in the A_1 species (Figure 4.17). While many of the phenyl vibrations overlap with vibrations from the tyrosine modes they are still effective at determining ring orientation. The peaks observed are likely to have a much greater contribution from phenylalanine than tyrosine. Phenylalanine is more than twice as common as tyrosine in the collagen

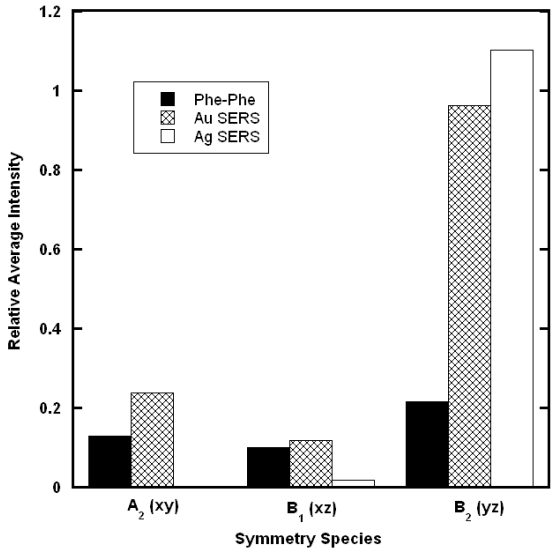

Figure 4.17: The average intensity of the phenyl modes of each symmetry species relative to the average intensity of the A_1 modes. The average intensity of the modes of each symmetry species were taken for the Phe-Phe Raman spectrum and the gold and silver SERS spectral sums. For each Raman technique, the average intensity was divided by the A_1 intensity average.

chain.

The B_1 symmetry species would be ideally enhanced if the face of the ring was tilted towards the metals surface due to its xz polarizability component. Three modes of this kind were observed in our experiments. Two of these modes were weakly observed in the gold SERS experiments and the Phe-Phe reference spectrum. One of these modes was weakly observed in the silver SERS. There was no evidence of a strong preferential enhancement of this mode (Figure 4.17).

The B_2 symmetry species would be optimally enhanced if the edge of the ring was tilted towards the surface due to its yz polarizability component. Modes of this kind demonstrated strong enhancements with SERS techniques. Specifically, the $1580\,\mathrm{cm}^{-1}$ had enhancements of 17 and 115 times stronger than the $1000\,\mathrm{cm}^{-1}$ peak in gold and silver SERS experiments. The intensities of these B_2 modes suggest that there is preferential enhancement of these modes (Figure 4.17).

The A_2 symmetry species would be greatly enhanced if the face of the ring was

tilted towards the metal surface as well as the edge due to its xy polarizability component. There was only one phenyl A_2 mode observed in these experiments at 950 cm^{-1}. It was only observed in the gold SERS and the Phe-Phe reference spectrum. There was no evidence of preferential enhancement (Figure 4.17). The 828 cm^{-1} band characteristic of tyrosine is a B_{1g} mode and has a xy polarizability component. It was observed in the gold SERS experiments but not in the silver ones. However without an appropriate far field reference sample of tyrosine, it cannot be used to determine orientation.

In the gold SERS experiments, the symmetric 1000 cm^{-1} peak was visible in almost every spectrum but was also regularly of a lower intensity than the other peaks (Figures 4.13 and 4.11). This has also been observed in previous gold SERS experiments with phenyl containing samples [77, 78]. Since the 1000 cm^{-1} peak arises from an A_1 mode, it will always be visible no matter what orientation the phenyl ring is in. The other groups of modes will only be visible in specific orientations. In far field Raman, where the sample is randomly oriented and there are many rings probed, this will result in an intense 1000 cm^{-1} peak (Figure 4.9). However if there are a few rings probed that are in an orientation favourable to one of the other groups, the modes of these groups will be observed at a greater intensity. With the strength of the B_2 modes compared to the A_1 modes, it is probable that on average the rings are positioned with respect to the metal's surface in a tilted configuration as shown in Figure 4.18.

Interestingly, the 1000 cm^{-1} peak was only very weakly observed in the silver experiments (Figure 4.13). An absence of this peak was observed in a previous silver TERS experiment [57]. In addition to orientation, the number of rings close to the surface will also affect the observed spectra. Each collagen triple strand is 300 nm long and 1-2 nm in diameter. It contains 3168 amino acids, 42 of which are phenylalanine and 15 of which are tyrosine. The Raman intensity of a mode decays from the surface. To be conservative, we assume that only the top half of the triple strand is enhanced enough to be detected. That places a phenylalanine every 14 nm along the strand and a tyrosine every 40 nm. The diameters of probes used in these experiments were 34 and 45 nm for silver SERS and 65 nm for gold SERS. With the larger probes used in the gold experiments, it is likely that more rings were in contact with the surface.

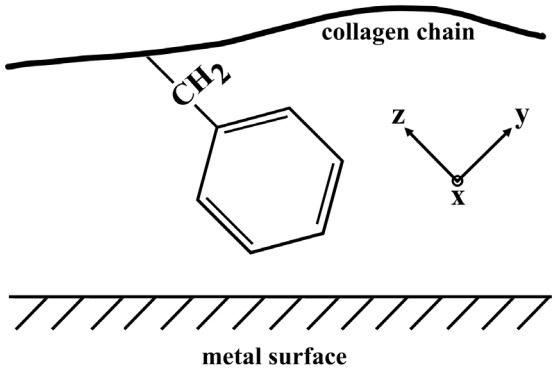

Figure 4.18: The proposed orientation of the phenylalanine residue with respect to the metal surface. The coordinate system of the phenyl molecule is shown. The x axis is out of plane.

Since the 1000 cm^{-1} peaks observed in gold SERS were often weak, it is likely that there were not enough rings in contact with the silver nanoparticles for the 1000 cm^{-1} peak to be easily observable. For this reason the 1000 cm^{-1} peak was not observable in the histogram of SERS spectra but was still observable in the sum. The summation of multiple spectra allowed the peak to rise above the noise level. This weakening would also be exaggerated if the rings had a higher affinity with gold than silver.

The characteristic tyrosine ring around 830 cm^{-1} was also only observed in the gold SER spectra (Table 4.2). Tyrosine residues are only present in the telopeptides of the collagen molecule. They should occupy the edges of the D-period (Figure 2.1 p5). In the AFM images of the gold nanoparticle covered collagen fibrils (Figure 4.4B), the particles often attached to the fibrils in register with the 67 nm banding pattern. The observation of the tyrosine characteristic ring vibration in gold but not silver could be a result of a gold nanoparticles attachment preference. A nanoparticle distribution creating high field enhancements in the telopeptide regions of the fibril would explain the observation of this vibration with gold but not silver.

4.3.3 Amide I Band

The Amide I band arises mainly from the C=O stretching mode of the peptide bond with minor contributions from the C-N stretching and N-H bending modes [70]. Because of this coupling between the C=O and N-H modes, the Amide I band is sensitive

Far Field Raman Deconvolution		SERS histogram	
Position (cm^{-1})	FWHM (cm^{-1})	Position (cm^{-1})	Assignment
1627	25	1628	collagen helix
		1640	
1649	25	1652	α helix
		1664	
1675	30	1676	β sheet

Table 4.5: Amide I band positions. The peak positions and FWHM used in the deconvolution of the far field Raman spectrum of the collagen I Amide I band (Figure 4.15A). The centers of the 5 strongest peaks in the histogram of SERS Amide I peak positions (Figure 4.15B).

to the hydrogen bonding pattern within a polypeptide. In other words changes in position of the Amide I band indicate different secondary structures such as α-helix or β-sheet. Based on sequence analysis of collagen type I chains, the most frequent secondary structure is the collagen-helix which has a characteristic Amide I peak around 1629-1638 cm^{-1} as measured with the Raman spectrum of the collagen-like molecule $(PPG)_{10}$[80] . According to a secondary structure prediction algorithm by Chou and Fasman [81], 18% of the chain should be in the α-helix conformation and 19% of the chain should be in the β-sheet conformation with peaks at 1650 [82] and 1672 cm^{-1} [83] respectively.

Interestingly the far field Raman spectra of collagen I fibrils shows an Amide I band centered at 1655 cm^{-1}, characteristic of an α-helix, with shoulders around 1630 and 1675 cm^{-1} characteristic of the collagen-helix and β-sheets, respectively. Deconvolution using Gaussian peaks yielded peak positions at 1627, 1649 and 1675 cm^{-1} (Figure 4.15A p50). In comparison, SERS spectra showed narrow Amide I bands with widths around 25 cm^{-1} and a wide range of peak positions between 1620 and 1690 cm^{-1} (Figure 4.15B). Furthermore, the distribution of peak positions clusters around 1628, 1640, 1652, 1664 and 1676 cm^{-1} (Figure 4.15B), in good agreement with the far field spectrum deconvolution (Figure 4.15A, Table 4.5). The presence of narrow Amide I bands in the enhanced Raman spectra indicates that we are most likely observing a single type of secondary structure at a given location. This allows us to assign secondary structures without the need of any deconvolution. Our results also confirm the presence of collagen-helix, α-helix and β-sheet structures at the surface of the fibril as expected.

4.4 Conclusion

Analysis of the spectra collected with SERS techniques revealed valuable information about the structure of collagen. The phenyl ring was found to be in an orientation with the edge of the ring tilted towards the nanoparticles surface. The SERS Amide I bands confirm the presence the characteristic collagen-helix as well as α-helix and β-sheet structures at the surface of the fibril. The dominance of contributions from amino acid residues in the SER spectra demonstrates the techniques ability to probe the fibrils surface molecules.

SERS was found to have large temporal spectral variations due to diffusion of the weakly attached nanoparticles. Although the variation is less prominent in air, it demonstrates that the nanoparticle SERS technique cannot be used in experiments that involve measuring spectra at the same position. This technique also cannot control the nanoparticle position. This can be overcome by using targeting molecules or tip-enhanced Raman spectroscopy.

Chapter 5

Tip Enhanced Raman Spectroscopy

The application of Tip Enhanced Raman Spectroscopy (TERS) has potential to offer routine structural investigations of proteins at the nanoscale. Much like SERS, it can probe a very small area on the surface of a protein. With the positioning power of the AFM, it has the advantage of high spatial resolution. TERS is also a label-free operation. Labels may affect biological structure and, consequently, the interpretation of data. When applied to collagen I fibrils, it has the capabilities to map structural changes on the surface of the fibril with minimal deformations of the sample.

5.1 Tip Preparation and Characterization

With our TERS set-up we rely on surface plasmons to enhance our Raman signal. In order to do this successfully, we must modify the surface of an AFM tip into a SERS active surface. SERS surfaces are created in a variety of ways. Three popular ways are nanoparticles (as investigated in the previous chapter), roughened metallic surfaces and highly ordered structures produced by lithography techniques. Applying these methods to AFM tips results in a Raman active surface that can be scanned over a sample.

The importance of a good-quality tip for TERS cannot be overstated. There are several techniques which generate TERS probes, but the reproducibility and yield of good tips are still a challenge [84]. Until 2006, the yield of metal tips that gave enhancement had been reported to be 20 to 30 %, and often, the enhancements were very small [64]. The reproducibility of the enhancement exhibited by the tips was poor, even with those that looked identical by SEM imaging [64].

The two techniques most frequently used for TERS probe fabrication are electrochemical etching methods of solid metal probes and the metal evaporation deposition on silicon or silicon nitride AFM tips [84]. In this thesis we used metal evaporation deposition as well as nanoparticle attachment. Magnetron sputtering and metal layer

modifications such as annealing and Focused Ion Beam (FIB) techniques were also investigated.

5.1.1 Nanoparticle Covered Tips

In theory, the attachment of SERS nanoparticles to an AFM tip is simple. As long as there is an aggregation of nanoparticles at the apex of the tip, there would be a hot spot that could be scanned across a sample.

The major obstacles with this technique are reproducibility and background spectra. The attachment configuration at the tip apex is determined by a random process. Different attachment mechanisms and protocols can only increase likelihood of an active tip. If the nanoparticles are not well attached they may fall off during scanning, thus reducing the tip optical activity. Much like with vapour deposition tips, many of the tips will be inactive. The background spectra can be a considerable hurdle as well. Although the nanoparticles themselves do not have a strong background, the spectra of any molecules used to attach the nanoparticles will be enhanced.

Mechanisms to attach nanoparticles and microparticles to AFM tips have been investigated for AFM-based surface force experiments [85]. A great deal of these mechanisms use adhesives [85]. Unfortunately, these mechanisms have not been developed for Raman spectroscopy and might be unsuitable for TERS due to particle size, lack of hot spots at the tip apex or unsuitable adhesives with vibrational modes that overlap with the sample's spectrum.

One group has used a nanoparticle covered tip to do TERS experiments [86, 87]. They used a silane coupling method to attach silver nanoparticles. They mentioned that their method had disadvantages. Their tips were noisy because of the signal from the polymer layer that was used to attach the nanoparticles. Unfortunately they did not publish any spectra of their tips not in contact with their samples. We investigated a similar silane attachment method for gold nanoparticles previously developed to produce colloidal AFM probes [88].

As a first attempt to create optically active probes, AFM tips were dipped in a silver nanoparticle water solution. The AFM chip was held between two Teflon squares with a chip sized grove removed from the lower square (Figure 5.1). A pipette tip with a melted end attached to a micro manipulator was used to move a $10\,\mu$l

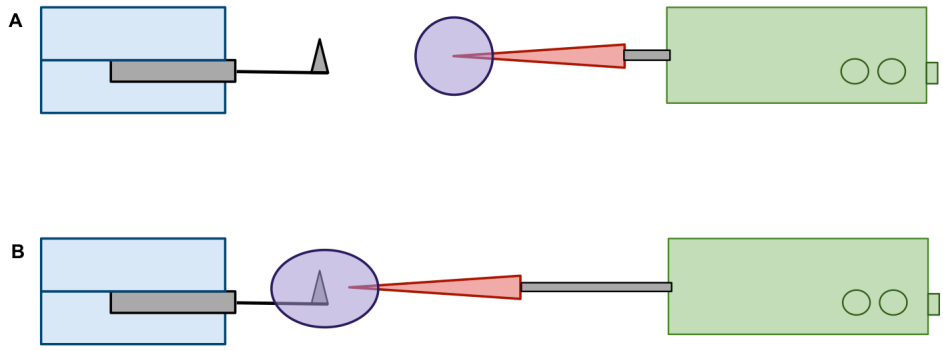

Figure 5.1: The set-up used to coat the AFM tips with nanoparticles. A) Before dipping B) Tip inside the droplet

droplet of the 34 nm silver nanoparticle solution (diluted 100X from nanocomposix solution). This process performed under a microscope with a 10X objective. Once the AFM cantilever was in the droplet it was left for 10 minutes.

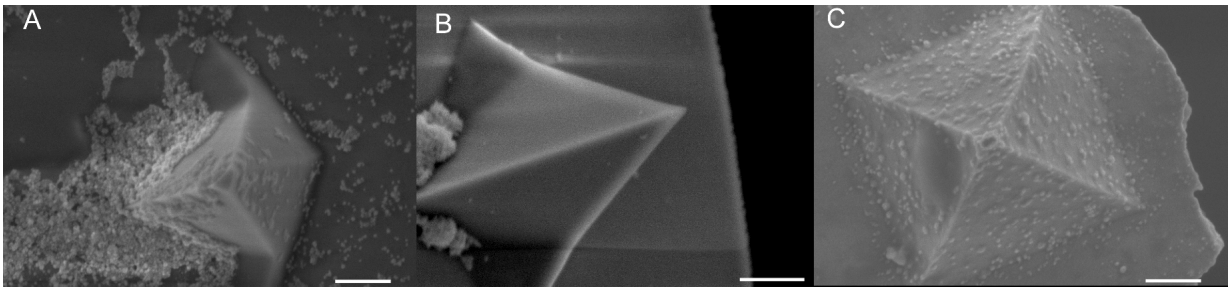

Figure 5.2: SEM images of TERS tips covered with silver nanoparticles. A) MSNL tip covered with 34 nm Ag nanoparticles. This tip was active and used to map a line across a fibril B) Inactive MSNL tip covered with 34 nm Ag nanoparticles C) A MSCT tip coated with PDADMAC followed by 34nm Ag nanoparticles. Scale bars represent 10 μm.

This simple process produced some active TERS tips (Figure 5.2A) and a large amount of inactive tips (Figure 5.2B). It is important to note that both the cantilevers and the tips are not always made of the same material. The MSCT cantilevers and tips are made of silicon nitride The MSNL tips are made of silicon but their cantilevers are made of silicon nitride. No significant difference in the two types of cantilevers was observed when examining tip activity. SEM images revealed that in an inactive tip, the nanoparticles deposited at the tip base leaving a naked apex (Figure 5.2B).

However, the SEM image of a previously active tip, had a nanoparticle island that reached the top of the peak (Figure 5.2A). The main advantage of this technique is that its background should be comparable to the spectra of the nanoparticle itself (Figure 4.5 p33) and have no distinct peaks in the range used to examine collagen. That was confirmed when the spectra of a 34 nm silver nanoparticle covered tip on clean glass was collected (Figure 5.3). The spectra of that tip on a collagen sample had many distinct peaks above the background. However, the low success rate in creating active tips and the tip longevity leave much to improve upon.

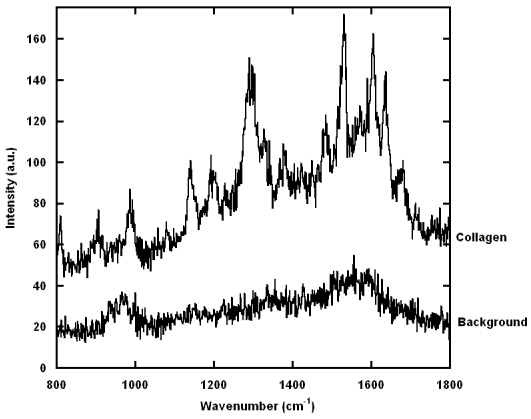

Figure 5.3: The spectra of a tip coated with 34 nm silver nanoparticles (Figure 5.2A) over a collagen fibril and clean glass.

In order to better attach the nanoparticles to the AFM tip, three attachment molecules were investigated. The addition of a PDADMAC (polydiallyl dimethyl ammonium chloride) layer to the tip before being exposed to nanoparticles improved nanoparticle attachment (Figure 5.2C). The PDADMAC was polydisperse with a molecular weight ranging from 100 to 200 kilodaltons. The AFM tip was dipped in a solution of 0.01% PDADMAC, dried and dipped in a solution of silver nanoparticles (Figure 5.4). The SEM image of the tip revealed attachment was much more even with nanoparticles randomly attached to the entire tip surface (Figure 5.2C). There was no longer a favoured attachment to the tip base. PDADMAC is a polyelectrolyte with a positive charge. Polyelectrolytes are often used to make layered nanostructured materials [89]. The positive charge makes it easier for the nanoparticles to attach to the tips. This demonstrates the ability of an attachment molecule to improve the

technique. Unfortunately PDADMAC has organic bonds and the potential for an interfering background.

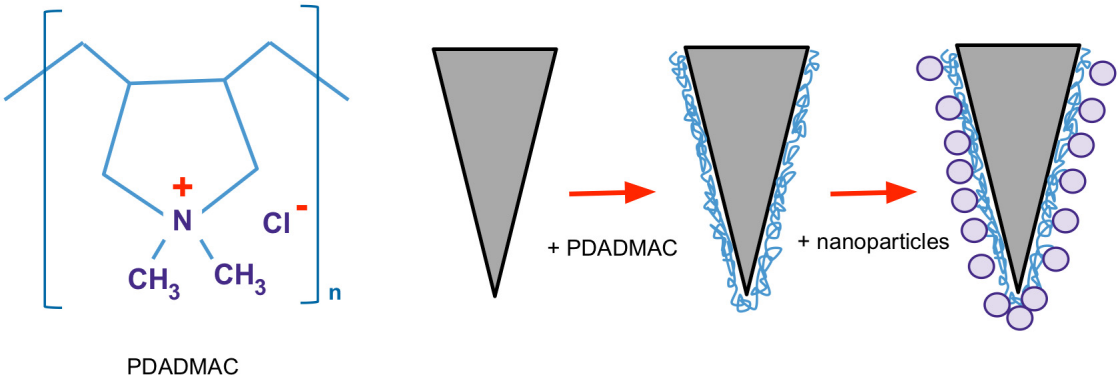

Figure 5.4: A diagram of the PDADMAC molecule and an illustration of the attachment mechanism used to attached 34 nm silver nanoparticles to an AFM tip with PDADMAC.

A simpler attachment ion was used to attach the silver nanoparticles in the place of PDADMAC in the attachment procedure. 1M MgCl was used with no noticeable advantage to the straight nanoparticle attachment method.

A silane attachment molecule previously used to attach gold nanoparticles to AFM tips [88] was also investigated. Tips were dipped in a small beaker of 10 ml propanol, 200 μl 3-MPTS ((3-mercaptopropyl)trimethoxysilane) and 200 μl of water for 20 minutes. It was then washed by dipping the tips in propanol then water beakers (each for 1 minute). It was then left in a 1 μl of 65nm gold nanoparticle water solution with the pipette tip micromanipulator method or in a beaker of the nanoparticle solution diluted 100x and 50x for 2 hours. None of the tips produced with 3-MPTS were active.

As mentioned previously, one of the major considerations with this method is background. The PDADMAC molecule, although an effective attachment molecule, had an interfering spectrum due to its organic bonds (Figure 5.4). The spectra of these tips on glass had very intense and fluctuating peaks (Figure 5.5C). Its background spectra made this method unusable, despite its high tip activity rate. The MgCl tip had a reasonable background making it an acceptable method (Figure 5.5A). However, the method showed no clear advantage over directly attaching the nanoparticles to

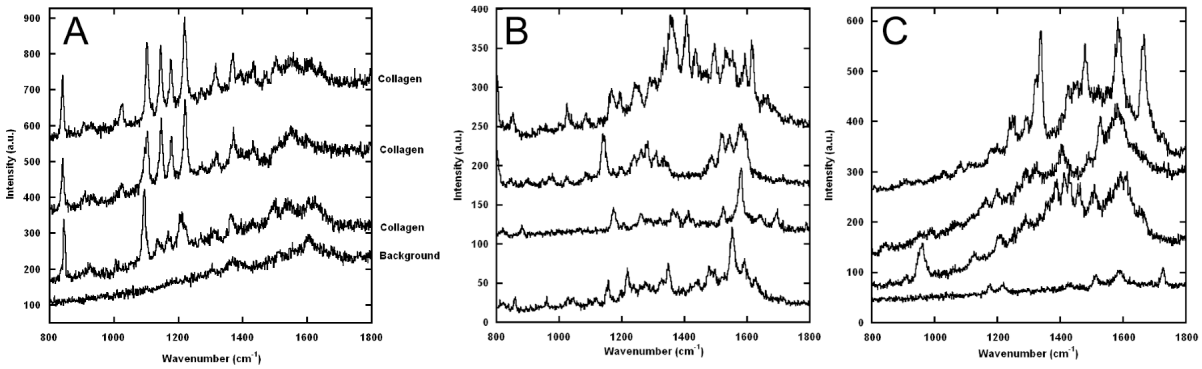

Figure 5.5: Spectra produced by tips with 34 nm silver nanoparticles attached with MgCl and PDADMAC (Figure 5.2C). A) The spectra of a MSCT AFM tip coated with 1M MgCl followed by 34 nm silver nanoparticles. The top 3 spectra were taken with the tip over a collagen fibril in a line scan. The bottom spectrum was taken on clean glass prior to the collagen spectra. B)The spectra of a MSCT afm tip coated with 0.01% PDADMAC followed by 34 nm silver nanoparticles over a collagen fibril. C) The spectra of a MSCT afm tip coated with 0.01% PDADMAC followed by 34 nm silver nanoparticles over clean glass.

an untreated tip.

5.1.2 Vapour Deposition Tips

Vapor deposition is the most common way to metallize AFM tips for use in TERS [64]. The morphology of a silver layer produced by vapor coating is rather rough and uncontrollable [64]. An irregularly shaped nanoparticle supports different surface plasmons of varying wavelengths [64]. The irregularity of a rough vapour coating results in AFM tips that are active at many excitation wavelengths.

Both silver and gold coatings were investigated. The silver coatings used were 30 nm thick. The gold coatings were also 30 nm with a 2 nm adhesion layer of chromium. The coating of the tips was performed by Andy George. The adhesion of a gold coating directly to an AFM tip is fairly weak and the coating may peel after several hours of scanning [64]. For this reason a chromium layer was used. Although the gold coating stayed on and has the distinct advantage over the silver tips of less oxidation, the gold tips were not active.

SEM images of 30 nm silver coatings revealed a grainy surface. The surfaces of previously active silver tips appeared to have grains with variation in size and shape

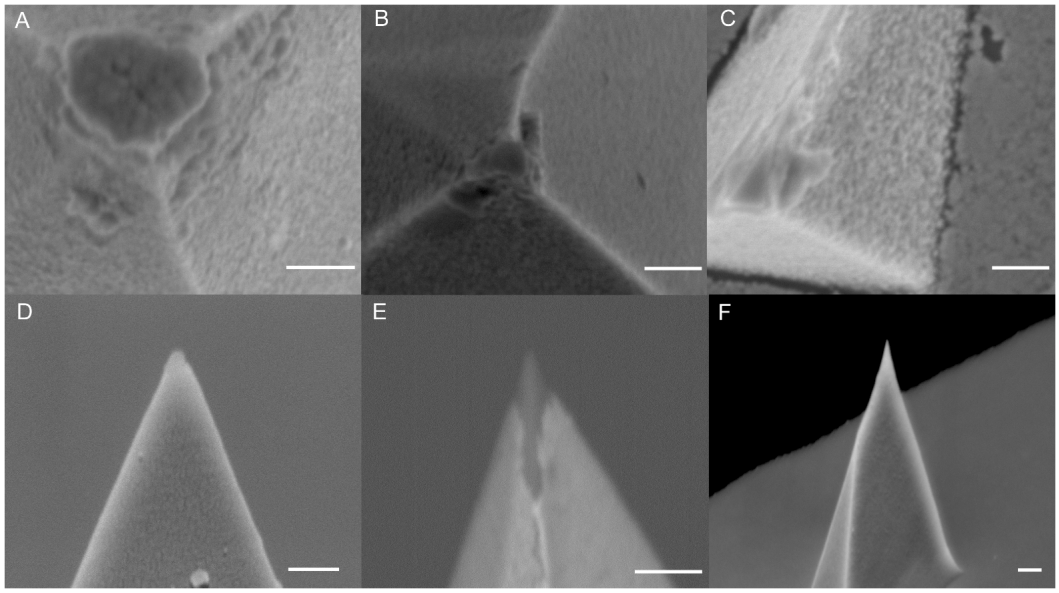

Figure 5.6: SEM images of tips made by vapour deposition. A) Nanoworld CONT tip coated with 30 nm of silver B) TESP tip coated with 30 nm of silver C) Veeco MSNL tip coated with 30 nm of silver. This is one on the five tips on this chip. D) Veeco CONT tip coated with 2 nm of chromium and 30 nm of gold E) Back scattering image of a Veeco CONT tip coated with 2 nm of chromium and 30 nm of gold F) Veeco MSNL tip coated with 2 nm of chromium and 30 nm of gold. The silver coated tips were imaged after they were used to produce TER spectra. Scale bars represent 5 μm.

(Figures 5.6A-C). They had a grainier appearance than the inactive gold coated tips (Figures 5.6D-F). In order to make gold TERS tips, a process that creates a grainier surface would be needed.

The background spectra was examined by taking the spectra of an active tip on clean glass with the same Raman settings used for collagen samples (Figure 5.7). The background had a reasonable spectra with a 520 cm^{-1} silicon peak as well as the silver surface species band.

5.1.3 Tip Decomposition of Vapour Deposition Tips

Due to the low tip activity rate associated with vapour deposition, it is tempting to use the tips up to their breaking point. Eventually the tip will become inactive by a change in the surface structure of the tip or the wearing off of the coating completely.

Theoretically, the grains of the vapour coated TERS tips act in the same fashion

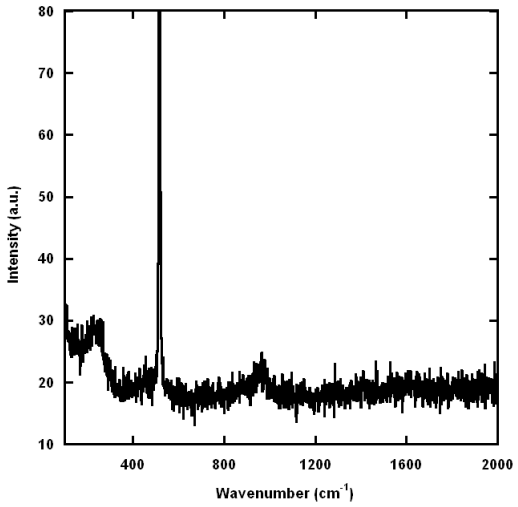

Figure 5.7: Background spectra of a 30 nm of a CONT cantilever (Figure 5.6A) in air on clean glass after use in TERS experiments.

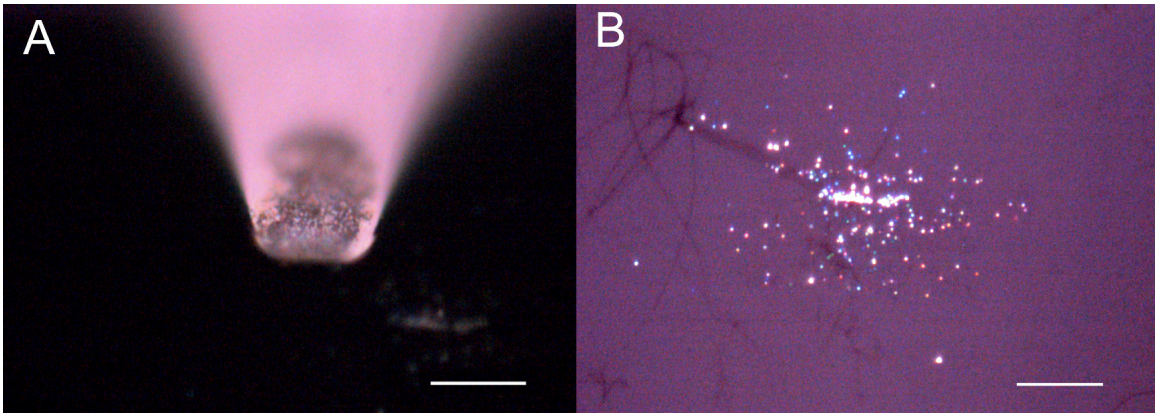

Figure 5.8: DIC images of a decomposed tip. A) DIC image of an MSNL tip coated with 30nm silver after the layer has fallen off. B) The fallen silver particles on a collagen sample on glass in water. Scale bars represent 5 μm.

as the SERS nanoparticles discussed in the previous chapter. During a TERS scan in water, a tip decomposed (Figure 5.8). It is well known that using a tip in water can result in the coating peeling off and is not commonly practised [90]. However, this allowed us to investigate the SERS activity of the tip coating's grains. This tip was on the same chip as other active tips (Figure 5.6C). The activity of these fallen particles (Figure 5.9) suggests that the grains on the tip were of the appropriate size and shape to support surface plasmons excited with our 532 nm laser. The spectra were also

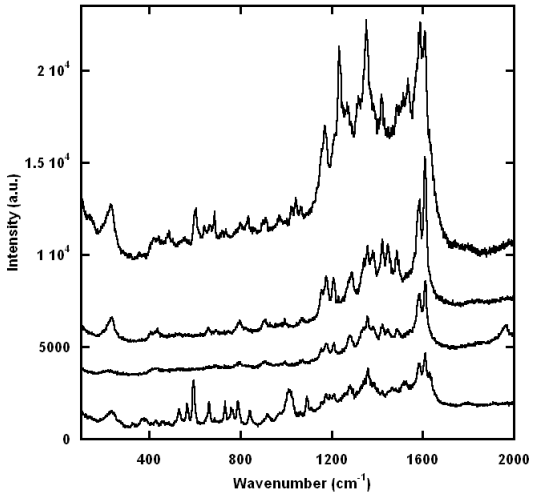

Figure 5.9: Spectra of collagen enhanced by nanoparticles arising from the decomposition of a silver coated tip (Figure 5.8).

very similar to the spectra observed with silver SERS nanoparticles. Most notably the 1585 and 1605 cm^{-1} peaks observed in SERS (Figure 4.10 p40) were extremely prevalent.

5.1.4 Other Promising Techniques

A few other techniques to create an active tip coating were investigated. The success of gold in the SERS experiments, was an incentive to create active gold covered tips. Thermal vapour deposition did not create rough enough gold coatings. Magnetron sputtering is similar to thermal vapour deposition but has the potential to create rougher surfaces. In thermal vapour deposition, a heat source evaporates the metal in vacuum, the vapour particles travel to the substrate and condense back to a solid state. Sputtering is a higher energy process. In sputtering, material is ejected from the solid target material due to bombardment of the target by energetic particles. The sputtered ions can ballistically fly from the target and impact the substrates at higher energies compared to the vapour deposition process. Sputtering has also been used to produce TERS tips [91] and SERS surfaces [92]. In our case, tips were sputtered with gold by R. Sanderson from the J. Dahn group at Dalhousie. A mask was used to create a linear thickness gradient on a substrate. A test substrate was

analysed to determine the position to put the AFM tips during the deposition. The thickness and grain size was measured at many positions along the gradient using x-ray diffraction. Two positions were chosen that would create film thicknesses of 20 and 30 nm. These positions had grain sizes of 16 and 19 nm. When imaged by SEM the gold sputtered tips were found to be very grainy (Figure 5.10A). Unfortunately the tips were not active at our laser's wavelength. The grains were likely too small considering that the active SERS nanoparticles were 65 nm in diameter.

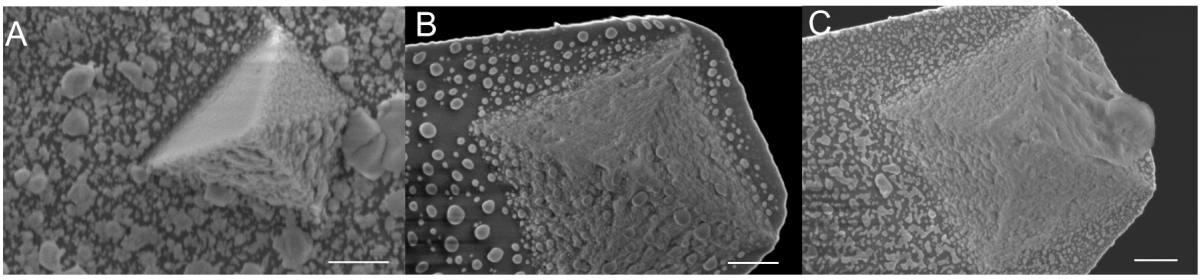

Figure 5.10: SEM images of sputtered TERS tips. A) A MSNL tip sputtered with 30 nm gold. B) A MSCT tip sputtered with 30 nm gold then heated. The sample was heated from 25°C to 200°C with a temperature increase of 5°C/s in 95% argon, 5% hydrogen and left for 5 minutes. C) An MSCT tip sputtered with 20 nm of gold then heated. Scale bars are 10 μm.

Some of the gold sputtered tips were also annealed by R. Sanderson and A. George. The tips were annealed to change the surface structure (Figure 5.10B and C). They were heated to 200°C with a temperature increase of 5°C/s in 95% Argon, 5% Hydrogen and left at 200°C for 5 minutes before cooling. This resulted in a change in film morphology. Many islands were created. However none of these tips were found to be active at our laser's wavelength.

Another emerging TERS tip fabrication technique is to make holes in the metal layer. This can be achieved with a focused ion beam. It works like a reverse nanoparticle producing high enhancements on the inside of the hole. Coaxial TERS tips have shown encouraging results [93]. Due to the success of nanoholes in SERS substrates [94, 95, 96], we attempted to mill a hole at the apex of an AFM tip. We covered the tip with 1 nm of chromium and 120 nm of gold. Unfortunately, with the FIB set-up available, the tip had to be imaged with the argon ions to find the tip. This removed gold atoms from the sample producing a roughened surface and limiting the scanning

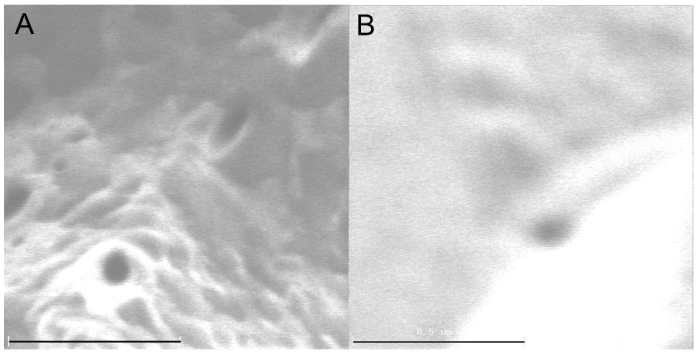

Figure 5.11: AFM tips milled with a focused ion beam. The M0-20 beam (10 picoamps) was used on a Hitachi FB-2000A. This used a beam of focused gallium ions to remove material. A MSNL tip was covered with 1 nm of chromium and 120 nm of gold. The oval holes were milled with a dell time of 30 μs and 300 frames. A) A hole intended to be 61 x 68 nm. The resulting hole was 82 x 94 nm. Note the roughened surface resulting from imaging the tip with the ions. B) A hole intended to be 49 x 55 nm. The resulting hole was 105 x 76 nm. Scale bars represent 500 nm.

power (Figure 5.11) . This combined with the thick layer of gold made it difficult to find the apex of the tip. Holes were created. However redeposition of the gold produced larger holes without crisp edges. When tested in the TERS set-up, none of the tips were active.

5.1.5 Tip Induced Heating

Much like in SERS, heating can be a considerable hurdle especially when imaging in air. Heating can result in the damage of a sample and the reshaping of the tip coating. Fine metal structures are much more unstable than their bulk counterparts [56]. Nanostructures can be reshaped due to the irradiation of lasers [56]. It has been demonstrated that the shape of silver nanostructures can be irreversibly changed after minutes of annealing at 35°C [97]. Reshaping of the coating could result in an inactive tip or changes in the locations of the high enhancement regions. Heating will also increase the likelihood of carbon contamination. Sample heating can change the sample's structure.

Noticeable heat damage was observed when attempting to make a TERS map with a gold coated tip and an illumination of 500μW (Figure 5.12). There is a limit to the illumination power that can be used in TERS. This limit depends on the amount of

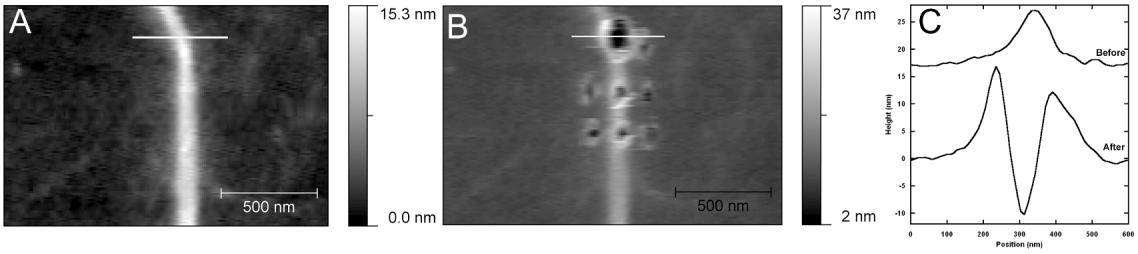

Figure 5.12: Tip induced heating of a sample. A) An AFM image of a collagen fibril on mica taken with a MSNL tip coated with 1.5 nm Cr and 30 nm Au. B) An AFM image after taking a Raman map of the area with a 660 nm laser adjusted to 500 μW. Spectra were taken at 8 points. Each spectra took 300 s to collect. Two spectra were taken at the first point. C) AFM height profile taken across a fibril before and after exposure. The path is indicated on the AFM image with a white line.

heat absorbed, which is proportional to E^2; the higher the enhancement, the higher the heat absorption [98]. Fortunately, the amount of TER signal depends on E^4, which rises more quickly than the heat absorption [98]. To avoid tip heating, TERS illumination was limited to 100μW and acquisition times were limited to 20 s per 1000 cm^{-1} window. No noticeable heat damage was observed with this illumination.

5.2 Results

5.2.1 Fibril Spectra

The best TER spectra were collected in air by tips coated with a 30 nm silver layer by thermal vapour deposition. These coated AFM tips were put in contact with collagen I fibrils to collect enhanced spectra (Figure 5.13A). The TER spectra of fibrils had fewer peaks per spectra than SERS but still had many intense peaks evident in a histogram of the TERS peak positions between 1150 and 1750 cm^{-1} (Figure 5.13B). The peaks between 600 and 1150 cm^{-1} were not common (Figure 5.13C). The ring vibrations at 1585 and 1600 cm^{-1} were also common peaks in the TER spectra (Table 5.1 p74). When compared with an out of contact spectrum of the fibril, the tip was found to enhance the Raman scattering signal by factor of 8000.

All of the TER spectra were collected using tips from 3 different chips. The spectra from each of the 3 chips were summed together to create a spectral sums (Figure 5.14). All of the TER spectra were also added together (Figure 5.14). The

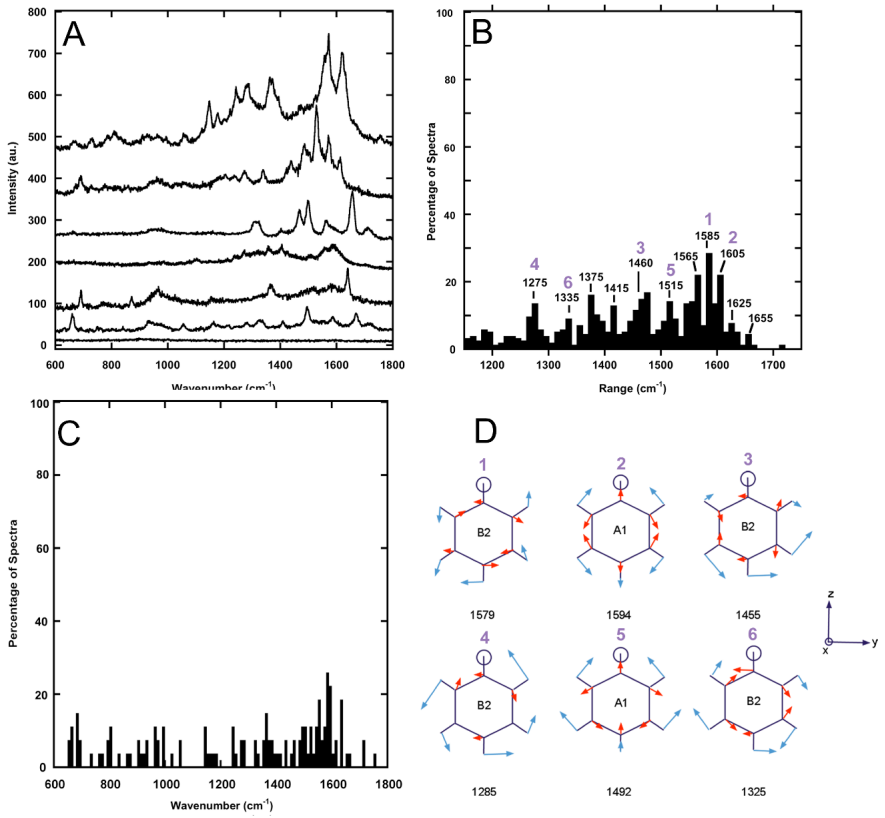

Figure 5.13: Tip enhanced Raman spectra of collagen I fibrils. A) Raman spectra of single collagen I fibrils with Ag-coated tips in contact with fibrils and out of contact (bottom). The Raman scattering signal was enhanced by a factor of 8000 (Equation 3.1 p26). B) Histogram of peak positions observed in 154 TERS spectra taken on 15 collagen I fibrils. C) Histogram of peak positions in 27 TERS spectra between 600 and 1800 cm^{-1}. D) Diagrams of the 6 phenyl vibrational modes observed.

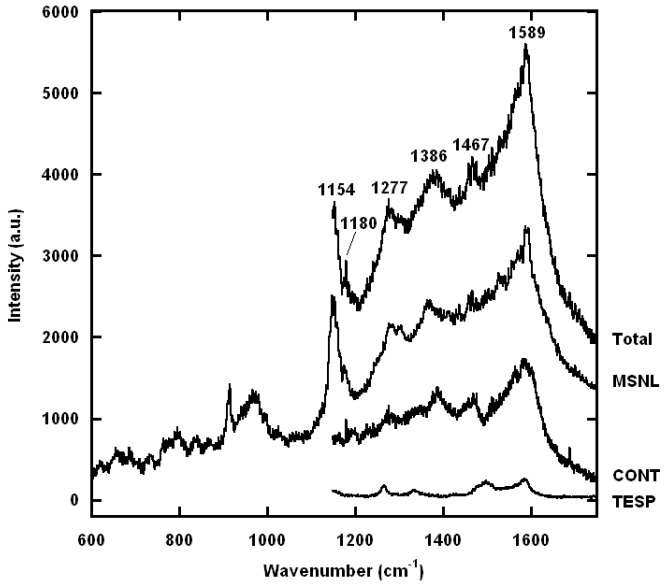

Figure 5.14: Sum of TER spectra taken on each of the 3 chips used in this thesis. The sums of each chip are shown as well as the total sum of TER spectra.

spectral sum did not closely resemble the far field Raman spectrum (Figure 4.8 p36). The total spectral sum had peaks at 1154, 1180 1277, 1386, 1467 and 1589 cm^{-1}. These peaks can be attributed to phenyl ring, Amide III and CH vibrations (Table 5.1 p74). Unfortunately, the 1000 cm^{-1} phenyl peak was not visible in the sum of spectra taken with the MSNL chip. The spectral sums also differed from far-field Raman spectra by not exhibiting strong Amide bands, specifically the Amide I band.

Peak Position (cm^{-1})				Assignment		
Far Field		Collagen TERS				
Collagen	Phe-Phe	Ag hist.	Ag sum	Phe ring	Tyr ring	Other
	1152		1154	15 B_2 1156(5)	9a A_g 1166(24)	
	1182		1180	9a A_1 1175(5)	9a A_g 1166(24)	
	1202			A_1 1205		
1246	1244					Amide III (1248[66], 1251[67])
1289	1283	1275	1277	3 B_2 1285(10)	3 B_{3g} 1286(26)	Amide III (1271[66], 1269[67])
		1335		14 B_2 1325(12)		CH(1314 [66], 1307[67])
	1347					CH(1343 [66], 1340[67])
	1385	1375	1386			CH (1391[67])
	1420	1415				COO^- (1422[66])
1445, 1449		1460	1467	19b B_2 1455(15)		CH (1451,1464[66])
		1515		19a A_1 1492(22)		
		1565		8b B_2 1579(18)	8b B_{3g} 1578(26)	Amide II (1564[67])
	1577	1585	1589	8b B_2 1579(18),	8b B_{3g} 1578(26)	
	1597	1605		8a A_1 1594(20)	8a A_g 1600(29)	

Table 5.1: TERS peaks observed in the 1150-1610 cm^{-1} range compared with far field. The ring vibrations are displayed with their Wilson vibration number, symmetry species and the range is excepted position [70]. Only Raman-active tyrosine modes are included. Assignment is based on previous Raman studies of collagen [66, 67] and Phe-Phe [76], the vibrational modes of substituted benzenes [70, 68, 74] and SERS and TERS studies of amino acids and short peptides [73, 9, 75, 57] and phenyl containing molecules [77, 78].

Peak Position (cm^{-1})						Assignment		
SERS				TERS				
Au hist.	Au sum	Ag hist.	Ag sum	Ag hist.	Ag sum	Phe ring	Tyr ring	Other
1165		1155	1152		1154	15 B_2 1156(5)	9a A_g 1166(24)	
	1170	1175			1180	9a A_1 1175(5)	9a A_g 1166(24)	
1195	1198	1215	1202			A_1 1205	A_g 1210(10)	
1245	1245	1235						Amide III (1248[66], 1251[67])
1265	1269	1285	1270,1285	1275	1277	3 B_2 1285(10)	3 B_{3g} 1286(26)	Amide III (1271[66], 1269[67])
	1315		1336	1335		14 B_2 1325(12)		CH(1314 [66], 1307[67])
		1355	1360	1375	1386			CH(1343 [66], 1340[67], 1391[67])
1405	1414	1410	1407	1415				COO^- (1422[66])
1445	1442	1445	1451	1460	1467	19b B_2 1455(15)		CH (1451,1464[66])
1485	1495	1485	1491	1515		19a A_1 1492(22)		
	1541	1530	1540					Amide II (1526-1576[10])
1565				1565		8b B_2 1579(18)	8b B_{3g} 1578(26)	Amide II (1564[67])
1585	1587	1585	1577,1587	1585	1589	8b B_2 1579(18),	8b B_{3g} 1578(26),	
		1605	1608	1605		8a A_1 1594(20)	8a A_g 1600(29)	

Table 5.2: TERS peaks observed in the 1150-1610 cm^{-1} range compared with SERS. The ring vibrations are displayed with their Wilson vibration number, symmetry species and the range is excepted position [70]. Only Raman-active tyrosine modes are included. Assignment is based on the vibrational modes of substituted benzenes [70, 68, 74], Raman studies of collagen [66, 67] and SERS and TERS studies of amino acids and short peptides [73, 9, 75, 57], insulin [10] and phenyl containing molecules [77, 78].

5.2.2 Line Scans

An AFM tip was coated with 30 nm Ag nanoparticles and was used to image collagen I fibrils in contact mode in air (Figure 5.2A p62). This allowed us to obtain TER spectra (Figure 5.15) at 35 points along a 1.33 μm line passing over a collagen I fibril. The peaks were not as intense as the SER spectra and had a strong background that resembled the spectrum of Ag nanoparticles in (Figure 4.5 p33). There were 1189 and 1635 cm^{-1} peaks that could be used to map the fibril. The first peak corresponds to a phenylalanine or tyrosine ring vibration. The second peak can be attributed to an Amide I vibration. The intensity of the ring vibration along the line map matched the height profile almost perfectly (Figure 5.15). The FWHM of the fibril along the line was found to be 660 nm in the height profile and 730 nm in the peak intensity map.

Using tapping mode, a silver vapour deposition tip (Figure 5.6B p66) was also used to make a line profile across a collagen I fibril in air. A 1.14 μm line across a fibril was scanned on an AFM image with spectra taken every 39 nm (Figure 5.16). Spectra taken at points on the fibril contained a 1330 cm^{-1} peak not observed in the other spectra (Figure 5.16) that can be attributed to either a phenyl ring vibration or a CH vibration (Table 5.1 p74). The spectra of the points taken on the fibril were homogeneous (Figure 5.17). Similar spectra with shifted peaks and an absent 1330 and 1505 cm^{-1} peak were observed in a region next to the fibril on what could possibly be a small aggregate of collagen molecules (Figure 5.16). The 1505 cm^{-1} peak can also be attributed to a phenyl ring vibration. This spectra contained 1485 and 1565 cm^{-1} peaks not present in the collagen fibril spectra. The 1485 cm^{-1} peak can be attributed to a phenyl ring and the 1565 cm^{-1} can be attributed to a ring vibration or an Amide II vibration (Table 5.1 p74). It did however have 1580 cm^{-1} (1590 cm^{-1} in the fibril spectra) and 1260 cm^{-1} in common with the collagen fibril that can be attributed to ring vibrations and ring or Amide III vibrations respectively. A plot of the intensity of the 1330 cm^{-1} peak along the scan was comparable to the AFM height profile of the fibril (Figure 5.16C). The full width half maximum (FWHM) of the fibril along the line was found to be 100 nm in both the height map and the 1330 cm^{-1} peak intensity map.

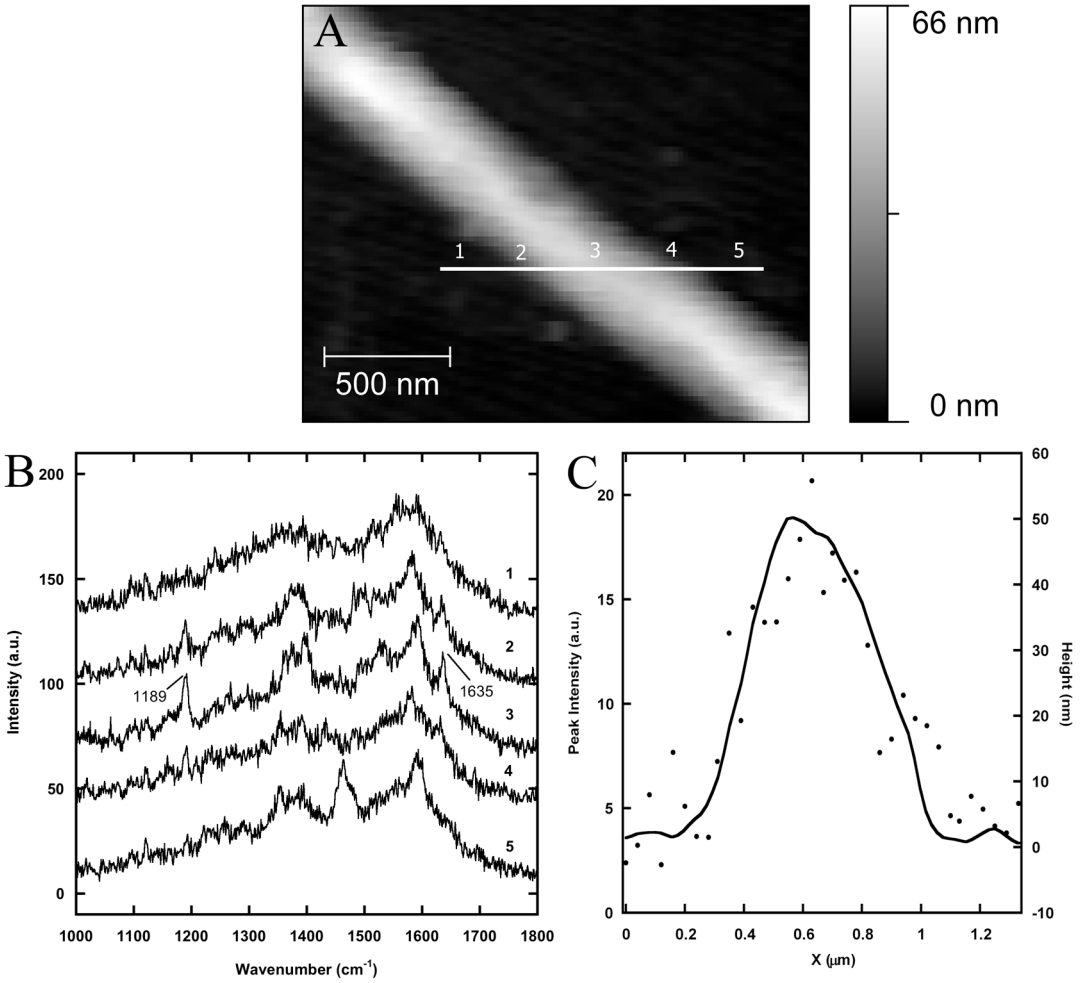

Figure 5.15: Enhanced Raman line map of a fibril obtained with a 30 nm Ag nanoparticle covered tip. A) Contact mode AFM height image in air of a collagen I fibril obtained with a 0.1 N/m MSNL cantilever. The path of the map is represented with a white line. B) Enhanced Raman spectra of the fibril at different points along the line. C) The intensity of the 1189 cm^{-1} peak (dots) and the height of the sample (line) along the map. The height map has a FWHM of 660 nm. The peak intensity map has a FWHM of 730 nm.

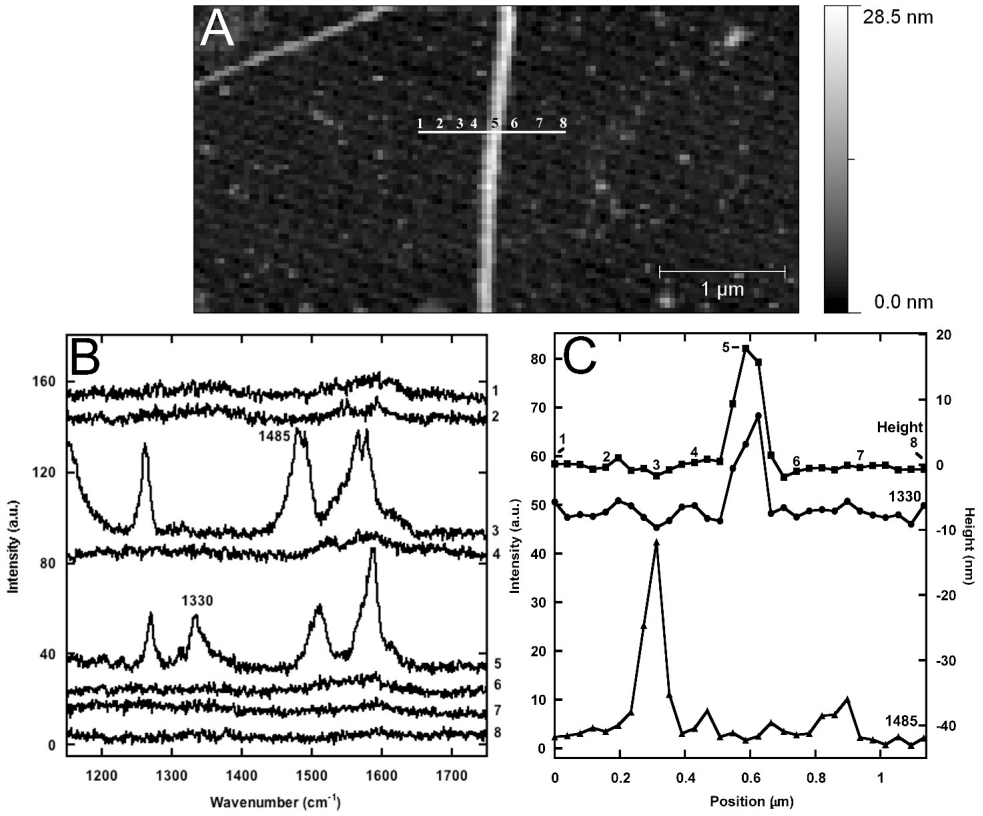

Figure 5.16: Tip enhanced Raman line scan of a collagen I fibril collected in tapping mode in air at an oscillation amplitude of 10 nm. A) AFM height image of the collagen I fibril obtained with a TESP-SS cantilever prior to Raman line scanning. The white horizontal line across the fibril represents the 1.14 μm path of the Raman line scan. B) The tip enhanced Raman spectra at different points along the 30 point path. C) Height profile of the collagen I fibril (squares) and the intensities of the 1330 (circles) and 1485 cm^{-1} (triangles) peaks along the Raman line scan. The height profile and the intensity profile at 1330 cm^{-1} both have a FWHM of 100 nm.

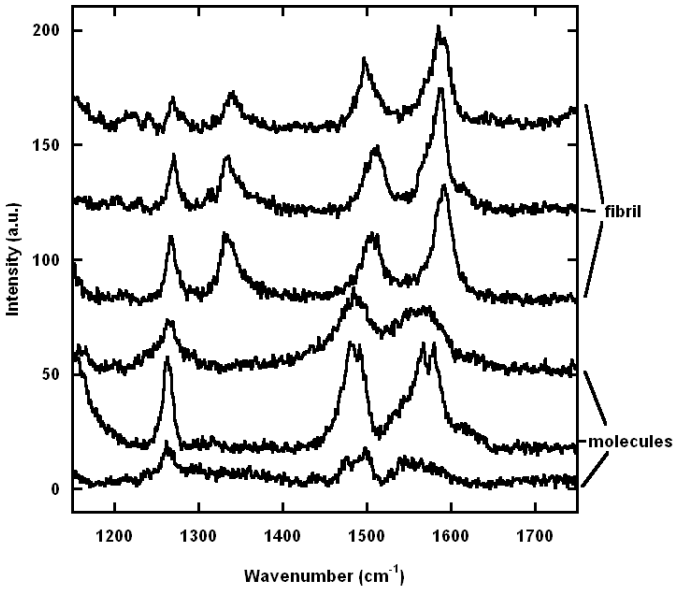

Figure 5.17: Spectra collected at the 3 points on the fibril and 3 points near a potential aggregate of collagen molecules probed in the line scan shown in Figure 5.16

5.2.3 2D Mapping

A silver vapour deposition tip (Figure 5.6A) was used to acquire a 2D map of a collagen I fibril in contact mode in air. In many cases, when making a map, the length of scan would result in large amounts of tip drifting, tips becoming inactive during the scan or even tips that came out of contact during the scan. In this particular case, we were able to produce a successful TERS 2D map (Figure 5.18). The total scan took roughly 30 minutes to complete. The height was measured at each point during the Raman map. Each row of height underwent a background subtraction and the resulting height profiles did not suggest any significant xy drifting (Figure 5.18C). As expected from our SERS data, we were not able to find a single peak that would map the fibril consistently. Interestingly, the strongest TERS signals corresponded to positions that appeared to not be on the collagen fibril (Figure 5.18B and D).

This scan was made with a contact mode tip. One of the disadvantages of a contact mode tip over a tapping mode tip is that they are more prone to wear. When the tips are covered with a layer of silver, the tips have a potential to become highly deformed while imaging. The SEM image of this tip taken after the TERS experiments were complete revealed a highly deformed tip (Figure 5.6A). The tip apex seemed to be

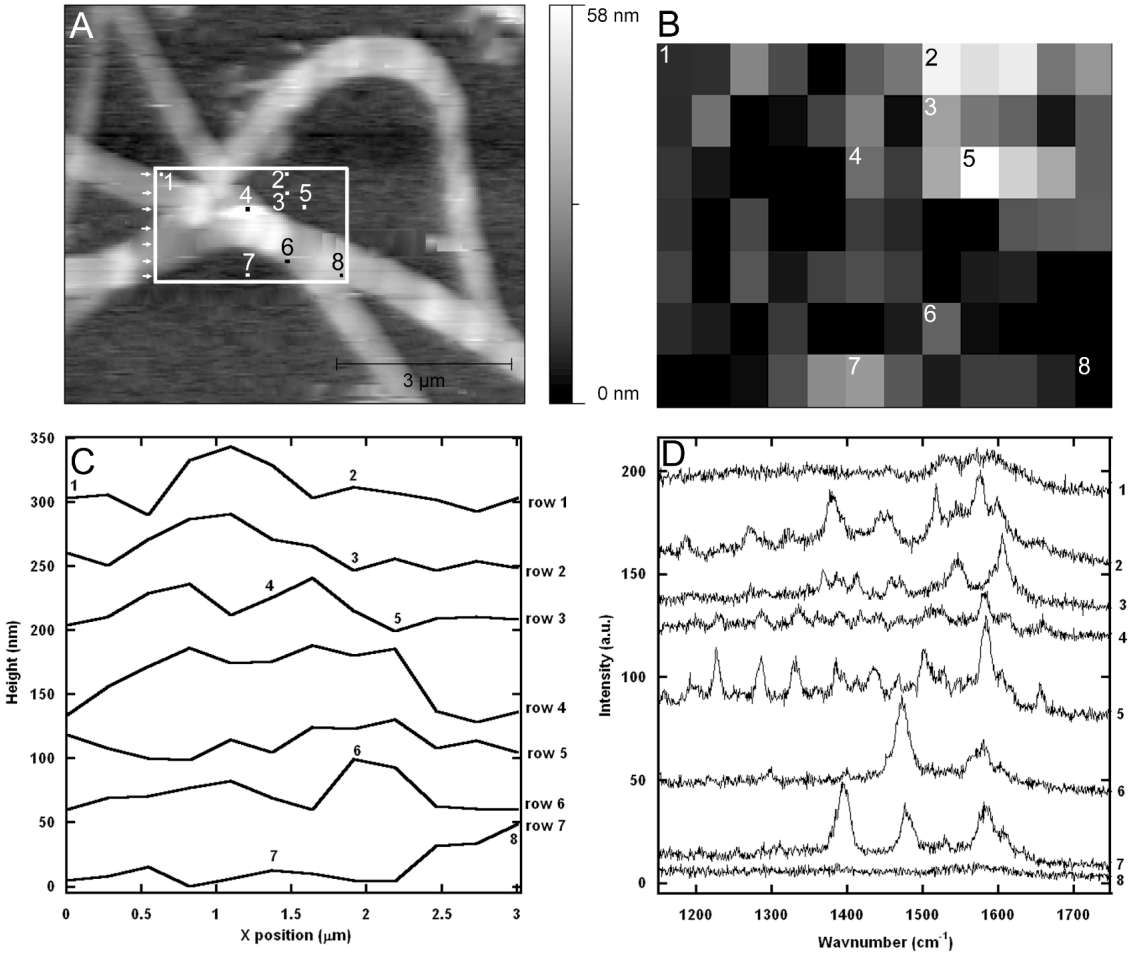

Figure 5.18: TERS map of a Collagen Fibril taken with a 30 nm silver coated CONT cantilever (Figure 5.6A). 84 points were taken with a 532 nm 100 μW laser was used with an acquisition time 20 s. Spectra were collected left to right starting with the top left spectra (point 1) and ending with the bottom right spectra (point 8) A) The AFM map of the area taken before the Raman experiments. The white rectangle represents the area probed with the beginning of each row marked with arrows and points of interest numbered. B) The total intensity of the TERS spectra in the range 1150-1750 cm^{-1} after background removal taken at each point. Lighter rectangles represent points with intense spectra C) The height of cantilever at each point where a Raman spectrum was acquired. The background of each row due to z drifting was removed. Each row was also moved vertically on the graph to display all rows. D) Sample spectra taken at point with intense peaks and notable positions. The points are marked on the other subfigures.

up to 10μm in diameter. This SEM image was taken after the tip became inactive and it was likely in a better state during the scan. But it is possible that the region

of the tip producing the high enhancements was not at the lowest point of the tip, responsible for the height measurements, but on the side of the tip. Points 6 and 7 produced similar spectra and yet point 6 was on the edge of a fibril and point 7 was on the glass in the height image. They were however both around 140 nm to the right of a fibril. Points 5, 3 and 2 also produced spectra with strong peaks while being on the glass in the height image.

5.2.4 Amide I Band

Amide I bands were also observed in 29 of the TER spectra. The mean width of the TERS Amide I bands were $15\pm7\,\mathrm{cm}^{-1}$. Not only was this much narrower than the $90\,\mathrm{cm}^{-1}$ wide far field Raman Amide I band, it was also narrower than the SERS Amide I bands. The SERS Amide I bands were 27 ± 12 and $22\pm11\,\mathrm{cm}^{-1}$ wide for silver and gold respectively. The TERS Amide I peak positions were analysed by a histogram (Figure 5.19B) to compare to the far field Raman band (Figure 5.19A, Table 5.3 p85). Unfortunately, there were not enough TERS Amide I bands for good statistics, so a histogram using both the SERS and TERS peaks was made (Figure 5.19C). The mean width of the SERS and TERS peaks was $22\pm12\,\mathrm{cm}^{-1}$. The far field band was fit with 25-30 cm^{-1} wide Gaussians.

5.3 Discussion

5.3.1 Drift and Tip Damage

Tip drifting can be a considerable difficulty of TERS scans. Drift in the z direction can result in tips coming out of contact with the sample. Drifting in the x and y direction can result in a Raman image that does not correspond to the AFM image. Long term pre-scanning can reduce drift, but also might result in tip contamination and wear. Also short scans such as line scans can reduce the effects of drifting. Drifting can be more of a problem in Raman maps with their long total acquisition time. Many of the attempted 2D Raman maps only produced good spectra in the first few points and the tip would even come out of contact with sample during the scan.

Tip damage seemed to be a substantial issue. The best line scan was made in

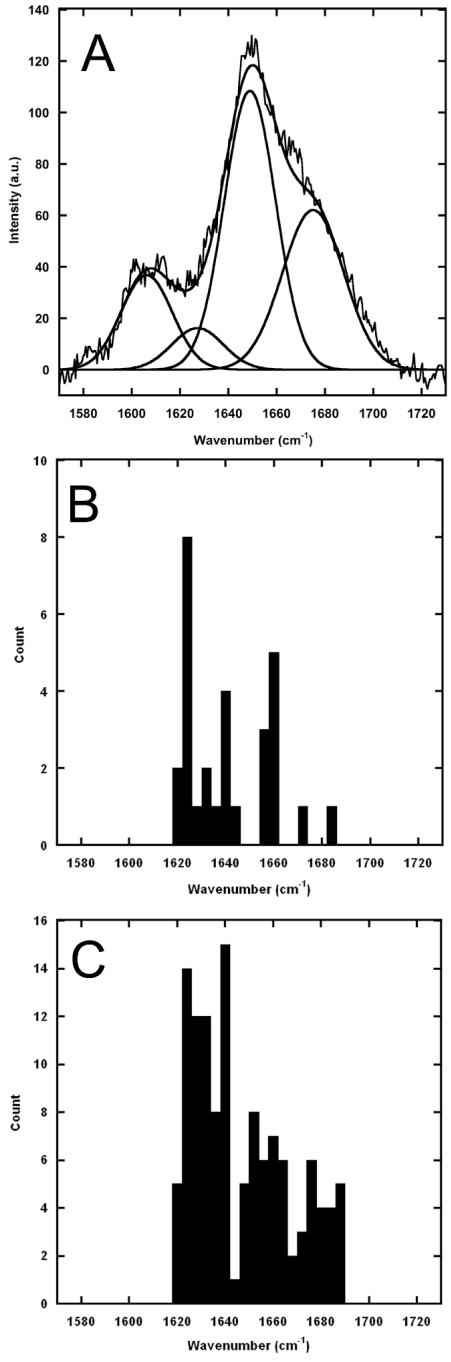

Figure 5.19: Comparison of the diffraction limited and enhanced Raman Amide I peaks for collagen I fibrils. A) Peak fitting of the far field Amide I band (Figure 4.15A). B) Histogram of the Amide I peak positions observed in TERS. The average FWHM of the Amide I band in the 29 silver TERS spectra was $15\pm7\,\mathrm{cm}^{-1}$. C) Histogram of the Amide I peak positions observed in both SERS and TERS.

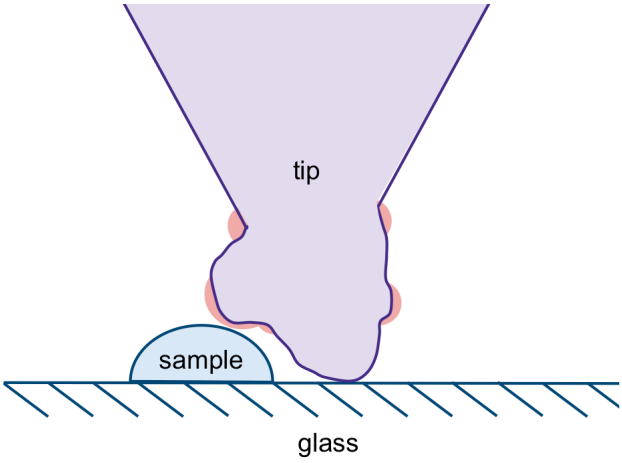

Figure 5.20: An Illustration of a deformed tip that would have the potential to give TERS signals When appearing to not be on the fibril in an AFM height images.

tapping mode. The Raman map made using contact mode suggested that the tip was considerably deformed. Deformation of a tip from scanning can be a problem with normal AFM scanning. Adding a layer of malleable silver can understandably make this more of an issue. Although a deformed tip can still be active, it might not be at the lowest point, making mapping much harder (Figure 5.20). When a deformed tip has regions of high enhancements that are located above the tip apex, it is harder to compare AFM images with Raman maps. Any deformation of the tip during the scan could result in different high enhancement regions or even a completely inactive tip. This makes the analysis of maps difficult and enforces that it is extremely important to protect the tip from wear when mapping.

5.3.2 TERS vs. Far Field

Much like in the SER spectra, we observed peaks in the TER spectra not seen in diffraction limited Raman (Table 5.1 p74). In previous tapping mode studies, the Raman intensity of a sample was found to exponentially decay with increasing tip-sample separation with a decay length of 2.8 nm [11]. The tip enhanced Raman experiments only probed bonds in the first layer of collagen molecules on the surface of the fibril. Similarly to the SERS experiments, the spectra were dominated by ring vibrations. Amide bands, C-H and COO^- vibrations were also observed.

Unfortunately the 1000 cm^{-1} peak was not visible. The spectral sums were not as helpful as the SERS sums were. The SERS sums were used to determine the average intensities of each symmetry species relative to the A_1 symmetry species. The TERS sum displayed 5 phenyl modes, 4 of which were B_2 modes and only 1 was an A_1 mode. This made determining the orientation of the phenyl ring with relative intensities by this method much less accurate. However, the prevalence of ring vibration modes does suggest a great deal of rings and other amino acid residues on the top surface of the fibrils.

5.3.3 TERS vs. SERS

Although SERS and TERS have very similar mechanisms, they have different uses and produce different spectra. TERS has the distinct advantage at being able to probe any area on a sample. Unfortunately, scanning a sample with TERS has its own disadvantages. When scanning a soft biological sample, the tip exerts a force, resulting in wear of the tip and minor compression and deformation of the sample. Additionally, the same tip is used for all measurements on the sample and can become contaminated. If material attaches to the tip, it can be brought along and contribute to the spectra at all points. SERS does not have this problem but lacks the spatial resolution of TERS. In SERS, one cannot control the positions of the nanoparticles without using some form of targeting, such as antibodies [99] or nanoprinting [100]. Furthermore, all nanoparticles within the 1 μm laser spot will be excited. SERS does not compress the sample, however the biomaterial does attach to the nanoparticle. Some vibrations may be altered due to the molecules interaction with the surface of the nanoparticle resulting in potentially shifted peaks [73]. Whenever possible both techniques should be used on the same sample as they are complimentary in nature.

To compare the SERS and TERS techniques, we used the histograms of peak positions and the spectral sums (Table 5.2 p75). The peaks in the TERS histogram were very similar to the peaks in the silver SERS histogram with only two TERS peaks not observed in the the SERS histogram. Similarly, the TERS sum had only one peak not observed in the silver SERS sum. Many TERS peaks were observed in both gold and silver SERS as well. These peaks can be assigned to ring vibrations around 1579, 1155, 1165 and 1492 cm^{-1}, ring or CH vibrations around 1325 and 1455 cm^{-1}, a ring

Position (cm^{-1})				Assignment
Far Field Raman	SERS	TERS	TERS +SERS	
1627	1628	1632	1632	collagen helix
	1640			
1649	1652	1658	1656	α
	1664			
1675	1676		1675	β

Table 5.3: Amide I band positions. The peak positions and FWHM used in the deconvolution of the far field Raman spectrum of the Collagen I Amide I band (Figure 5.19A). The centers of the 5 strongest peaks in the histogram of SERS Amide I peak positions (Figure 4.15B). The centers of clusters of peaks found in the histogram of TERS Amide I peaks (Figure 5.19B) as well as the histogram containing SERS and TERS peaks (Figure 5.19C).

or Amide III vibration around 1285 cm^{-1} and the symmetric COO^- stretch around 1410 cm^{-1} (Table 5.2 p75). A ring vibration around 1205 cm^{-1} was observed in gold and silver SERS but was not observed in TERS (Table 5.2 p75). The similarities between the SER and TER spectra were stronger than the differences. This supports the idea that TERS can extract structural information similar to SERS but with superior positioning power.

5.3.4 Amide I Band

The narrow Amide I bands found with TERS were comparable to the bands found with SERS and the peak decomposition of the far field Raman band (Figure 5.19 p82). The far field band was fit with Gaussian peaks at 1627, 1649, 1675 cm^{-1} which can be assigned to collagen-helix, α-helix and β-sheet secondary structures respectively [80, 82, 83].

Although there were not very many TERS spectra with Amide I bands, the histogram revealed a wide cluster of peaks around 1632 cm^{-1} and a narrow cluster around 1658 cm^{-1}. These clusters can be attributed to collagen- and α-helices (Table 5.3). The combination of the SERS and TERS amide I bands had a distribution of peak positions that had three distinct clusters around 1632, 1656 and 1675 cm^{-1} (Table 5.3). These clusters could be attributed to collagen-helix, α-helix and β-sheet respectively.

The narrow TERS bands suggests that even less of the fibril is being probed than the SERS spectra. We are observing one type of secondary structure at a

given location. This allows us to assign secondary structures without the need of any deconvolution. Our results also confirm the presence of α-helix and β-sheets structures at the surface as well as the characteristic collagen-helix of the fibril as expected.

5.4 Conclusion

The TERS experiments presented in this chapter demonstrated the ability of TERS to map surface structure and molecules on fibrils. The spectra were dominated with the bands attributed to the vibrations of amino acid residues. The TER spectra were comparable to the spectra found in SERS. The TERS Amide I peaks agreed with the SERS result which suggests the presence of collagen-helix and α-helix structures at the surface of the fibril.

Due to the success of the gold nanoparticles in the SERS experiments, it is possible that technique could be improved with gold coated tips. If a $1000\,\mathrm{cm}^{-1}$ is present in most of the gold tip spectra, it can be used to more effectively map the fibril. Scanning the sample in modes that minimize tip wear could improve both the longevity of the active tips and the resolution of the TERS maps. Increased scanning stability would minimize the likelihood of the tip becoming out of contact during the scan and drifting.

Chapter 6

Tendon Fascicles

The fibrils used in the previous chapters were reassembled from collagen extracted from rat tails. Rat tail tendon is made up of a number of fascicles bound together by connective tissue [101]. The organization of the fascicle results in a structure that is highly resistant to tensile strain while maintaining its flexibility [102]. A fascicle is essentially organized fibrils. A bunch of collagen fibrils interwoven with proteoglycans form a collagen fiber [103]. A fine sheath of connective tissue called endotenon covers each collagen fiber and binds them together [104]. This connective tissue contains collagen-producing cells called tenocytes [105]. A bunch of collagen fibers forms a subfascicle, and a group of subfascicles forms a fascicle [104]. The collagen I fibrils found within the fascicle have a natural crimp to them that straightens during fascicle extension [102, 101].

SERS can be employed to study this higher level of structure. A rat tail tendon fascicle provided by S. Veres was cut into segments resulting in several shorter fascicles. These fascicles were soaked in a colloidal solution of 30, 60 or 70 nm gold nanoparticles diluted 4X or 65 nm gold nanoparticles for 17 hours. The samples were dried and examined with the Raman spectrometer. The fascicles were illuminated with a 660 nm laser adjusted to 100 μW through a long working distance 40X objective. An acquisition time of 20 s was used to collect the SER spectra per 1000 cm^{-1} window. The spectra of a fascicle not soaked in nanoparticles was also taken with an acquisition time of 100 s.

6.1 Results and Discussion

6.1.1 Far Field Raman

The control fascicle that was not soaked in nanoparticles was first examined by far field Raman. It was compared to the far field spectra of fibrils used as references in the

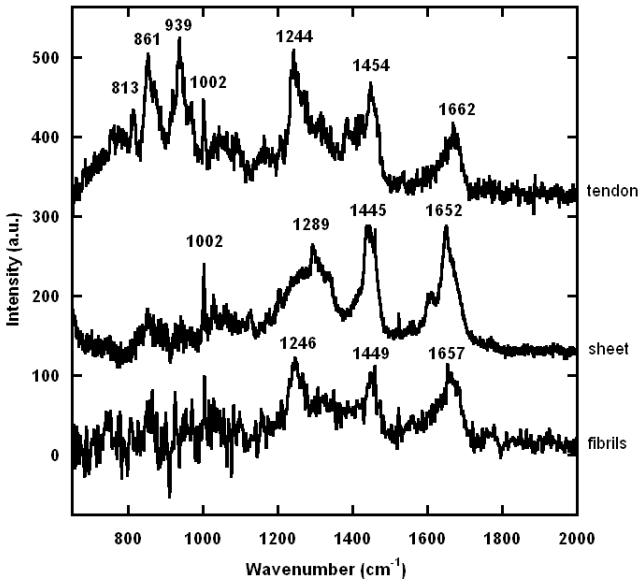

Figure 6.1: Far field Raman spectra of collagen I taken at different levels of organization. Raman spectra was taken of a fascicle removed from a rat tail tendon as well as a dense network of fibrils and a sheet of fibrils.

SERS and TERS chapters (Figure 6.1). Each of these spectra were taken of different levels of collagen organization. The fibrils were either organized into a dense network, a sheet several microns in thickness and a tendon fascicle several hundred microns in thickness. Due to the large size of the fascicle, there was less of a contribution of glass to the spectrum. A few Raman bands were observed in the fascicle spectra that were not visible in the previous spectra. These bands were found at 813, 861 and 939 cm^{-1}. They have been observed in previous collagen spectra [66, 67] and can be assigned to C-C vibrations (Table 6.1). The fascicle spectra also possesses a distinct phenylalanine ring vibration at 1002 cm^{-1} and a C-H band at 1454 cm^{-1}. The Amide bands they share in common with the previous spectra are of greater interest. The Amide I and Amide III bands both contain structural information. The fascicle spectra resembled the spectra of the dense network of fibrils more than the sheet, specifically with the Amide III band. This suggests that the secondary structure of the fibrils examined in the SERS and TERS chapters are very similar to the structure of fibrils in a rat tail tendon.

Tendon	Sheet	Fibrils	Assignment
813			CC backbone (821[66], 810[67])
861			CC of Proline ring (856[66])
939			CC (938[66], 934[67])
1002	1002		Phe ring (1006[66], 1001[67])
1244	1289	1246	Amide III (1248,1217[66], 1251,1269[67])
1454	1445	1449	CH (1451[66])
1662	1652	1657	Amide I (1670[66], 1655[67])

Table 6.1: Positions and assignments of the far field Raman bands observed in Figure 6.1.

6.1.2 Surface enhance Raman Spectroscopy

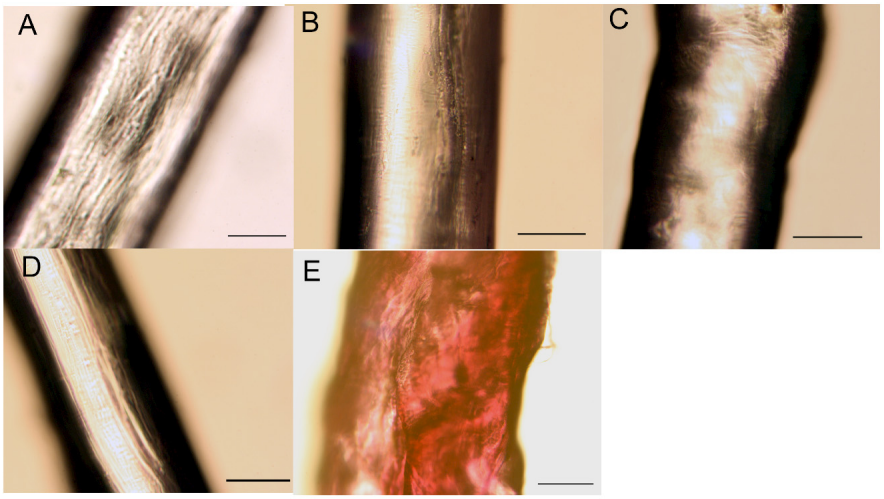

Figure 6.2: Optical images of fascicles soaked in nanoparticle solutions (colour available in electronic version). The fascicles were soaked in A) no nanoparticles B) 60 nm gold nanoparticles C) 65 nm gold nanoparticles D) 70 nm gold nanoparticles E) 30 nm gold nanoparticles. Scale bars represent 100 μm.

The tendon fascicles provided appeared as white fibers due to scattering (Figure 6.2A). The nanoparticle solutions that the fascicles soaked in were pink. When the fascicles were soaked in 30 nm gold nanoparticles, the fascicle adopted a dark pink colour. When the fascicles were soaked in the 60, 65 and 70 nm gold nanoparticles they remained white. This suggests that the larger nanoparticles had a greater difficulty penetrating the sample. When examined with an optical microscope, the fascicles soaked in 60 and 70 nm gold nanoparticles retained there longitudinal fiber organization (Figure 6.2B,D). However, in the 65 nm gold nanoparticle soaked fascicle

this organization was less apparent (Figure 6.2C). The 30 nm gold nanoparticle soaked fascicle appeared deformed, indicating that some rearrangement of the collagen fibrils occurred during nanoparticle penetration (Figure 6.2E).

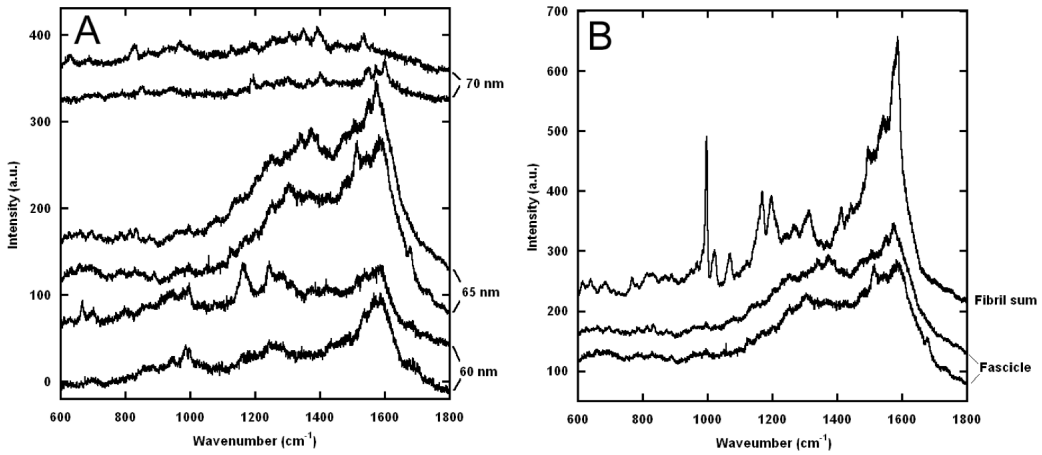

Figure 6.3: A) SER spectra of a fascicles soaked in 60, 65 or 70 nm gold nanoparticle solutions. The intensity of the 65 nm nanoparticle soaked fascicle spectra was scaled down to 25% for comparison with the other spectra. B) The spectra of 65 nm gold nanoparticle soaked fascicles and the sum of the 65 nm gold SERS spectra of collagen fibrils (see subsection 4.2.4).

The tendons soaked in 60, 65 and 70 nm gold nanoparticles exhibited SER spectra (Figure 6.3A). The 65 nm nanoparticle soaked fascicle had very intense SER spectra. The spectra resembled a SER spectra sums (Figure 4.13). The spectra had a shape similar to the gold SERS spectral sum but had less defined peaks (Figure 6.3B). The 60 and 70 nm nanoparticle soaked fascicles produced spectra with better defined peaks.

The 65 nm gold nanoparticle spectra were missing the 1000 cm^{-1} phenyl ring vibration peak among others observed in the fibril spectral sum. The 65 nm gold nanoparticles were older in these experiments than when they were used in the experiments of the previous chapter. It is possible that they were clumped together in the solution and attached to collagen differently. It is also possible that the nanoparticles attached to non collagen I materials. Although tendon fascicles has a large amount of collagen I, it is held together with connective tissue. Materials such as proteoglycans or even tenocytes can be enhanced. The 60 and 70 nm gold nanoparticles were chosen for the

next experiments due to the more defined peaks in their spectra.

6.1.3 Penetration

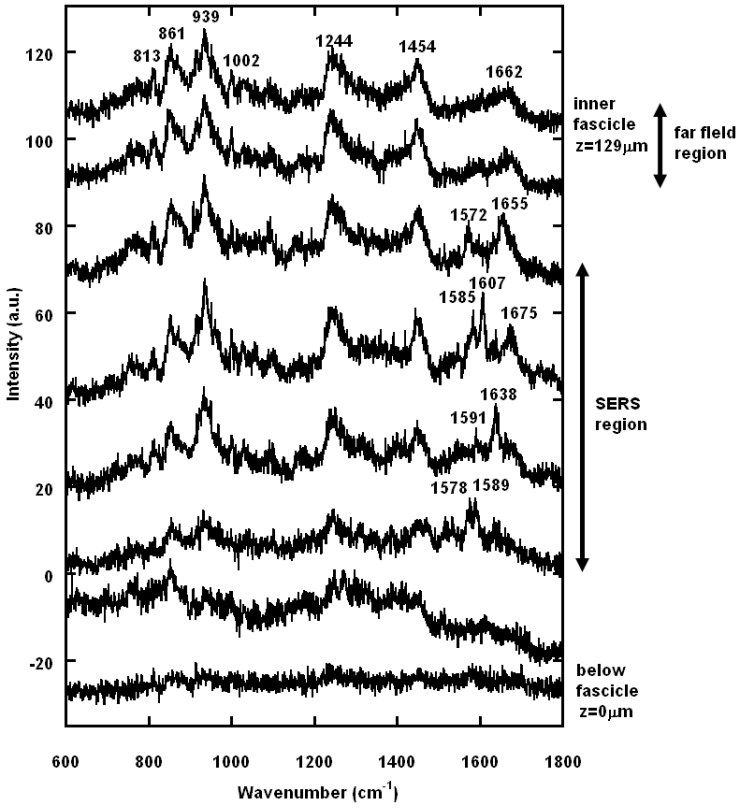

Figure 6.4: The penetration profile of nanoparticles in a fascicle. A fascicle was soaked in 60 nm gold nanoparticles for 17 hours. Spectra were taken sequentially increasing the height of the focal plane between each spectra. The spectra shown above are separated by 18.4 μm steps.

Spectra were taken at different focal planes 8.4 μm apart inside a fascicle soaked in 60 nm gold nanoparticles (Figure 6.4). The first bands that were observed when moving into the fascicle were SERS bands. SERS bands were present in 4 spectra. Thus the nanoparticle penetrated at least 55 μm. The SERS bands were weak but were very narrow. There was a gradual increase in the intensity of the far field bands of the fascicle. Eventually, the SERS peaks were no longer visible and only the far field spectrum remained. The SERS bands observed included an Amide I band observed at 1638, 1655 and 1675 cm^{-1}. The bands can be attributed to collagen-helix,

α-helix and β-sheet structures respectively. The other SERS bands can be assigned to phenylalanine or tyrosine ring vibrations.

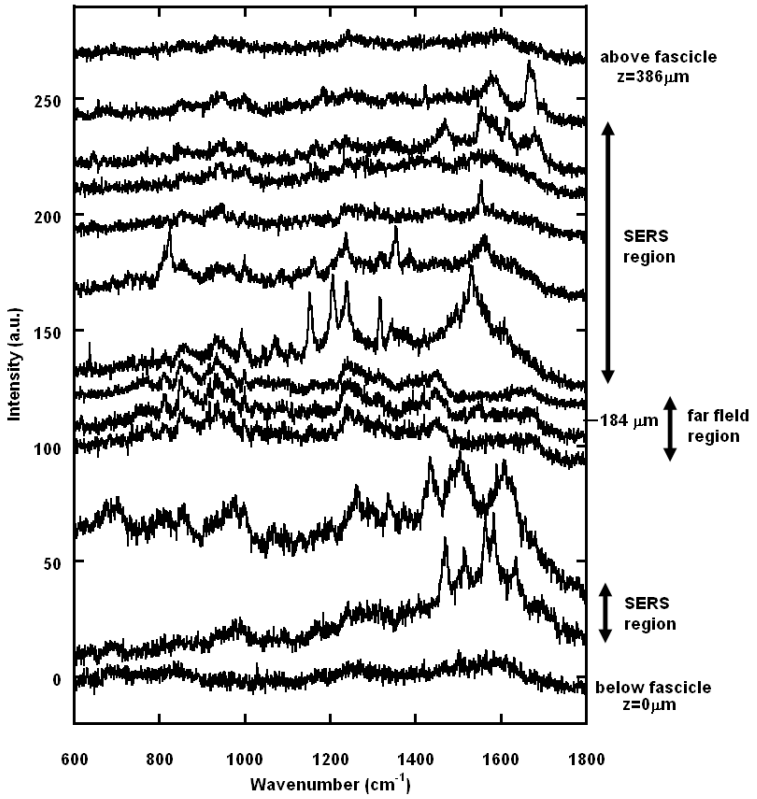

Figure 6.5: The penetration profile of nanoparticles in a fascicle. A fascicle was soaked in 70 nm gold nanoparticles for 17 hours. Spectra were taken sequentially increasing the height of the focal plane by 18.4 μm between each spectra. Each of the spectra shown are separated by 18.4 μm except for the 184 μm gap highlighted were similar spectra were not shown.

A larger height range was used for a fascicle soaked in 70 nm gold nanoparticles. Spectra were taken along the entire height of the fascicle (Figure 6.5). When the focal plane was at the bottom or top of the fascicle, enhanced Raman spectra were observed. When it was focused inside the fascicle, the far field Raman spectra of the fascicle was observed. The height of the fascicle was measured to be 350 μm based on the Raman spectra. The nanoparticles penetrated at least 18 μm at the bottom of the fascicle and 92 μm at the top. Much like with the 60 nm nanoparticle soaked fascicle, the SER spectra of the fascicle exhibited peaks that can be attributed to Amide I and amino acid residue vibrations. Amide I bands were observed at 1636 and 1658 cm^{-1}

below the fascicle and 1670 and 1680 cm^{-1} above the fascicle. The residue bands observed in the SER spectra include the characteristic tyrosine ring vibration at 825 cm^{-1}, phenylalanine ring vibrations around 1580 and 1600 cm^{-1}. Also observed were possible Amide II bands around 1550 cm^{-1}, Amide III bands around 1240 and 1260 cm^{-1} and CH bands around 1330 and 1450 cm^{-1}

6.1.4 Amide I Band

Many of the enhanced fascicle spectra contained Amide I bands. The positions of the bands varied from 1636 to 1680 cm^{-1}. The width of these bands was found to be 24 ± 11 cm^{-1}. This is very similar to the 22 ± 11 cm^{-1} width of the Amide I bands of the collagen I fibrils found with gold nanoparticles in the SERS chapter. There does not seem to be very much of a difference between the application of gold nanoparticles to individual collagen I fibrils and tendon fascicles.

6.2 Conclusion

The soaking of rat tail tendons in gold nanoparticles produced enhanced spectra in the outer regions of the fascicle. The penetration of the nanoparticles into the fascicle was measured using a high working distance 40X objective and a Raman spectrometer. This demonstrated the technique's ability to do SERS sectioning of a sample. Recently cancer targeting antibodies have been attached to metal nanoparticles. These nanoparticles have been used under *in vivo* conditions for tumour detection in live animal models [106, 107]. Similar penetration experiments can be used on different tissues testing the penetration of the functionalized nanoparticles.

Many Amide I bands were observed in the SERS spectra. The Amide I band is of particular interest in tendons. Tendons mechanical properties are often tested by stretching tendons. Ideally the SERS Amide I bands can be used to measure changes in secondary structure during stretching experiments. Far field Raman stretching experiments have been carried out on a fiber removed from a rat tail tendon [108]. Their Amide I band had a small positive shift during stretching. The SERS Amide I bands observed in these experiments can be used to test if the collagen molecules adopt a structure with more β-sheets at the point of fracture. The sectioning power of

the SERS experiments can even be used to look at the changes in secondary structure on the outer fascicle and compare them to changes inside the fascicle.

Chapter 7

Conclusion

In this thesis, we have demonstrated the ability of nanoscale Raman techniques to obtain spatially localized surface spectra of collagen fibrils assembled *in vitro*.

7.1 Summary of Results

In the SERS experiments, enhanced spectra of collagen I fibrils dominated by contributions from the amino acid residues at the fibril's surface were observed. 65 nm gold nanoparticles were found to produce the highest quality SER spectra. With these spectra, the phenylalanine residue had a preferential orientation with the edge of its ring tilted towards the nanoparticles surface. The SERS Amide I bands confirmed the presence of the characteristic collagen-helix as well as α-helix and β-sheet structures at the surface of the fibril.

In the TERS experiments, the enhanced spectra of collagen I fibrils were also dominated by contributions from the amino acid residues at the fibril's surface. The ability of TERS to map surface structure and molecules on fibrils was demonstrated. The TERS Amide I peaks agreed with the SERS results and suggested the presence of collagen-helix and α-helix structures at the surface of the fibril.

In the tendon experiments, fascicles soaked in gold nanoparticles produced enhanced spectra in the outer regions of the fascicle. Many Amide I bands were observed in the SERS spectra as well as amino acid residue vibrations.

The FWHM of the Amide I bands in Ag SERS, Au SERS, Ag TERS and Au SERS of fascicles was found to be 27±12, 22±11, 15±7 and 24±11 cm^{-1} respectively. Considering that the FWHM of the Amide I band found in far field Raman was 90 cm^{-1}, these bands are all extremely narrow.

7.2 Significance

The examination of proteins with SERS and TERS is not yet a routine investigation. Very few proteins have been examined with these techniques. To the best of our knowledge, this thesis, along with a paper on this topic [14], are the first characterization of collagen with SERS or TERS. The enhancement of the fibril's surface amino acid residues demonstrated these techniques capabilities of mapping surface molecules. However, the most significant result arose from the enhanced Amide I bands. The enhanced Raman bands were all much narrower than the far field Raman Amide I band. The SERS and TERS Amide I bands have the potential to replace the current technique of fitting the wide far field band with a spectral deconvolution which would increase the accuracy of protein secondary structure assignment.

7.3 Improvements

The TERS technique had the most room for improvement. Only silver coated tips performed well with our set-up. With the success of the gold nanoparticles in the SERS experiments, gold-coated tips should be examined. These tips could be manufactured by sputtering tips with gold under conditions that would create larger grains closer to 65 nm in size. The tips could also be fabricated with an improved gold nanoparticle attachment process.

Our current set-up is being modified to include a long working distance dark field condenser. This can be used to directly measure the plasmon resonance of future tips and nanoparticle aggregations. In this thesis, we were only able to categorize the manufacture tips as "active" or "inactive". With this new set-up, they can be categorized by how close their plasmon resonance is to our excitation laser, making it much easier to improve the tip fabrication process.

We observed significant wear of the tips during our scans. Scanning in modes that minimize tip wear could improve both the longevity of the active tips and the resolution of the TERS maps. Increased scanning stability would minimize the likelihood of the tip becoming out of contact during the scan or drifting. Since these experiments were completed, a new Bruker BioScope Catalyst AFM was purchased. This AFM uses a new imaging mode called Peak Force Tapping. The mode performs a fast force

curve at every pixel and adjusts the feedback parameters based on these curves. It claims to operate at forces lower than tapping mode. This has the potential to reduce the tip wear problem that occurred with our previous AFM. This mode also has the possibility of producing more stable scans reducing drift.

It would also be beneficial to perform the TERS experiments in water. All the TERS measurements in this thesis were performed in air. The conditions would be closer to ones found in native collagen. Water would also reduce any heating effects. When scanning in water it is important to use lower forces to avoid the coating peeling off. Hopefully this won't be a problem with the new AFM.

7.4 Outlook

The next step in the characterization of collagen I fibrils is to obtain Raman maps along the fibril axis to reveal chemical motifs associated with the 67 nm banding pattern. Our approach, potentially, could be applied to other issues in the field of collagen research such as the structural/mechanical relationship of various types of fibrils, the effect of heat on collagen structure, and the impact of aging.

Both SERS and TERS techniques investigated in this thesis can also be applied to samples harvested from tissues to investigate naturally occurring changes in the structure and chemical composition of collagen fibrils. The SERS techniques were applied to the fascicles removed from a rat tail tendon. In the same way it can be applied to many other biological samples. It can be applied to measure penetration of different nanoparticles in tissues. It is also possible to examine the 3D structure of a tissue through SERS sectioning. In the same way it can be used to study the distribution of nanoparticles with targeting antibodies attached to their surface in a sample.

The tendon fascicles can be investigated in greater detail with the SERS nanoparticles. The mechanical properties of tendon are of particlular interest in the biological and medical community. The presence of the Amide I band in the SERS spectra shows a great deal of promise for potential applications. The SERS Amide I bands can be examined during stretching experiments. The changes and Amide I bands can also be studied as a function of fascicle depth.

Bibliography

[1] Roman Tuma. Raman spectroscopy of proteins: from peptides to large assemblies. *Journal of Raman Spectroscopy*, 36(4):307–319, April 2005.

[2] Joke De Gelder, Kris De Gussem, Peter Vandenabeele, and Luc Moens. Reference database of Raman spectra of biological molecules. *Journal of Raman Spectroscopy*, 38:1133–1147, 2007.

[3] K Sakamoto and G Mizutani. Absolute Raman-scattering cross section of a surface-adsorbed layer: Amorphous nitrobenzene on Ni (111). *Physical Review B*, 48(12), 1993.

[4] S Nie and Sr Emory. Probing Single Molecules and Single Nanoparticles by Surface-Enhanced Raman Scattering. *Science (New York, N.Y.)*, 275(5303):1102–6, February 1997.

[5] Catalin Neacsu, Jens Dreyer, Nicolas Behr, and Markus Raschke. Scanning-probe Raman spectroscopy with single-molecule sensitivity. *Physical Review B*, 73(19):1–4, May 2006.

[6] Saratchandra Shanmukh, Les Jones, Jeremy Driskell, Yiping Zhao, Richard Dluhy, and Ralph a Tripp. Rapid and sensitive detection of respiratory virus molecular signatures using a silver nanorod array SERS substrate. *Nano letters*, 6(11):2630–6, November 2006.

[7] W R Premasiri, D T Moir, M S Klempner, N Krieger, G Jones, and L D Ziegler. Characterization of the surface enhanced raman scattering (SERS) of bacteria. *The journal of physical chemistry. B*, 109(1):312–20, January 2005.

[8] Katrin Kneipp, Harald Kneipp, Ramasamy Manoharan, Irving Itzkan, Ramachandra R Dasari, and Michael S Feld. Surface-enhanced Raman scattering (SERS) a new tool for single molecule detection and identification. *Bioimaging*, 6(2):104–110, June 1998.

[9] S Stewart and P.M Fredericks. Surface-enhanced Raman spectroscopy of amino acids adsorbed on an electrochemically prepared silver surface. *Spectrochimica Acta Part A: Molecular and Biomolecular Spectroscopy*, 55(7-8):1641–1660, July 1999.

[10] Tanja Deckert-Gaudig and Volker Deckert. Tip-enhanced Raman scattering (TERS) and high-resolution bio nano-analysis–a comparison. *Physical chemistry chemical physics : PCCP*, 12(38):12040–9, October 2010.

[11] Taro Ichimura, Shintaro Fujii, Prabhat Verma, Takaaki Yano, Yasushi Inouye, and Satoshi Kawata. Subnanometric Near-Field Raman Investigation in the Vicinity of a Metallic Nanostructure. *Physical Review Letters*, 102(18):1–4, May 2009.

[12] Jon P Camden, Jon a Dieringer, Jing Zhao, and Richard P Van Duyne. Controlled plasmonic nanostructures for surface-enhanced spectroscopy and sensing. *Accounts of chemical research*, 41(12):1653–61, December 2008.

[13] Stephen D Hudson and George Chumanov. Bioanalytical applications of SERS (surface-enhanced Raman spectroscopy). *Analytical and bioanalytical chemistry*, 394(3):679–86, June 2009.

[14] Corinne Gullekson, Leanne Lucas, Kevin Hewitt, and Laurent Kreplak. Surface-sensitive Raman spectroscopy of collagen I fibrils. *Biophysical journal*, 100(7):1837–45, April 2011.

[15] Alois Bonifacio and Valter Sergo. Effects of sample orientation in Raman microspectroscopy of collagen fibers and their impact on the interpretation of the amide III band. *Vibrational Spectroscopy*, 53(2):314–317, July 2010.

[16] K E Kadler, D F Holmes, J A Trotter, and J A Chapman. Collagen fibril formation. *The Biochemical journal*, 316:1–11, May 1996.

[17] Jyrki Heino, Mikko Huhtala, Jarmo Käpylä, and Mark S Johnson. Evolution of collagen-based adhesion systems. *The international journal of biochemistry & cell biology*, 41(2):341–8, February 2009.

[18] A Rich and F H Crick. The structure of collagen. *Nature*, 176(4489):915–6, November 1955.

[19] PM Cowan, S McGavin, and ACT North. Polypeptide Chain Configuration of Collagen. *Nature*, 176(4492):1062–1064, 1955.

[20] J Gross. A study of certain connective tissue constituents with the electron microscope. *Annals of the New York Academy of Sciences*, 52(7):964–70, May 1950.

[21] Matthew D Shoulders and Ronald T Raines. Collagen structure and stability. *Annual review of biochemistry*, 78:929–58, January 2009.

[22] B.L. Trus and K.A. Piez. Compressed microfibril models of native collagen fibril. *Nature*, 286:300–301, 1980.

[23] A. George, J.P. Malone, and A. Veis. The secondary structure of type I collagen N-telopeptide as demonstrated by Fourier transform IR spectroscopy and molecular modeling. *Journal of Chemical Sciences*, 111(1):121–131, 1999.

[24] James P Malone, Anne George, and Arthur Veis. Type I collagen N-telopeptides adopt an ordered structure when docked to their helix receptor during fibrillogenesis. *Proteins*, 54(2):206–15, February 2004.

[25] Alexander Rich and F.H.C. Crick. The molecular structure of collagen. *Journal of Molecular Biology*, 3(5):483–IN4, October 1961.

[26] Kenji Okuyama, Xiaozhen Xu, Makoto Iguchi, and Keiichi Noguchi. Revision of Collagen Molecular Structure. *Biopolymers*, 84:181–191, 2006.

[27] Arnab Bhattacharjee and Manju Bansal. Collagen structure: the Madras triple helix and the current scenario. *IUBMB life*, 57(3):161–72, March 2005.

[28] Bojan Zagrovic, Guha Jayachandran, Ian S Millett, Sebastian Doniach, and Vijay S Pande. How large is an alpha-helix? Studies of the radii of gyration of helical peptides by small-angle X-ray scattering and molecular dynamics. *Journal of molecular biology*, 353(2):232–41, October 2005.

[29] Johanna Myllyharju. Intracellular Post-Translational Modifications of Collagens. *Topics in Current Chemistry*, 247:115– 147, 2005.

[30] L I Fessler, R E Burgeson, N P Morris, and J H Fessler. Collagen synthesis: a disulfide-linked collagen precursor in chick bone. *Proceedings of the National Academy of Sciences of the United States of America*, 70(10):2993–6, October 1973.

[31] H D Moeller, U Bosch, and B Decker. Collagen fibril diameter distribution in patellar tendon autografts after posterior cruciate ligament reconstruction in sheep: changes over time. *Journal of anatomy*, 187:161–7, August 1995.

[32] G King, E M Brown, and J M Chen. Computer model of a bovine type I collagen microfibril. *Protein engineering*, 9(1):43–9, January 1996.

[33] J.W. Smith. Molecular Pattern in Native Collagen. *Nature*, 219:157–158, 1968.

[34] By T J Wess. Collagen fibril form and function. *Advances in Protein Chemistry*, 70:341–374, 2005.

[35] Franz J. Giessibl. Advances in atomic force microscopy. *Reviews of Modern Physics*, 75(3):949–983, July 2003.

[36] D Rugar and P Hansma. Atomic force microscopy. *Physics today*, 43(10):23–30, 1990.

[37] N Jalili. A review of atomic force microscopy imaging systems: application to molecular metrology and biological sciences. *Mechatronics*, 14(8):907–945, October 2004.

[38] Maher S. Amer. *Raman spectroscopy for soft matter applications*. John Wiley & Sons Inc., 2008.

[39] M Fleischmann, PJ Hendra, and AJ McQuillan. Raman spectra of pyridine adsorbed at a silver electrode. *Chemical Physics Letters*, 26(2):163–166, 1974.

[40] Katherine A Willets and Richard P Van Duyne. Localized Surface Plasmon Resonance Spectroscopy and Sensing. *Annual Review of Physical Chemistry*, 58:267–297, 2007.

[41] E.C. Le Ru and P.G. Etchegoin. *Principles of Surface-Enhanced Raman Spectroscopy: and related plasmonic effects*. Elsevier Science, 2008.

[42] T. Dörfer, Michael Schmitt, and J. Popp. Deep-UV surface-enhanced Raman scattering. *Journal of Raman Spectroscopy*, 38(11):1379–1382, 2007.

[43] Jitka Cejkova, Vadym Prokopec, Sona Brazdova, Alzbeta Kokaislova, Pavel Matejka, and Frantisek Stepanek. Characterization of copper SERS-active substrates prepared by electrochemical deposition. *Applied Surface Science*, 255(18):7864–7870, June 2009.

[44] J. J. Mock, S. M. Norton, S.-Y. Chen, a. a. Lazarides, and D. R. Smith. Electromagnetic Enhancement Effect Caused by Aggregation on SERS-Active Gold Nanoparticles. *Plasmonics*, October 2010.

[45] Tobias Geldhauser, Shintarou Ikegaya, Andreas Kolloch, Naoki Murazawa, Kosei Ueno, Johannes Boneberg, Paul Leiderer, Elke Scheer, and Hiroaki Misawa. Visualization of Near-Field Enhancements of Gold Triangles by Nonlinear Photopolymerization. *Plasmonics*, January 2011.

[46] Pedro H C Camargo, Claire M Cobley, Matthew Rycenga, and Younan Xia. Measuring the surface-enhanced Raman scattering enhancement factors of hot spots formed between an individual Ag nanowire and a single Ag nanocube. *Nanotechnology*, 20(43):434020, October 2009.

[47] Miodrag Micic, Nicholas Klymyshyn, Yung Doug Suh, and H. Peter Lu. Finite Element Method Simulation of the Field Distribution for AFM Tip-Enhanced Surface-Enhanced Raman Scanning Microscopy. *The Journal of Physical Chemistry B*, 107(7):1574–1584, February 2003.

[48] PC Lee and D. Meisel. Adsorption and surface-enhanced Raman of dyes on silver and gold sols. *The Journal of Physical Chemistry*, 86(17):3391–3395, August 1982.

[49] N. Felidj, J. Aubard, G. Levi, J. R. Krenn, a. Hohenau, G. Schider, a. Leitner, and F. R. Aussenegg. Optimized surface-enhanced Raman scattering on gold nanoparticle arrays. *Applied Physics Letters*, 82(18):3095, 2003.

[50] K.-H. Su, Q.-H. Wei, X. Zhang, J. J. Mock, D. R. Smith, and S. Schultz. Interparticle Coupling Effects on Plasmon Resonances of Nanogold Particles. *Nano Letters*, 3(8):1087–1090, August 2003.

[51] Linda Gunnarsson, Tomas Rindzevicius, Juris Prikulis, Bengt Kasemo, Mikael Käll, Shengli Zou, and George C Schatz. Confined plasmons in nanofabricated single silver particle pairs: experimental observations of strong interparticle interactions. *The journal of physical chemistry. B*, 109(3):1079–87, January 2005.

[52] R. Aroca. *Surface-Enhanced Vibrational Spectroscopy*. Wiley Online Library, 2006.

[53] J.R. Ferraro and K. Nakamoto. *Introductory raman spectroscopy*. Academic Pr, 2003.

[54] W Fischer. Raman and FTIR spectroscopic study on water structural changes in aqueous solutions of amino acids and related compounds. *Journal of Molecular Structure*, 415(3):249–257, October 1997.

[55] Hans H. Eysel and Kye Taek Lim. Raman intensities of phosphate and diphosphate ions in aqueous solution. *Journal of Raman Spectroscopy*, 19(8):535–539, December 1988.

[56] W. Zhang, T. Schmid, B.-S. Yeo, and R. Zenobi. Near-Field Heating, Annealing, and Signal Loss in Tip-Enhanced Raman Spectroscopy. *Journal of Physical Chemistry C*, 112(6):2104–2108, February 2008.

[57] Tanja Deckert-gaudig, Eva Rauls, and Volker Deckert. Aromatic Amino Acid Monolayers Sandwiched between Gold and Silver : A Combined Tip-Enhanced Raman and Theoretical Approach. *Journal of Physical Chemistry C*, 114:7412–7420, 2010.

[58] Achim Hartschuh. Tip-enhanced near-field optical microscopy. *Angewandte Chemie (International ed. in English)*, 47(43):8178–91, January 2008.

[59] Sarah M Stranahan and Katherine a Willets. Super-resolution Optical Imaging of Single-Molecule SERS Hot Spots. *Nano letters*, pages 3777–3784, August 2010.

[60] K.F. Domke, D. Zhang, and B. Pettinger. Enhanced Raman Spectroscopy: Single Molecules or Carbon? *Journal of Physical Chemistry C*, 111(24):8611–8616, June 2007.

[61] Yasutaka Kitahama, Akari Ogawa, Yuhei Tanaka, Safwan Obeidat, Tamitake Itoh, Mitsuru Ishikawa, and Yukihiro Ozaki. Difference in time dependence of surface-enhanced Raman scattering spectra of thiacarbocyanine J- and H-aggregates adsorbed on single silver nanoaggregates. *Chemical Physics Letters*, 493(4-6):309–313, June 2010.

[62] Andrzej Kudelski. Role of O2 in inducing intensive fluctuations of surface-enhanced Raman scattering spectra. *The journal of physical chemistry. B*, 110(25):12610–5, June 2006.

[63] Yung Doug Suh, Gregory K Schenter, Leyun Zhu, and H Peter Lu. Probing nanoscale surface enhanced Raman-scattering fluctuation dynamics using correlated AFM and confocal ultramicroscopy. *Ultramicroscopy*, 97(1-4):89–102, 2003.

[64] Boon-Siang Yeo, Johannes Stadler, Thomas Schmid, Renato Zenobi, and Weihua Zhang. Tip-enhanced Raman Spectroscopy Its status, challenges and future directions. *Chemical Physics Letters*, 472(1-3):1–13, April 2009.

[65] D. Richards, R. G. Milner, F. Huang, and F. Festy. Tip-enhanced Raman microscopy: practicalities and limitations. *Journal of Raman Spectroscopy*, 34(9):663–667, September 2003.

[66] B G Frushour and J L Koenig. Raman scattering of collagen, gelatin, and elastin. *Biopolymers*, 14(2):379–91, February 1975.

[67] Maria Jastrzebska, Roman Wrzalik, Antoni Kocot, Justyna Zalewska-Rejdak, and Beata Cwalina. Raman spectroscopic study of glutaraldehyde-stabilized collagen and pericardium tissue. *Journal of biomaterials science. Polymer edition*, 14(2):185–97, January 2003.

[68] Daimay Lin-Vien, NB Colthup, and WG Fateley. *The Handbook of Infrared and Raman Characteristic Frequencies of Organic Molecules*. 1991.

[69] M. Reches and E. Gazit. Casting Metal Nanowires within Discrete Self-Assembled Peptide Nanotubes. *Science*, 300(5619):625, 2003.

[70] F.R. Dollish, W.G. Fateley, and F.F. Bentley. *Characteristic Raman Frequencies of Organic Compounds*. Wiley New York;, 1974.

[71] Marc Chaigneau, Gennaro Picardi, and Razvigor Ossikovski. Molecular Arrangement in Self-Assembled Azobenzene-Containing Thiol Monolayers at the Individual Domain Level Studied through Polarized Near-Field Raman Spectroscopy. *International journal of molecular sciences*, 12(2):1245–58, January 2011.

[72] Catalin C. Neacsu, Samuel Berweger, and Markus B. Raschke. Tip-Enhanced Raman Imaging and Nanospectroscopy: Sensitivity, Symmetry, and Selection Rules. *NanoBiotechnology*, 3(3-4):172–196, February 2009.

[73] S. Stewart and P.M. Fredericks. Surface-enhanced Raman spectroscopy of peptides and proteins adsorbed on an electrochemically prepared silver surface. *Spectrochimica Acta Part A: Molecular and Biomolecular Spectroscopy*, 55(7-8):1615–1640, July 1999.

[74] G. Varsanyi. *Assignment for vibrational spectra of seven hundred benzene derivatives*. 1974.

[75] Robert Jeffers and John Cooper. FT-Surface-Enhanced Raman Scattering of Phenylalanine Using Silver-Coated Glass Fiber Filters. *Spectroscopy Letters*, 43(3):220–225, April 2010.

[76] Tonya M. Herne, Angela Ahern, and Robin L. Garrell. Surface-enhanced Raman spectroscopy of peptides: preferential N-terminal adsorption on colloidal silver. *Journal of the American Chemical Society*, 113(3):846–854, January 1991.

[77] Sang-Woo Joo and Kwan Kim. Adsorption of phenylacetylene on gold nanoparticle surfaces investigated by surface-enhanced Raman scattering. *Journal of Raman Spectroscopy*, 35(7):549–554, July 2004.

[78] J. R. Anema, A. G. Brolo, A. Felten, and C. Bittencourt. Surface-enhanced Raman scattering from polystyrene on gold clusters. *Journal of Raman Spectroscopy*, 41:745–751, 2010.

[79] J.R. Lombardi and R.L. Birke. A Unified Approach to Surface-Enhanced Raman Spectroscopy. *Journal of Physical Chemistry C*, 112(14):5605–5617, April 2008.

[80] Antonello Merlino, Filomena Sica, Lelio Mazzarella, Adriana Zagari, and Alessandro Vergara. Correlation between Raman and X-ray crystallography data of (Pro-Pro-Gly)10. *Biophysical chemistry*, 137(1):24–7, September 2008.

[81] P.Y. Chou and G.D. Fasman. Prediction of protein conformation. *Biochemistry*, 13(2):222–245, 1974.

[82] Robert a. Copeland and Thomas G. Spiro. Ultraviolet Raman hypochromism of the tropomyosin amide modes: a new method for estimating .alpha.-helical content in proteins. *Journal of the American Chemical Society*, 108(6):1281–1285, March 1986.

[83] Iain H McColl, Ewan W Blanch, Andrew C Gill, Alexandre G O Rhie, Mark a Ritchie, Lutz Hecht, Kurt Nielsen, and Laurence D Barron. A new perspective on beta-sheet structures using vibrational Raman optical activity: from poly(L-lysine) to the prion protein. *Journal of the American Chemical Society*, 125(33):10019–26, August 2003.

[84] Elena Bailo and Volker Deckert. Tip-enhanced Raman scattering. *Chemical Society reviews*, 37(5):921–30, May 2008.

[85] Yang Gan. Invited review article: a review of techniques for attaching micro- and nanoparticles to a probe's tip for surface force and near-field optical measurements. *The Review of scientific instruments*, 78(8):081101, August 2007.

[86] Takashi Kodama and Hiroyuki Ohtani. Surface enhanced Raman scattering imaging of carbon onions with a silver nanoparticle immobilized tip. *Applied Physics Letters*, 89(22):223107, 2006.

[87] T Kodama, T Umezawa, S Watanabe, and H Ohtani. Development of aperture less near-field scanning optical microscope tips for tip-enhanced Raman spectroscopy. *Journal of microscopy*, 229(2):240–6, February 2008.

[88] Ivan U Vakarelski and Ko Higashitani. Single-nanoparticle-terminated tips for scanning probe microscopy. *Langmuir : the ACS journal of surfaces and colloids*, 22(7):2931–4, March 2006.

[89] Janos H. Fendler. Self-Assembled Nanostructured Materials. *Chemistry of Materials*, 8(8):1616–1624, January 1996.

[90] Thomas Schmid, B.S. Yeo, Grace Leong, Johannes Stadler, and Renato Zenobi. Performing tip-enhanced Raman spectroscopy in liquids. *Journal of Raman Spectroscopy*, 40(10):1392–1399, 2009.

[91] Mark S. Anderson and William T. Pike. A Raman-atomic force microscope for apertureless-near-field spectroscopy and optical trapping. *Review of Scientific Instruments*, 73(3):1198, 2002.

[92] Y K Kim, J B Ketterson, and D J Morgan. Scanning plasmon optical microscope operation in atomic force microscope mode. *Optics letters*, 21(3):165–7, February 1996.

[93] Alexander Weber-Bargioni, Adam Schwartzberg, Matteo Cornaglia, Ariel Ismach, Jeffrey J Urban, Yuanjie Pang, Reuven Gordon, Jeffrey Bokor, Miquel B Salmeron, D Frank Ogletree, Paul Ashby, Stefano Cabrini, and P James Schuck. Hyperspectral Nanoscale Imaging on Dielectric Substrates with Coaxial Optical Antenna Scan Probes. *Nano letters*, January 2011.

[94] John T Bahns, Qiti Guo, Jason M Montgomery, Stephen K Gray, Heinrich M Jaeger, and Liaohai Chen. High Fidelity Nano-Hole Enhanced Raman Spectroscopy. *The journal of physical chemistry. C, Nanomaterials and interfaces*, 113(26):11190–11197, July 2009.

[95] Qiuming Yu, Phillip Guan, Dong Qin, Greg Golden, and Paul M Wallace. Inverted size-dependence of surface-enhanced Raman scattering on gold nanohole and nanodisk arrays. *Nano letters*, 8(7):1923–8, July 2008.

[96] T. Rindzevicius, Y. Alaverdyan, B. Sepulveda, T. Pakizeh, M. Kall, R. Hillenbrand, J. Aizpurua, and F.J. GarciadeAbajo. Nanohole Plasmons in Optically Thin Gold Films. *Journal of Physical Chemistry C*, 111(3):1207–1212, January 2007.

[97] DJ Semin, A Lo, SE Roark, and RT Skodje. Time-dependent morphology changes in thin silver films on mica: A scaling analysis of atomic force microscopy results. *Journal of Chemical*, 105(13):5542–5551, 1996.

[98] Alistair P D Elfick, Andrew R Downes, and Rabah Mouras. Development of tip-enhanced optical spectroscopy for biological applications: a review. *Analytical and bioanalytical chemistry*, 396(1):45–52, January 2010.

[99] Y Charles Cao, Rongchao Jin, Jwa-Min Nam, C Shad Thaxton, and Chad a Mirkin. Raman dye-labeled nanoparticle probes for proteins. *Journal of the American Chemical Society*, 125(48):14676–7, December 2003.

[100] Nahla a Abu Hatab, Jenny M Oran, and Michael J Sepaniak. Surface-enhanced Raman spectroscopy substrates created via electron beam lithography and nanotransfer printing. *ACS nano*, 2(2):377–85, February 2008.

[101] R. W. D. Rowe. The Structure of Rat Tail Tendon Fascicles. *Connective Tissue Research*, 14(1):21–30, January 1985.

[102] H R C Screen, D a Lee, D L Bader, and J C Shelton. An investigation into the effects of the hierarchical structure of tendon fascicles on micromechanical properties. *Proceedings of the Institution of Mechanical Engineers, Part H: Journal of Engineering in Medicine*, 218(2):109–119, January 2004.

[103] M. Raspanti, T. Congiu, and S. Guizzardi. Structural Aspects of the Extracellular Matrix of the Tendon: An Force and Scanning Electron Microscopy Study. *Archives of histology and cytology*, 65(1):37–43, 2002.

[104] P Kannus. Structure of the tendon connective tissue. *Scandinavian journal of medicine & science in sports*, 10(6):312–20, December 2000.

[105] H R C Screen, D L Bader, J C Shelton, and D A Lee. Non-collangenous matrix components influence the micro-mechanical environment of tenocytes within tedon fascicles subjected to tensile strain. *European Cells and Materials*, 4:41–42, 2002.

[106] Ximei Qian, Xiang-Hong Peng, Dominic O Ansari, Qiqin Yin-Goen, Georgia Z Chen, Dong M Shin, Lily Yang, Andrew N Young, May D Wang, and Shuming Nie. In vivo tumor targeting and spectroscopic detection with surface-enhanced Raman nanoparticle tags. *Nature biotechnology*, 26(1):83–90, January 2008.

[107] S Keren, C Zavaleta, Z Cheng, a de la Zerda, O Gheysens, and S S Gambhir. Noninvasive molecular imaging of small living subjects using Raman spectroscopy. *Proceedings of the National Academy of Sciences of the United States of America*, 105(15):5844–9, April 2008.

[108] Y N Wang, C Galiotis, and D L Bader. Determination of molecular changes in soft tissues under strain using laser Raman microscopy. *Journal of biomechanics*, 33(4):483–6, April 2000.

Appendix A

Vibrational Modes of Benzene Derivatives

Wilson number	Phe(cm^{-1})	species	polarizability components	Tyr(cm^{-1})	species
9b	320±30	B_2	yz		
16a	405±15	A_2	xy	400±20	A_u (not active)
16b	448±13	B_1	xz		
	478±18	A_1	xx, yy, zz		
6b	618±12	B_2	yz	630±20	B_{3g}
4	690±10	B_1	xz	700±35	B_{2g}
11	716±14	B_1	xz		
	755±25	A_1	xx, yy, zz		
			xx, yy, zz	820±50	A_g
10a	835±25	A_2	xy	820±30	B_{1g}
17b	910±30	B_1	xz		
17a	960±20	A_2	xy	960±30	A_u (not active)
	985±15	B_1	xz		
12	1000±10	A_1	xx, yy, zz		
18a	1023±6	A_1	xx, yy, zz	1012±9	B_{1u} (not active)
18b	1074±8	B_2	yz	1107±22	B_{2u} (not active)
15	1156±5	B_2	yz		
9a	1175±5	A_1	xx, yy, zz	1166±24	A_g
	1205	A_1	xx, yy, zz		
			xx, yy, zz	1210±10	A_g
				1250±15	B_{1u} (not active)
3	1285±10	B_2	yz	1286±26	B_{3g}
14	1325±12	B_2	yz	1310±70	B_{2u} (not active)
19b	1455±15	B_2	yz	1420±50	B_{2u} (not active)
19a	1492±22	A_1	xx, yy, zz	1495±35	B_{1u} (not active)
8b	1579±18	B_2	yz	1578±26	B_{3g}
8a	1594±20	A_1	xx, yy, zz	1600±29	A_g

Table A.1: Mono- and para-substituted benzene vibrations below 3000 cm^{-1} [70].